Alma Mater Studiorum · University of Bologna

School of Science
Department of Physics and Astronomy
Master Degree in Physics

Construction and detectors' characterization of a new detection system for FAMU Experiment

Supervisor:
Prof. Giuseppe Baldazzi

Submitted by:
Simone Fumagalli

Academic Year 2021/2022

Abstract

From 2010, the Proton Radius has become one of the most interest value to determine. The first proof of not complete understanding of its internal structure was the measurement of the Lamb Shift using the muonic hydrogen, leading to a value 7σ lower. A new road so was open and the Proton Radius Puzzle epoch begun.

FAMU Experiment is a project that tries to give an answer to this Puzzle implementing high precision experimental apparatus.

The work of this thesis is based on the study, construction and first characterization of a new detection system. Thanks to the previous experiments and simulations, this apparatus is composed by 17 detectors positioned on semicircular crown with the related electronic circuit.

The detectors' characterization is based on the use of a LabView program controlling a digital potentiometer and on other two analog potentiometers, all three used to set the amplitude of each detector to a predefined value, around $1.2V$, set on the oscilloscope by which is possible to observe the signal. This is the requirement in order to have, in the final measurement, a single high peak given by the sum of all the signals coming from the detectors. Each signal has been acquired for almost half of an hour, but the entire circuit has been maintained active for more time to observe its capacity to work for longer periods.

The principal results of this thesis are given by the spectra of 12 detectors and the corresponding values of Voltages, FWHM and Resolution.

The outcomes of the acquisitions show also another expected behavior: the strong dependence of the detectors from the temperature, demonstrating that an its change causes fluctuations in the signal. In turn, these fluctuations will affect the spectrum, resulting in a shifting of the curve and a lower Resolution. On the other hand, a measurement performed in stable conditions will lead to accordance between the nominal and experimental measurements, as for the detectors 10, 11 and 12 of our system.

Sommario

Dal 2010, il raggio del protone è diventato uno dei valori più interessanti da determinare. La prima prova della non completa comprensione della sua struttura interna è stata la misurazione del Lamb Shift utilizzando l'idrogeno muonico, che ha portato a un valore inferiore di 7σ. Si aprì così una nuova strada e iniziò l'epoca del Puzzle del Raggio Protonico.

L'esperimento FAMU è un progetto che cerca di dare una risposta a questo Puzzle impiegando un apparato strumentale ad alta precisione.

Il lavoro di questa tesi si basa sullo studio, costruzione e prima caratterizzazione di un nuovo sistema di rilevazione. Grazie agli esperimenti e alle simulazioni precedenti, questo apparato è composto da 17 detector posizionati su una corona semicircolare con il relativo circuito elettronico.

La caratterizzazione dei detector si basa sull'uso di un programma LabView che controlla un potenziometro digitale e altri due potenziometri analogici, tutti e tre impiegati per impostare l'ampiezza di ciascun detector a un valore predefinito intorno a $1.2\,V$, settato sull'oscilloscopio da cui poter osservare il segnale. Questo è il requisito per avere, nella misura finale, un unico picco alto dato dalla somma di tutti i segnali provenienti dai detector. Ogni segnale è stato acquisito per quasi mezz'ora, ma l'intero circuito è stato mantenuto attivo per più tempo per osservare la sua capacità di funzionare anche più a lungo.

I principali risultati di questa tesi sono dati dagli spettri di 12 detector e dai corrispondenti valori di tensione, FWHM e risoluzione.

I risultati delle acquisizioni mostrano anche un altro comportamento atteso: la forte dipendenza dei detector dalla temperatura, dimostrando che una sua variazione provoca fluttuazioni nel segnale. A loro volta, queste fluttuazioni influenzano lo spettro, determinando uno spostamento della curva e una risoluzione più bassa. D'altra parte, una misura eseguita in condizioni stabili porterà alla concordanza tra le misure nominali e quelle sperimentali, come nel caso dei detector 10, 11 e 12 del nostro sistema.

Contents

Introduction

Before 2010 the subnuclear physics was supposed to known in all its forms.

After this year, the scientific community has been shaken from the news that a laser spectroscopy used to measure the Lamb Shift through the implementation of the muonic hydrogen has led to a proton radius lower of several standard deviations with respect to the accepted value.

The new discovery gave birth to the so called Proton Radius Puzzle in which every scientific group tried to find the most accurate measure of the proton radius.

The FAMU Experiment so is an Italian project that tries to defined with accuracy the proton radius, taking measurements at RIKEN RAL facility in London.

This thesis work focuses on the detection system of the FAMU Experiment and on the characterization of each installed detector.

The topic of the first chapter regards the proton. At first some information about its discovery are given while in the following paragraphs the internal structure is studied by considering different kind of methods: the Electron Proton Scattering and the Atomic Hydrogen Spectroscopy. In addition to the explanation of the methodology, the results of four main experiments are presented, focusing on the differences and similarities.

The second chapter talks about the other main character of the story: the Muon. Its general characteristics are given at first, focusing then on how it is formed and the kind of interaction with the matter. In the end, the result of the first successful laser spectroscopy, known as CREMA, is presented, together with an its update performed in 2013.

The third chapter focuses on the FAMU Experiment. It is presented through the last experimental apparatus implemented: Beam and Laser, the Cryogenic System and the Detection System with its electronic parts. Then the chapter continues with the experimental results obtained in several years, starting from 2014 up to 2021. In this way, the evolution of the experimental apparatus and results are shown.

The subject of the fourth chapter is the circuitry of the Detection System. For each detector there is one module controlling it. Each module can be seen as composed by two main parts: the Acquisition of the Signal and the Feedback on High Voltage. The Acquisition of the Signal starts with the scintillation of $LaBr_3$ which reaches the PMT. The outcoming signal then is processed passing through a series of components like the Front End, the BaseLine Restorer and the Buffer. The HV Feedback instead works on the High Voltage, controlling its value thanks to the implementation of several potentiometer.

In the last chapter, the working process is explained. Everything starts with the LabView program which turns on the system. The HV voltage is controlled by three potentiometer: one acts directly on the HV, one controlling the proportionality factor between the HV and output voltage and the digital potentiometer to change

the value of the HV once the analog potentiometers cannot be reached. In the end, the results of the detectors' characterization are presented and discussed, showing the detectors characteristics extrapolated using the Oscilloscope. In addition, the spectrum obtained using a MatLab program are shown.

Chapter 1

Proton

One of the questions to which the FAMU experiment want to answer is the well-known "Proton Radius Puzzle".

This Puzzle is born in last decades from the recognition that the proton radius doesn't have the same value using different methods to evaluate it.

Indeed, before 2010, the scientific community supposed to know exactly the dimensions of the proton. In 2010 the first successully Lamb Shift measurement of muonic hydrogen evaluates a lower value with respect to that expected, approximately 5 standard deviations (5σ) lower, demonstrating that the human knowledge about the proton was far from being fully acquired. Since 2010 therefore the race to discover the proton radius with the highest possible precision has begun.

This chapter will shown a brief history of the proton and the physics related to the measurement of the proton radius obtained following two different methods: the Electron-Proton Scattering and the Atomic Hydrogen Spectroscopy.

Then, the results of four different experiments will be presented, showing differences and similarities between what have been found.

1.1 The positive constituent of the atom

The physics of the elementary particles has been started with the work of the physicist J.J. Thomson.

From J.J. Thomson's studies in 1897 (Thomson, 1897), the deflection of cathode rays brought to the discovery that they carries negative electric charge. By studying this effect, Thomson estimated the velocity of these particles that, in the end, he called corpuscles. In 1891, George Johnstone Stoney had introduced the term electron for the fundamental unit of charge and only later this became the name that identified the particle.

These particles remained the only constituents of the atom for almost ten years but everything changed with furthers discoveries over the alpha particle.

Indeed, in the early years of the twenty century, Rutherford bombed a gold thin plate with alpha particles. As expected, most of these particles passed through the matter undeflected. The unxpected event was the deflection at large angles of some of these alpha particles (Gegier and Marsden, 1909) and in some cases they were completely rejected back. From these surprisingly results, Rutherford concluded that the deflection of alpha particles was due to the presence of a small positive-charged region, called nucleus, surrounded by electrons.

Around 1920s, it was found that there was no nuclear component of positive charge lighter than the hydrogen nucleus and Rutherford established that the fundamental constituent of the atomic nuclei was the hydrogen nucleus, called from that moment as Proton.

Together with the neutron, discovered in 1932 (Chadwick, 1932), and the electron, the proton is considered nowadays as one of the components that defines the atom. The latter quark theory has led to the concept of hadron, a subatomic particle composed by quarks and anti-quarks. The protons are stable forms of the adrons and they are known as baryons since they are composed by three quarks, two up and one down. Some of the proton's characteristics are the following (Tiesinga et al., 2021):

- its free form is stable in the Standard Model;
- positive unitary charge +1;
- mass of $938.27208816(29)\frac{MeV}{c^2}$;
- spin $\frac{1}{2}$.

1.2 Electron Proton Scattering

To know the role of the proton and the problems connected to the measure of its radius, there is the needing of a deeper understanding of the proton structure. The physical event that can help the knowledge about the internal structure of an object is the scattering process.

The first scattering that will be considered is the Electron–Proton Scattering, especially the elastic case. In elastic scattering, the energy and the momentum of the electron are transferred to the nucleon under the form of a single photon, without exciting any nuclear state.

This description starts with the measurement of the differential cross section for a charged particle scattered off a heavier nucleus, also known as Rutherford's equation (Rutherford, 1911):

$$\left(\frac{d\sigma}{d\Omega}\right)_R = \left(\frac{Z\alpha}{2E}\right)^2 \frac{1}{\sin^4(\frac{\theta}{2})} \tag{1.1}$$

where $\alpha = \frac{e^2}{4\pi} \approx \frac{1}{137}$ is the fine structure constant, Z atomic number of nucleus, E is the electron energy and θ is the electron scattering angle.
For Rutherford scattering, the target recoil is neglected and the scattered particle is non-relativistic. In order to study the proton structure, it's required to consider relativistic scattered particle and so the Rutherford equation needs to be changed. The relativistic expression for the scattering of the charged particle is called Mott's scattering and it takes the form (Guffanti, 2015):

$$\left(\frac{d\sigma}{d\Omega}\right)_M = \left(\frac{d\sigma}{d\Omega}\right)_R (1 - \beta^2 \sin^2 \frac{\theta}{2}) \tag{1.2}$$

being $\beta = \frac{v}{c}$ the incident particle velocity in units of the speed of light.

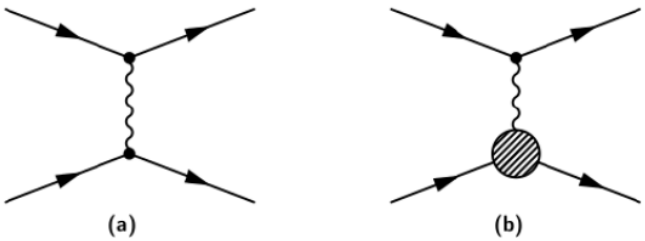

Figure 1.1: Feynman graph of the electron-proton interaction. In the left image (a) the proton is point-like, in the right (b) it has finite dimension. (Guffanti, 2015)

Until this point no information about the internal structure of the proton is contemplated and to show a difference between a point-like target and a finite size object (Figure 1.1) the QED treatment must be used.

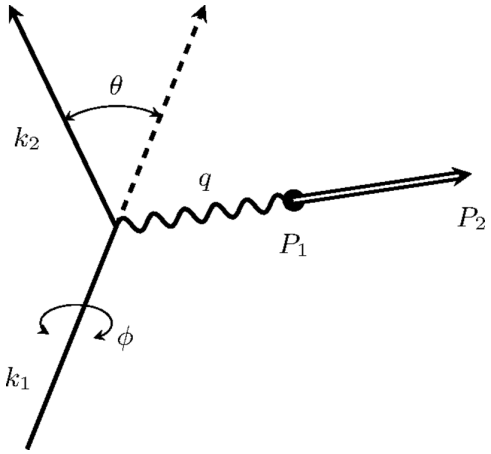

Figure 1.2: The kinematic parameters for the elastic scattering of an electron on a target initially at rest (Bernauer, 2010).

Under the QED description, there are several considerations to do, starting from Figure 1.2. The initial target mass M is at the rest, $\vec{P_1} = (M, 0)$. The incident and scattering electron doesn't share the same four-momentum. Indeed, the incident one has a four-momentum $k_1 = (E_1 = E, \vec{p_1})$ and then it is scattered in the direction $\Omega = (\theta, \phi)$ with a four-momentum $k_2 = (E_2 = E', \vec{p_2})$ as shown in Figure 1.2 (Bernauer, 2010). The unpolarized cross section is independent from the azimuthal angle and so the only degree of freedom considered is just the parameter θ representing the deflection of k_2 with respect to the original direction of k_1 and the energy of the incoming electron E (Bernauer, 2010).

In exchange of a virtual photon, the four-momentum $q = k_1 - k_2$ is transferred to the target. The virtual photon also has a negative four-momentum squared and so $Q^2 = -q^2$.

The matrix element of interaction, representing the spin-averaged invariant amplitude, is (Bernauer, 2010):

$$M_{fi} = J_{\mu}^{elec} \frac{1}{q^2} J_{prot}^{\mu} \tag{1.3}$$

where J_{μ}^{elec} and J_{prot}^{μ} are the electron proton currents (Bernauer, 2010):

$$\begin{aligned} J_{\mu}^{elec} &= -e\bar{u}(k_2)\gamma^u u(k_1), \\ J_{prot}^{\mu} &= e\bar{u}(P_2)\Gamma^u u(P_1). \end{aligned} \tag{1.4}$$

and $u(k)$, $u(p)$ are the associated spinors of the electron and proton.

Right now, the vertex has to be parametrized by introducing the right form factors Γ_i. The most general form is given by (Bernauer, 2010):

$$\Gamma^{\mu} = P_1^{\mu}\Gamma_1 + P_2^{\mu}\Gamma_2 + \gamma^{\mu}\Gamma_3 \tag{1.5}$$

where P_1^{μ}, P_2^{μ} and γ^{μ} are the three independent Lorentz vectors. The form factors Γ_i depend only on Q^2 when thinking about the free on-shell particle. Because $u(P_1)$ and $\bar{u}(P_2)$ satisfy the free Dirac equation, one obtains Γ_1=Γ_2 from the current conservation (Bernauer, 2010):

$$q_{\mu}\bar{u}(P_2)\Gamma^{\mu}u(P_1) = 0. \tag{1.6}$$

Now taking the mass of the proton m_p, the anomalous part of the magnetic moment $k = \mu_p$–1 and employing the Gordon decomposition, Γ_i becomes (Bernauer, 2010):

$$\Gamma^\mu = F_1(q^2)\gamma^\mu + \frac{k}{2m_p}F_2(2^2)i\Big(\frac{\gamma^\mu\gamma^\nu}{2}\Big)iq_\nu = F_1(q^2)\gamma^\mu + \frac{k}{2m_p}F_2(q^2)i\sigma^{\mu\nu}q_\nu, \quad (1.7)$$

where $F_1(q^2)$ is the form factor related to the Dirac charge and intrinsic magnetic moment of the proton, $F_2(q^2)$ the form factor associated with the moment of Pauli.

Using the internal structure of the proton obtained with the one-photon approximation, the unpolarized cross section for the elastic scattering is given by calculating the modulus squared of the matrix element, by summing over the final spins and averaging on the initial ones. This one is called Rosenbluth cross section and it takes the form (Guffanti, 2015):

$$\Big(\frac{d\sigma}{d\Omega}\Big)_{Ros} = \Big(\frac{d\sigma}{d\Omega}\Big)_M [F_1(q^2) - \frac{k^2q^2}{4m_p^2}F_2(q^2) - \frac{q^2}{2m_p}F_1(q^2)kF_2(q^2)\tan\Big(\frac{\theta}{2}\Big)]. \quad (1.8)$$

The Rosenbluth cross section can also take a different form by using the Sachs form factors. The first, known also as electric form factor G_E, describes the proton electric charge distribution (Antognini, 2005):

$$G_E = F_1 + (k\frac{q^2}{4m_p^2})F_2 \quad (1.9)$$

while the latter, known as magnetic form factor G_M, represents the magnetic dipole moment distribution (Antognini, 2005):

$$G_M = F_1 + kF_2. \quad (1.10)$$

Using these last equations 1.9 and 1.10 together with $Q^2 = -q^2$ and $\tau = \frac{Q^2}{4m_p^2}$, the Rosenbluth formula 1.8 becomes (Bernauer, 2010):

$$\Big(\frac{d\sigma}{d\Omega}\Big)_{Ros} = \Big(\frac{d\sigma}{d\Omega}\Big)_M \Big[\frac{G_E^2(Q^2) + \tau G_M^2(Q^2)}{1+\tau} + 2\tau G_M^2(Q^2)\tan^2\Big(\frac{\theta}{2}\Big)\Big]. \quad (1.11)$$

where, considering the static limit, $G_E(0) = 1$ and $G_M(0) = \mu_p$ (Bernauer, 2010). μ_p is known as the magnetic moment of the proton.

After all, it's possible now to determine the radius of the proton, using the form factors introduced before. The following description is similar for G_E and G_M so just one case has been demonstrated, that of G_E. The behaviour of G_E can be expressed as a function of Q^2 (Guffanti, 2015):

$$G_E(Q^2) \approx \frac{G_M(Q^2)}{2.79} \approx \frac{1}{(1 + \frac{Q^2}{0.71GeV^2})^2}. \quad (1.12)$$

Applying the Fourier Transform, G_E is expressed as a function of the charge density while G_M is expressed as a function of magnetic density. Thanks to the Fourier Transform, G_E becomes (Rignanese, 2019):

$$G_E(q^2) = \int \rho(r)e^{iqr}d^3r \quad (1.13)$$

and expanding it in terms of Q^2, one obtains (Antognini, 2005):

$$\frac{G(Q^2)}{G(0)} = 1 + \frac{1}{6}\langle r^2\rangle Q^2 - \frac{1}{120}\langle r^4\rangle Q^4 - \dots \tag{1.14}$$

where $G(Q^2)$ can be substituted by $G_E(Q^2)$ or $G_M(Q^2)$, $G(0)$ respectively by $G_E(0)$ $G_M(0)$ and $\langle r^2\rangle$ is the n-th moment of the electric or magnetic distribution. In the end so the mean squared value of the proton charge radius is given by (Rignanese, 2019):

$$\langle r_E^2\rangle = -\frac{6}{G_E(0)}\frac{dG_E(Q^2)}{dQ^2}\Big|_{Q^2=0} \tag{1.15}$$

and the mean squared value of the proton magnetic radius corresponds to (Rignanese, 2019):

$$\langle r_M^2\rangle = -\frac{6}{G_M(0)}\frac{dG_M(Q^2)}{dQ^2}\Big|_{Q^2=0}. \tag{1.16}$$

1.2.1 Recent Results

In this paragraph, it will be shown the results from a pair of experiments performed on the electron proton scattering to study the proton radius. The first is the experiment performed by the A1 Collaboration, at the Mainz Microtron MAMI in 2010. The second experiment considered will be that of X. Zhan et al. performed in 2011 at the Jefferson Lab in Hall A.

MAMI Facility Experiment

The A1 Collaboration measured about 1400 cross sections in a range of negative four-momentum transfer squared from $Q^2 = 0.004(GeV/c)^2$ up to $Q^2 = 1(GeV/c)^2$ with statistical errors below 0.2% (Bernauer and Collaboration, 2011). The group used a Mainz accelerator MAMI consisting of a cascade of three race track microtrons (RTMs) and a fourth stage composed by a harmonic double sided microtron (HDSM). It is equipped with two electron sources, one thermionic and one polarized (Bernauer, 2010). The detector setup used is called 3-spectrometer-facility, containing three high resolution magnetic spectrometers (Bernauer, 2010), as shown in Fig. 1.3. The 1400 cross sections were measured at different energies of the electron beam, in the range between $180\,MeV$ and $855\,MeV$. The simulation started from equation 1.12, modified introducing the Coulomb corrections. Then G_E and G_M of the proton were extracted by fitting the form factor models directly to the cross sections (Bernauer and Collaboration, 2011).

In this way the charge and magnetic radii are given by (Bernauer and Collaboration, 2011):

$$\langle r_{E/M}^2\rangle = -\frac{6\hbar^2}{G_{E/M}(0)}\frac{dG_{E/M}(Q^2)}{dQ^2}\Big|_{Q^2=0} \tag{1.17}$$

The models so considered can be grouped as follows: "one is the group of models based on splines with varying degree of basis functions and number of support points while, in the other group, the models are composed of polynomials with varying orders" (Bernauer and Collaboration, 2011).

Figure 1.3: The A1 hall. The three big spectrometers A (red, left), B (blue, middle), C (green, right) are visible (Bernauer, 2010).

For the spline groups, the value of the charge and magnetic radii are (Bernauer and Collaboration, 2011):

$$\langle r_E^2 \rangle^{\frac{1}{2}} = 0.875(5)_{stat.}(4)_{syst}(2)_{model} fm,$$
$$\langle r_M^2 \rangle^{\frac{1}{2}} = 0.775(12)_{stat.}(9)_{syst}(4)_{model} fm,$$

while for the polynomial group (Bernauer and Collaboration, 2011):

$$\langle r_E^2 \rangle^{\frac{1}{2}} = 0.883(5)_{stat.}(5)_{syst}(3)_{model} fm,$$
$$\langle r_M^2 \rangle^{\frac{1}{2}} = 0.778(^{+14}_{-15})_{stat.}(10)_{syst}(6)_{model} fm.$$

As can be observed in these last results, there are differences between the values of the radii found with the two groups and no explanation to this gap has been found from the A1 Collaboration. What they have presented as result so is the average of the previous values (Bernauer and Collaboration, 2011):

$$\langle r_E^2 \rangle^{\frac{1}{2}} = 0.879(5)_{stat.}(4)_{syst}(2)_{model}(4)_{group} fm,$$
$$\langle r_M^2 \rangle^{\frac{1}{2}} = 0.777(13)_{stat.}(9)_{syst}(5)_{model}(2)_{group} fm. \quad (1.18)$$

Jefferson Lab Experiment

In 2011, at Jefferson Lab, another experiment has been performed, using a recoil polarimetry for the measurement of the proton elastic form factor ratio, indicated

with the symbol $\mu_p G_E/G_M$ (Zhan et al., 2011). For that purpose, the group considered a Q^2 value in the range between 0.3 and 0.7 $(GeV/c)^2$. For this experiment it has been taken in account to work in the one-photon exchange formalism, also known as Born formalism. In this way the ratio of the transferred transverse to longitudinal polarizations is related to the proton form factors (Zhan et al., 2011):

$$R = \mu_p \frac{G_E}{G_M} = -\mu_p \frac{E_e + E'_e}{2M_P} \tan\left(\frac{\theta}{2}\right) \frac{P_t}{P_l}; \tag{1.19}$$

where:

- M_p and μ_p are, respectively, the mass and the magnetic moment of the proton;
- E_e and E_e' are the incident and scattering electron energy;
- θ_e is the electron scattering angle;
- P_t and P_l are the transverse and longitudinal component of the polarization transfer.

For conducting the experiment, an electron beam of energy equal to 1.2 GeV has been shot against a thick liquid hydrogen target. The recoil proton then has been revealed by a Left High Resolution Spectrometer, which contains a focal plane polarimeter able to measure the transferred proton polarization (Zhan et al., 2011). The radii values obtained from the global fit are:

$$\begin{aligned} \langle r_E^{2\,\frac{1}{2}} \rangle &= 0.875 \pm 0.008_{exp} \pm 0.006_{fit}\, fm, \\ \langle r_M^{2\,\frac{1}{2}} \rangle &= 0.867 \pm 0.009_{exp} \pm 0.018_{fit}\, fm. \end{aligned} \tag{1.20}$$

As can be observed from the results in 1.18, the two methods return measurements of the proton radius a little bit different, remaining anyway compatible.

1.3 Atomic Hydrogen Spectroscopy

Another method that can be used to determine the charge radius of the proton is the spectroscopy of the atomic hydrogen since the study of the hydrogen energy levels has a deeply connection with the discovery and further progress of the Quantum Mechanics. The next explanation regarding the description of the hydrogen energy levels follows the analysis presented in (Antognini, 2005).

1.3.1 Theoretical Foundations

Bohr quantization rules of the old quantum physics were created to explain the existence of the stable discrete energy levels as shown in Equation 1.21, explanation that found it's confirmation in the wave equation formulated by E. Schrödinger (Antognini, 2005).

$$E_n = -mc^2 \frac{(Z\alpha)^2}{2n^2} = -R_\infty hc \frac{Z^2}{n^2}, \tag{1.21}$$

where c is the speed of light in vacuum, n the principal quantum number, m the mass of the electron, h is the Planck constant, α is the fine structure constant and R_∞ is the Rydberg constant (Antognini, 2005):

$$R_\infty = \frac{me^4}{8\epsilon_0^2 h^3 c} = \alpha^2 \frac{mc}{2h}.$$

The energy of an absorbed or emitted photon is given by the difference between two levels, n and n', in terms of energy. The spectrum of this photon so it's given by (Antognini, 2005):

$$\frac{1}{\lambda} = \frac{v}{c} = R_\infty \frac{m_r}{m}\Big(\frac{1}{n^2} - \frac{1}{n'^2}\Big) = R_\infty \Big(\frac{1}{n^2} - \frac{1}{n'^2}\Big) \tag{1.22}$$

considering that the reduced mass for the hydrogen is $m_r = \frac{mM}{(m+M)} \simeq 0.9995\, m$, M is the mass of the proton, λ is the wavelength of the proton and ν is the frequency of the same. The different n dependence so allows the determination of both the Rydberg constant and the proton radius from at least two transition frequencies in hydrogen (Pohl et al., 2013).

Subsequently to this non-relativistic treatment, Dirac was able to bring the equation onto a relativistic plane (Beyer et al., 2013). The energy eigenvalues of a solution for a Coulomb source is given by (Antognini, 2005):

$$E_{nj} = mc^2 f(n, j) \tag{1.23}$$

with

$$f(n,j) = \left[1 + \frac{(Z\alpha)^2}{\Big(n - j - \frac{1}{2} + \sqrt{(j+\frac{1}{2})^2 - (Z\alpha)^2}\Big)^2}\right]^{-\frac{1}{2}}, \tag{1.24}$$

and j the sum of orbital and spin angular momentum of the electron. The general expression for the atomic energy levels takes so the form (Antognini, 2005):

$$\begin{aligned} E_{njl} &= mc^2 + Mc^2 + (f(n,j) - 1) m_r c^2 \\ &\quad - (f(n,j) - 1)^2 \frac{m_r^2 c^2}{2(m+M)} + \frac{1 - \delta_{(l0)}}{(j+\frac{1}{2})(2l+1)} \frac{(Z\alpha)^4 m_r^3 c^2}{2n^3 M^2}, \end{aligned} \tag{1.25}$$

where l is the orbital angular momentum.

The Lamb Shift Discovery

Then, in the 1947, W.E. Lamb and R.C. Retherford discover a discrepancy in Dirac equation due to the fact that several and important contributions have not been considered, like the effects of the quantum vacuum (Beyer et al., 2013).

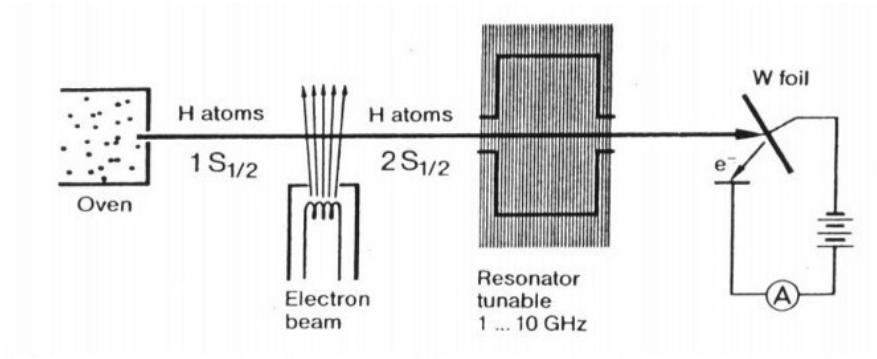

Figure 1.4: Configuration of the Lamb-Retherford experiment in 1947 (Belloni, 2014).

Indeed, energy levels with same n and j but different l should have the same energy, but they observed that this is not true for the energy levels $2S_{\frac{1}{2}}$ and $2P_{\frac{1}{2}}$ due to the interaction between the electron and the vacuum.

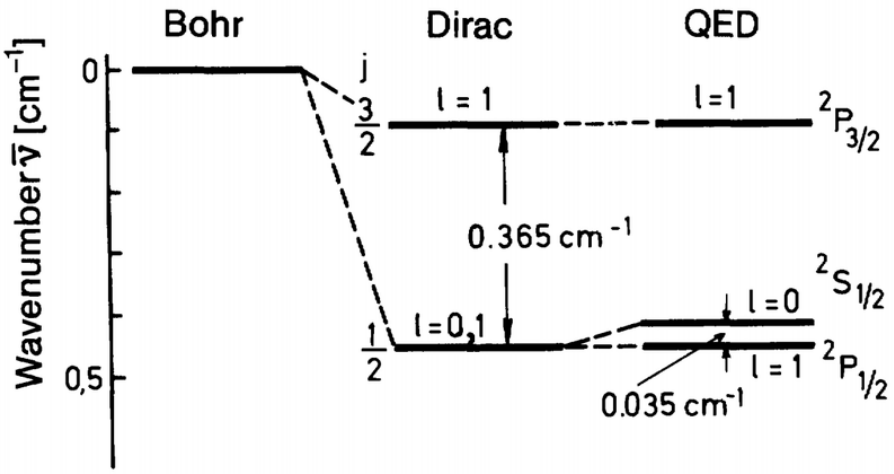

Figure 1.5: Fine structure of the energy levels of the hydrogen with the introduction of Dirac's treatment and the Lamb Shift corrections (Schlenga, 2015).

So, every variation from the expected energy level differences take the name of Lamb Shift. In general, the Lamb Shift L_{njl} is introduced in Equation 1.25, averaging over the hyperfine splitting contributions E^{hfs}_{njlF} (Antognini, 2005):

$$E^{tot}_{njlF} = mc^2 + Mc^2 + (f(n,j) - 1)m_r c^2 - (f(n,j) - 1)^2 \frac{m_r^2 c^2}{2(m+M)} + L_{njl} + E^{hfs}_{njlF}, \tag{1.26}$$

where E^{hfs}_{njlF} is the total binding energy of the level characterized by the n, j, l, F quantum numbers.

The contributions of all these terms are given below (Antognini, 2005):

- when energy differences between two levels are measured, the two first terms cancel out;
- the third term contributes to the 1S-2S energy splitting in hydrogen with about 2.5×10^3 THz;
- the forth term is about 22 MHz.

The Lamb Shift arises from QED corrections to the energy levels that can be written in form of a power series expansion in three small dimensionless parameters: $\alpha, Z\alpha$ and m/M. The main contributions to the corrections can be classified in different categories (Antognini, 2005):

- Radiative corrections: pure QED effects are considered, like self-energy and vacuum polarization for an electron in a Coulomb potential of an infinitely heavy and point-like nucleus. They depend only on α and $Z\alpha$;
- Recoil corrections: due to the finite mass of the nucleus. They arises from the introduction of the reduced mass that can not account for all recoil corrections in a relativistic two-body system. They depend on the parameters $Z\alpha$ and m/M;
- Radiative-recoil corrections: corrections that take into account the mixed radiative and recoil contributions and depend on all the parameters simultaneously;
- Finite nuclear size corrections: corrections born considering the nucleus not as a point-like object but as an object with its own structure.

The usefulness of the categorization of the different corrections arises from the fact that they can be generally treated as separated and so determined one by one. From now, just the radiative and nuclear size corrections will be considered since the first ones are those with the highest value while the latter, even if they contribute to the Lamb Shift with a value of the order 10^{-4} (Antognini, 2005), are important because of their largest uncertainty related to that of the proton radius.

At this point, it's possible to consider the difference between the electric potentials $V(r)$ of the point like and structured nucleus (Antognini, 2005):

$$\delta V(r) = V(r) - (-\frac{Z\alpha}{r}). \tag{1.27}$$

Now, it's useful consider the relation between the charged form factor and the nucleus ground state charge density (expressed in Equation 1.13), solve the Fourier Transform and describe the difference in function of the charged particle. For full explanation, see Appendix A of (Antognini, 2005).
So, transforming back to the coordinate space, Equation 1.27 takes the form (Antognini, 2005):

$$\delta V(r) = \frac{2\pi(Z\alpha)}{3} r_p^2 \delta(r) - \frac{Q\alpha}{2r^3} \frac{3(\mathbf{S}\cdot\hat{r})^2 - \mathbf{S}^2}{S(2S-1)} + \dots, \tag{1.28}$$

where **S** is the nuclear spin operator, r_p^2 the proton squared mean value and Q is the nuclear quadrupole moment. For the hydrogen case, the spin of the proton equals to 1/2 leading to $Q = 0$ and so the second term is removed. Using the non-relativistic Schrödinger wave function $\Psi(r)$ and the perturbation theory, the hydrogen level energy shifted ΔE becomes (Antognini, 2005):

$$\begin{aligned}\Delta E =& \langle \bar{\Psi}(r)|\delta(r)|\Psi(r)\rangle = \frac{2\pi(Z\alpha)}{3} r_p^2 \,|\Psi_n(0)|^2 \\ =& \frac{2(Z\alpha)^4}{3n^3} m_r^3 \, r_p^2 \, \delta_{l0} \simeq 1162(51) \frac{\delta_{l0}}{} n^3 \, kHz, \end{aligned} \tag{1.29}$$

obtained considering a proton radius of $0.895(15)\, fm$. The energy of the S-state in hydrogen can be approximated as the following formula (Antognini, 2005):

$$E(nS) \simeq -\frac{R_\infty}{n^2} + \frac{L_{1S}}{n^3} \tag{1.30}$$

where L_{1S} represents the Lamb Shift in the state 1S.

Ideally, one uses the 1S-2S transition in order to extract the proton radius because this contains the maximal 1S Lamb Shift, strongly dependent on the proton radius. Instead, one of the 2S-8S,D/12D transitions are used to extract the Rydberg constant because they contain just a smaller Lamb Shift contributions due to $\frac{1}{n^3}$ (Pohl et al., 2013).

Hyperfine Structure leading to Zemach Radius

Another finer splitting in the atomic levels that has not been considered in the Dirac treatment depends on the interaction between the electron and the nuclear angular momentum, known as Hyperfine Splitting. A simple diagram of it is shown in Figure 1.6 while in Figure 1.7 $n = 2$ energy levels of hydrogen are shown, combining Fine and Hyperfine structures.

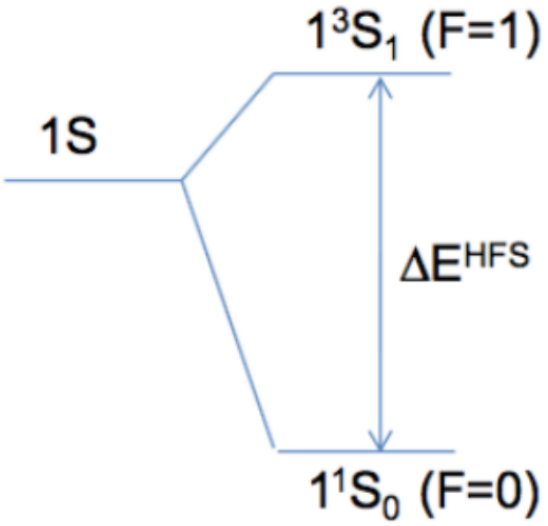

Figure 1.6: Representation of the Hyperfine Splitting states: F=0 corresponds to the singlet state and F=1 to the triplet state (Rignanese, 2019).

The hyperfine splitting of the ground state of the hydrogen atom takes the value (Dupays et al., 2003)

$$\Delta E_{exp}^{HFS} = 1420405751.7667 \pm 0.0009 Hz \tag{1.31}$$

where the relative experimental uncertainty doesn't exceed 10^{-12}. On the contrary, theoretical predictions based on the QED are less accurate.

This major uncertainty comes from the non-optimal knowledge about the proton structure. In order to have a more precise measurement, one could have followed two ways: to consider the information about the electromagnetic of the protons or to consider the hyperfine splitting of the hydrogen-like bound states of charged point-like leptons, like the muons (Dupays et al., 2003). For now just the Hyperfine Splitting of the hydrogen is treated.

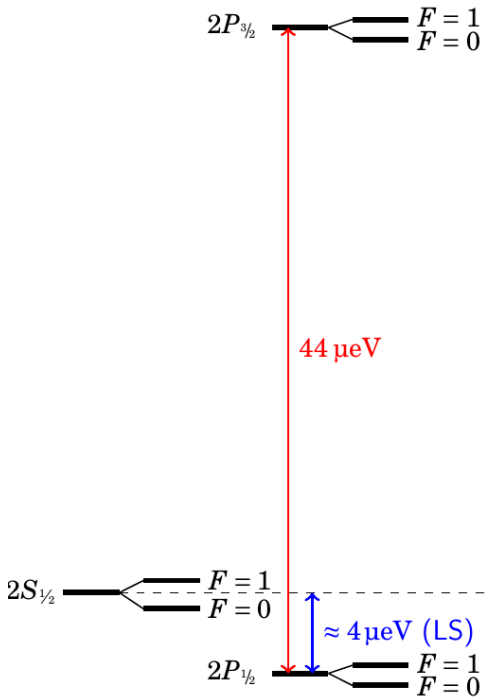

Figure 1.7: Representation of the $n = 2$ energy levels of the atomic hydrogen, including the Fine and Hyperfine Structure. In the image, LS stands for Lamb Shift, while the Hyperfine States are indicated with F=0 and F=1 (Guffanti, 2015).

So the theoretical value of the ΔE^{HFS} is composed by several components (Dupays et al., 2003):

$$\Delta E_{th}^{HFS} = E^F(1 + \delta^{QED} + \delta^{str}). \tag{1.32}$$

E^F is the Fermi splitting expressed in terms of proton and electron masses and dipole magnetic moment of the proton μ_p (Dupays et al., 2003):

$$E^F = \frac{8}{3}\alpha^4 c^2 \frac{m_e^2 m_p^2}{(m_e + m_p)^3}\mu_p \tag{1.33}$$

.

The two correction terms, δ^{QED} and δ^{str}, are related to higher order QED effects and to proton electromagnetic structure due to strong interactions. δ^{QED} takes the following form, without distinguish between α and $Z\alpha$ (Dupays et al., 2003):

$$\delta^{QED} = a_e + \frac{3}{2}\alpha^2 + \alpha^2(\log 2 - \frac{5}{2}) - \frac{8\alpha^3}{3\pi}\log\alpha(\log\alpha - \log 4 + \frac{281}{480}) + 18.984 \cdot \frac{\alpha^3}{\pi} + \ldots, \tag{1.34}$$

where a_e is the anomalous magnetic moment of the electron. In this kind of correction there is no trace of the terms that depend on the proton mass or on strong interactions, already included in δ^{str}.

The correction term δ^{str} is given by the sum of other corrections (Dupays et al., 2003):

$$\delta^{str} = \delta^{rigid} + \delta^{pol} + \delta^{hpv} \tag{1.35}$$

in which:

- δ^{pol} is the proton polarizability correction, related to the internal dynamics of the proton;
- δ^{hpv} is the hadron vacuum polarization correction, describing the strong interaction effects outside the proton;
- δ^{rigid} is the static part, accounting for the elastic electromagnetic form factor of the proton and defined as $\delta^{rigid} = \delta^{recoil} + \delta^{Zemach}$:
  - δ^{recoil} is the term related to the recoil effects depending so on m_e/m_p;
  - δ^{Zemach} is associated with the spatial distribution of the charge and magnetic moment within the proton and it takes the form (Antognini, 2005):

$$\delta^{Zemach} = -2Z\,\alpha\,\mu\langle r_{EM}\rangle \tag{1.36}$$

    calling $\langle r_{EM}\rangle$ the Zemach radius of the proton, defined as the convolution of proton charge and magnetic distributions:

$$\langle r_{EM}\rangle = -\frac{4}{\pi}\int_0^\infty \frac{dQ}{Q^2}\Big[G_E\frac{G_M(Q^2)}{\mu_p} - 1\Big]. \tag{1.37}$$

By using the $\langle r_{EM}\rangle$ expressed in Equation 1.37, it's possible to extract the value of the form factors and to compare them with the measurements obtained using the Electron Proton Scattering. Through the measurement of the proton Zemach radius and the comparison of this value with those found using variants of the hydrogen atoms as explained in Chapter 2, there will be the possibility to better understand the proton structure and to know why there are so many different outputs in the examination of the proton radius.

The values of corrections and of their uncertainty to the hyperfine splitting can be seen in Table 1.1.

Hydrogen		
	magnitude	uncertainty
E^F	1420 MHz	0.01 ppm
δ^{QED}	$1.16 \cdot 10^{-3}$	$< 0.001 \cdot 10^{-6}$
δ^{rigid}	$39 \cdot 10^{-6}$	$2 \cdot 10^{-6}$
δ^{recoil}	$6 \cdot 10^{-6}$	10^{-8}
δ^{pol}	$1.4 \cdot 10^{-6}$	$0.6 \cdot 10^{-6}$
δ^{hvp}	10^{-8}	10^{-9}

Table 1.1: Numerical values of the contributions to the Hyperfine Splitting of the Hydrogen (Dupays et al., 2003).

1.3.2 Results

In this section, two experimental results obtained with the Atomic Hydrogen Spectroscopy will be examined, one from (Bezginov et al., 2019) and the other from (Thomas et al., 2019), both performed in 2019. Here, the apparatuses used will be shown together with the results.

Even if the two results are based on the same technique, they have returned two very different results, one closer to the old measurement of the proton, the other closer to the value obtained by studying the muon hydrogen, introduced in the next chapter.

S. Thomas et al. Experiment

This experiment has been performed at LKB, in Paris, studiyng the 1S-3S transition frequency and then extrapolating the proton radius. When their result has been combined with the more precise measure of the 1S-2S transition frequency, they have noticed that the found proton radius was in agreement with the CODATA value of 2014, $0.8751(61) fm$ (Mohr, Newell, and Taylor, 2016).

The experimental setup consists of an effusive beam of atomic hydrogen produced by a radiofrequency discharge and directed colinearly with a laser beam at $205\,nm$. The laser beam propagates in a Fabry-Perot cavity under vacumm, undergoing then a frequency scan performed by an acousto-optic modulator, exciting so the 1S-3S transition of the atoms (Thomas et al., 2019). The laser beam of $205\,nm$ is obtained by sum frequency generation in a BBO (barium borate) crystal, using the TiSa laser at $894\,nm$ and the frequency-doubled Verdi laser at $532\,nm$. In order to measure the frequency of the two lasers so the apparatus contains an optical frequency comb, referenced to a hydrogen maser (Thomas et al., 2019). A picture of this experimental setup can be viewed in Figure 1.8.

The main systematic effect to face has been the second order Doppler Shift, given by (Thomas et al., 2019):

$$\Delta_{SOD} = -\frac{v^2}{2c^2}\nu_L \tag{1.38}$$

where v is the atomic velocity and ν_L the laser frequency. For hydrogen atoms, the SOD (Second-Order Doppler Shift) has been calculated to be about $-135 kHz$ (Thomas et al., 2019). To correct this effect, the atomic velocity distribution within

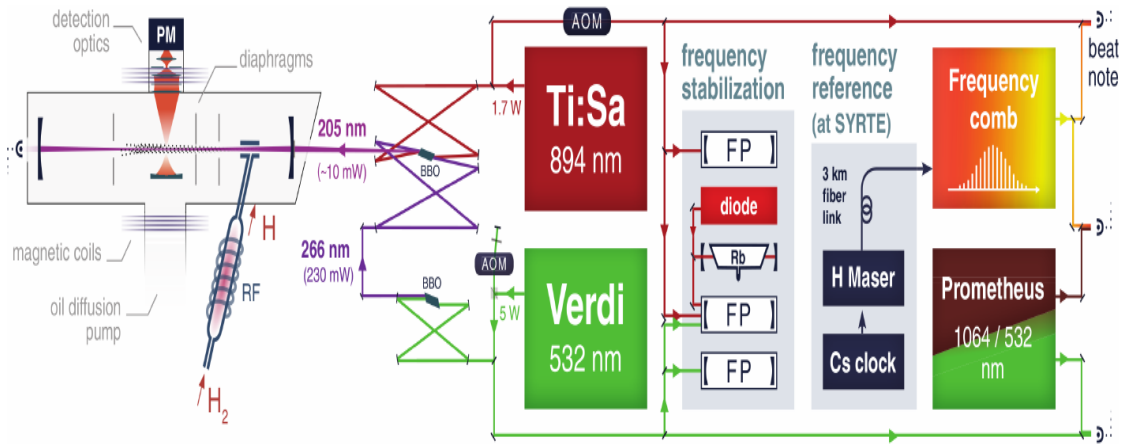

Figure 1.8: Graphic of the experimental apparatus used for the Hydrogen Spectroscopy at the LKB (Thomas et al., 2019).

the hydrogen beam is required, obtained using a magnetic field with the same direction of the hydrogen beam.

In order to fit the experimental spectra in further step, a theoretical lineshape must be extrapolated by calculating the fluorescence probability of the hydrogen atom as a function of the laser frequency (Thomas et al., 2019)

$$\nu_L = \frac{\omega L}{2\pi}.$$

By introducing the fluorescence probability, one should take in to account also the interference terms, but luckily in case of 1S-3S transition they are weak, around $0.6\,kHz$ and so they are just considered in the theoretical lineshape by shifting the obtained value of ν_{1S-3S} by $+0.6(2)kHz$ (Thomas et al., 2019).

Data sets consist of more than 2700 experimental spectra of the 1S-3S transition obtained by varying the hydrogen pressure, the laser power and the applied magnetic field in order to reduce the systematic effects mentioned before.

The Figure 1.9 shows the spectra of the 1S-3S transition in hydrogen, considering different values of the temperature, $0\,K$, $120\,K$ and $300\,K$. In this figure, the systematic effects have not been removed yet.

The resulting transition frequency is so obtained:

$$\nu_{1S-3S} = 2922743278671.5(2.6)kHz \tag{1.39}$$

In the end, combining this result with the 1S-2S transition frequency, they found that the proton radius measures (Thomas et al., 2019):

$$r_p = 0.877(13)fm, \tag{1.40}$$

a value according with that established from CODATA in 2014, but far away from the more precise and newest measures, as foretold.

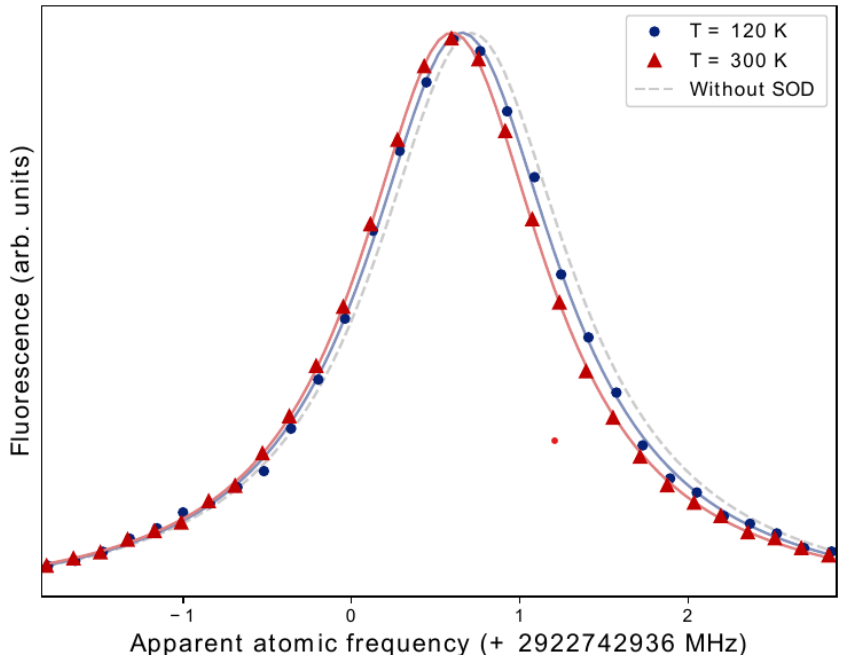

Figure 1.9: Spectra of the 1S-3S transition in hydrogen obtained with a nozzle at room temperature (red triangle) and at 120 K (blue circles). The systematic effects have not been removed. The experimental data points are fitted by a Lorentzian lineshape. The dashed line is a simulation of the line position at 0 K (Thomas et al., 2019).

1.3.3 N. Bezginov et al. Experiment

In 2019, this group of scientists decided to operate a direct measurement of the $n = 2$ Lamb Shift of the atomic hydrogen, considering the $2S_{1/2}$ and $2P_{1/2}$ transitions, shown in Figure 1.10.

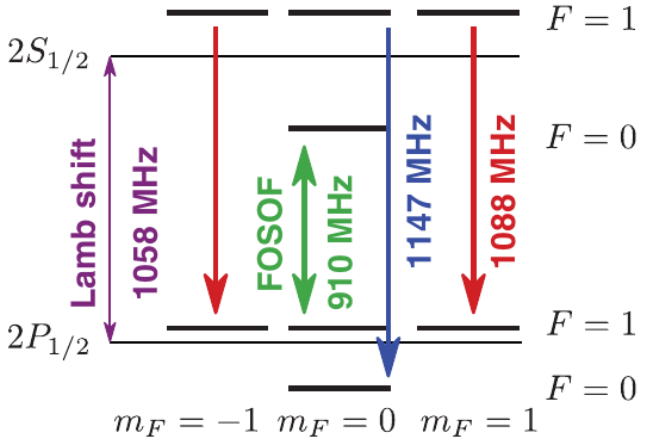

Figure 1.10: *"Scheme of the $2S_{1/2}$ and $2P_{1/2}$ states with Lamb Shift and Hyperfine states of the atomic hydrogen. The green arrow indicates the transition measured, while the red and blue represent transitions used to remove populations from $2S_{1/2}$ (F=1). F and m_F are the total angular moment and its projection along the direction of the radiofrequency fields"* (Bezginov et al., 2019)

The performed measurement is done using the FOSOF technique, working with continuously variant phases of the two separated fields. The apparatus used is described in Figure 1.11.

At the basis of this work, there is a fast beam of hydrogen atoms created by passing accelerated protons through a molecular hydrogen target.

Due to the collisions, approximately an half of the proton is neutralized into the hydrogen atom, generating a 4% of neutral hydrogen atoms in the metastable $2S_{1/2}$ state. These atoms move with a velocity that is the 1% of the speed of light, passing 70-cm-long deflector plates, where an electron beam ejects the remaining protons out of the beam (Bezginov et al., 2019).

At the beginning, all the states of $2S_{1/2}$ are populated. Now, two radiofrequency cavities, with their own radiofrequency intensities and frequencies, have the job to transfer the 99.9% of the F=1 atoms to the $2P_{1/2}$ such that just the F=0 state survives the passage. The $2S_{1/2}$ atoms then are driven to the $2P_{1/2}$, passing through a pair of waveguides. The resulting $2S_{1/2}$ (F=0) atoms are so detected by using a gas-ionization detector and their number is obtained by mixing them in an electric field and observing the resulting Lyman-α photons (Bezginov et al., 2019).

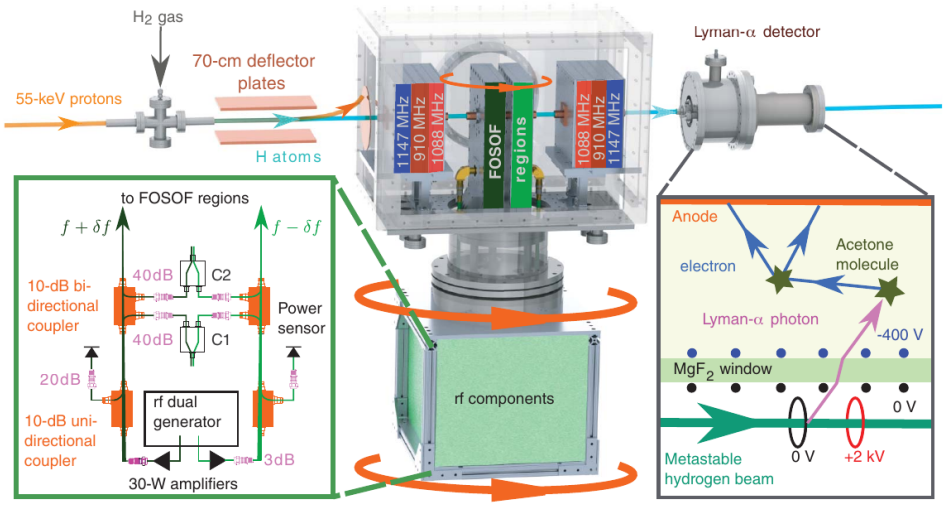

Figure 1.11: Apparatus used for the measurement of the proton radius. From left to right, it's possible observed the molecular hydrogen gas, the 70-cm-plates, the two FOSOF regions and the Lyman-α detector. The radiofrequency component is placed under the FOSOF regions. The entire FOSOF system is able to rotate up to 180°. In the squares, additional information about FOSOF regions and the detector are included. (Bezginov et al., 2019)

In order to achieve precise measurements, the phase difference $\Delta\theta$ has been measured with an accuracy better than $1\,mrad$. Using a so high precision, however, can cause phase shifts due to time delays and filtering. To remove the possible phase shifts, they employ three different techniques (Bezginov et al., 2019):

- every few seconds, a frequency change is applied such that the phase shifts related to the bandwidth is avoided;

- every hour, the FOSOF region is rotate of 180° with the aim of flipping $\Delta\theta$ such that the average $\bar{\Delta\theta}$ cancels any errors in the radiofrequency system;
- in the end, to be sure to have the correct $\Delta\theta$, the beat signal is measured twice: once by combining the radiofrequency field before entering the FOSOF regions and once when they have come back from those regions.

In this experiment, other corrections have been faced, like the time dilation and the Stark shift, the evaluation of which can be seen in the full treatment of (Bezginov et al., 2019).

In the end, the atomic resonance frequency has been measured, obtaining (Bezginov et al., 2019):

$$f_0^{avg} = 909.8717(32)\, MHz \tag{1.41}$$

where the uncertainty of $3.2\, kHz$ comes adding up all the contributions already mentioned.

From this measurement it is possible to extract the proton radius (Bezginov et al., 2019)

$$r_p = 0.8333(10) fm. \tag{1.42}$$

As can be seen, this value is very different from those that had been found until now. This result indeed is in accordance with the value of the proton radius measured using the muonic hydrogen, treated in Chapter 2, value that in 2010 has shaken the foundations of the scientific community. By considering all the experiments treated, just this has shown a different result, while the others agree with the CODATA value of $0.8751(61)\, fm$ (Mohr, Newell, and Taylor, 2016): this means that is possible to obtain more accurate precision of the proton radius by employing newest technologies, even working with atomic hydrogen.

Chapter 2

Muon

The subject under study is the Muon, a particle that has become of fundamental importance to determine the proton radius.
Initially, the muon and the measurement of the Lamb shift in muonic hydrogen was taken into account just for testing the electron vacuum-polarization (Pohl et al., 2013).
In order to perform the laser spectroscopy of the interesting transitions, the muonic hydrogen atoms must be in the metastable $2s$ state and many experiments tried to study this effect, failing. The first successful experiment has been performed in 2010 and takes the name of CREMA: Charge Radius Experiment with Muonic Atoms, at the PSI (Pohl et al., 2010).

So, in this chapter, at first the general properties of the muon are described, as the mass and lifetime of the muons.

A brief description of the production and of the sources of muon has been written, followed by the description of the interaction between the muon and matter and the possible outcomes.

In the end, the CREMA have been treated, the first attempt in 2010 and also that of the 2013, which is an update of the first experiment.

2.1 General Notions

The muon was discovered in 1937 by Carl David Anderson and its student Seth Neddermeyer, classifying it as unstable elementary particles. There exist two charge types of this kind of particle, the positive μ^+ and the negative μ^- ones, with the following characteristics (Nagamine, 2003), shown also in Table 2.1:

- Spin equal to $\frac{1}{2}$;
- An intermediate mass between the value of the proton ($\frac{1}{9}$ of m_p) and of the electron (207 of m_e), which makes it the second particle with the smallest mass;
- A lifetime of 2.2 μs, which is the longest after that of the neutron;
- It belongs to the lepton family, like the electron and the τ-particle;
- Electromagnetic and weak interactions govern the mutual influence between the muon and other particles or matter.

	μ^+	μ^-
Charge	$+1$	-1
Spin	$\frac{1}{2}$	$\frac{1}{2}$
Mass (m_μ)	206.768277(24) (m_e)	105.6583715(35) (MeV)
Magnetic moment (μ_μ/μ_p)	3.18334513(39)	
Free decay lifetime (10^{-6})	2.169803(22)	2.1948(10)

Table 2.1: Muon properties (Nagamine, 2003).

2.1.1 Mass and Size of the Muons

According to the double charge nature of the muons, there are different ways to measure the mass of the m_{μ^+} and of the m_{μ^-}.

The first can be determined by measuring the energy intervals between the $1s$ and $2s$ electron quantum levels (ΔE_{1s-2s}) in muonium.
The second cannot be measured in this way, but just measuring the energy intervals between the atomic states formed by the μ^- around a nucleus, generating the so-called muonic atom.

Two methods can be used to measure the sizes of the two charged muons: one uses the high-energy collision experiments implementing e^+e^- colliders; the other uses high-precision measurements of muon properties (anomalous gyromagnetic ratio of the muon, upper limit upon the flavor non-conserving decay $\mu^+ \rightarrow e^+ + \gamma$) (Nagamine, 2003).

The results of these experiments lead to 10^{-16} (Nagamine, 2003) for the size of the muons. Due to this small result, the idea of the point-likeness of the muon is acceptable. A picture of the mass' particles, including the mass of the charged muons, can be observed in Figure 2.1.

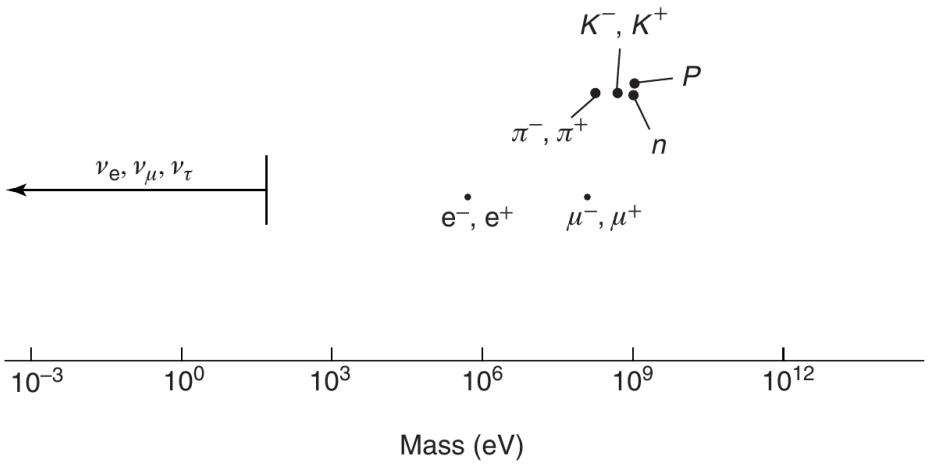

Figure 2.1: Masses of various particles (Nagamine, 2003).

2.1.2 Lifetime of the Muon

In order to measure the lifetime of positive muon, it can be measured by considering the time spectrum of the decay positrons (Nagamine, 2003):

$$\mu^+ \rightarrow e^+ + \bar{\nu}_\mu + \nu_e \, (in\, vacuum),$$
$$\mu^- \rightarrow e^- + \nu_\mu + \bar{\nu}_e \, (in\, vacuum)$$

where ν_e and ν_μ are electron and muon neutrinos, while $\bar{\nu}_e$ and $\bar{\nu}_\mu$ are the corresponding anti-neutrinos. This measurement is performed in reference to the time of μ_+ stopping in some target material, with the assumption that no changes occurred from the vacuum case (Nagamine, 2003).

The time distribution of the positrons' decay thanks to the weak interaction is given by (Nagamine, 2003):

$$N_e(t) = N_e(0) e^{-\frac{t}{\tau_\mu}}. \tag{2.1}$$

The strength of this force is strongly governed by the Fermi Constant (G_F), given by (Rignanese, 2019):

$$\frac{G_F}{\sqrt{2}} = \frac{g^2}{8 M_W^2} \Big(1 + \sum_i r_i\Big), \tag{2.2}$$

where $1/M_W^2$ is the three-level propagator corresponding to the W boson exchange and g the weak coupling (Rignanese, 2019). Together with the summation term, the electro-weak interactions have been taken into account.

One measurement of the lifetime of the positive muon has been performed in 2013 at PSI, under the name of MuLan experiment (Rignanese, 2019):

$$\tau_\mu = 216980.3 \pm 2.2\, ps. \tag{2.3}$$

On the contrary, the measurement of the negative muon can't be performed in a target material but just in the vacuum, due to the nuclear capture processes. For this reason, a measurement of this parameter is more difficult to estimate with a low uncertainty. An unconventional way to measure the lifetime of the negative muon is to consider it in flight compared to that of the μ^+ (Nagamine, 2003).

A scheme of the lifetimes of some particles, together with those of the negative and positive muons, is shown in Figure 2.2.

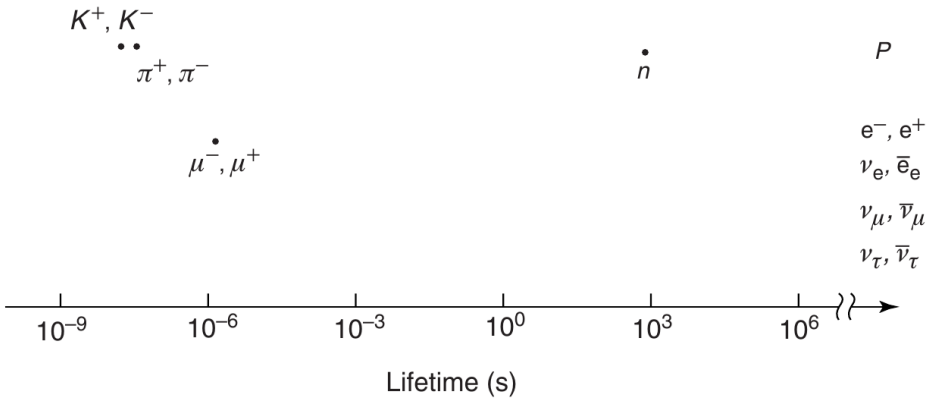

Figure 2.2: Lifetimes of various particles (Nagamine, 2003).

2.2 Muon Sources and Production

Depending on the quantity of energy used, different kinds of muons are produced. For example, using high energy beams it's possible to produce just cosmic-ray muons while, at low energy, accelerator-producing muons are almost exclusively used, desirable for their short stopping power of the order of $mm - cm$. Some kinds of muons are present in Figure 2.3.

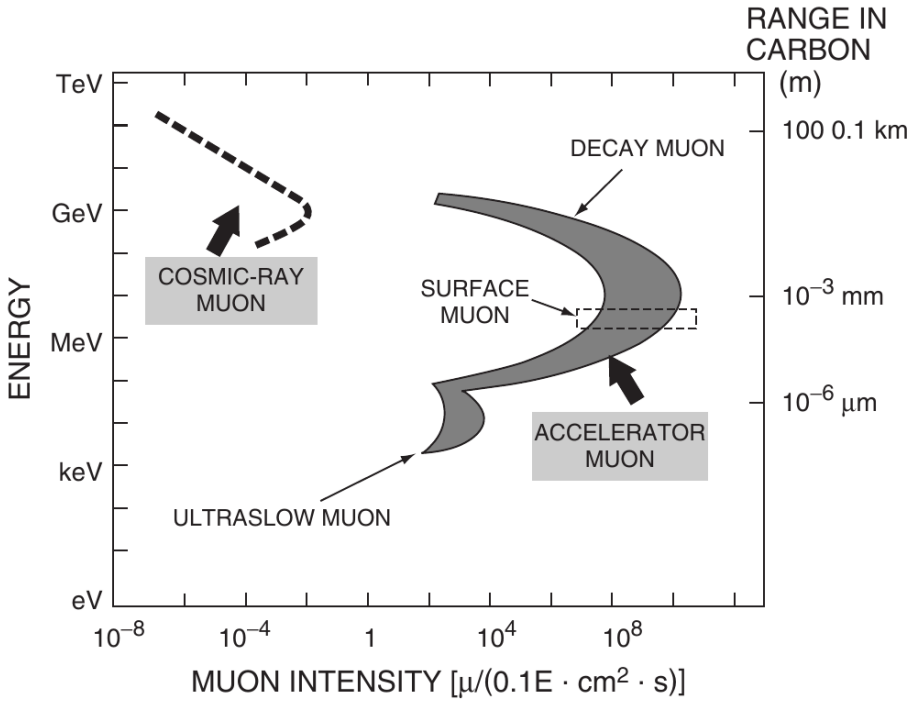

Figure 2.3: Scheme of cosmic-rays and accelerator producing muons, characterized by the ranges of energies in function of the muon intensities (Nagamine, 2003).

To produce muons, it's required the decay of pions as shown in Equation 2.4, generated by the interaction between accelerated particles and nuclear targets (Rignanese, 2019).

$$\begin{aligned} \pi^+ &\rightarrow \mu^+ + \nu_\mu \\ \pi^- &\rightarrow \mu^- + \bar{\nu}_\mu \end{aligned} \tag{2.4}$$

The primary beam and the target employed alter the spectrum and the angular momentum of the pions and this means that the decay length of pion with momentum p_π is given by the equation (Nagamine, 2003):

$$L_\pi(cm) = c\beta\gamma\tau_\pi = 5.593 \times p_\pi \frac{MeV}{c}, \tag{2.5}$$

where $\tau_\pi = 2.6 \cdot 10^{-8} s$ is the mean lifetime of the pion at rest.

The pion's momentum considered for the production of the muons must be in the range $100 - 200 MeV/c$, leading to a decay length of $L_\pi = 5.6 - 11.2\, m$ (Nagamine, 2003).

In the $\pi \rightarrow \mu$ decay, the momentum of the muon is different in the pion and laboratory frame. In the first, the momentum is equal to $29.8\frac{MeV}{c}$ and its direction is isotropic. In the last, instead, the muon momentum has a flat distribution within two limits that correspond to the Forward (F_W) and Backward (B_W) decays in the pion rest frame (Nagamine, 2003):

$$\begin{aligned} p_\mu^{F_W} &= \frac{(\beta_\pi + \beta_\mu^*)p_\pi}{[\beta_\pi(1+\beta_\mu^*)]} \\ p_\mu^{B_W} &= \frac{|\beta_\pi - \beta_\mu^*|p_\pi}{[\beta_\pi(1+\beta_\mu^*)]} \end{aligned} \tag{2.6}$$

where β_μ^* is the muon speed corresponding to its momentum from pion decay at rest.

The muons, within these limits, move along the pion directions with a definite polarization of $+1$ and -1, respectively. In the definition of a decay muon channel, one should consider that it consists of (Nagamine, 2003):

- A system for pion collection, able to select the decay length and inject them into the decay section;
- while in flight, the pions decay in muons in the decay section, characterized by a length comparable to L_π;
- then, a muon extraction system selects the muons originated from the pion decay and transports them to the target station.

A picture of the decay muon channel can be observed in Figure 2.4.

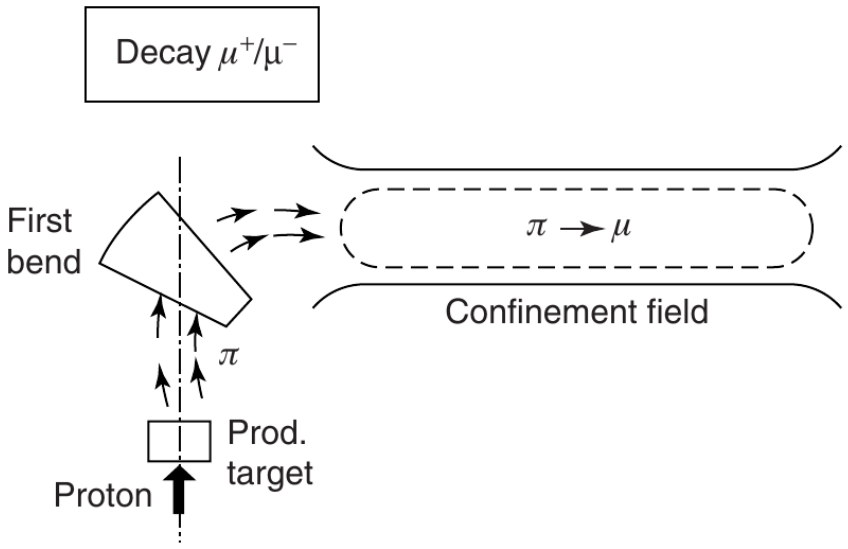

Figure 2.4: Scheme of the muon sources, involving energetic protons from accelerators (Nagamine, 2003).

For what concerns the method to delivery the muons, it can be of two types: pulsed muon method and continuous muon method. In the pulsed method, the muon beam is stopped inside the target material, by which the muon-related observable can be detected (Nagamine, 2003).
In continuous muon method, the arrival of each muon is identified and together with it each muon-associated element is detected.
There are several advantages of using the pulsed method instead of the continuous, such as (Nagamine, 2003):

- the measurement of the muon decay events over a long time range;
- the coupling of the muon pulses together with extreme experiment conditions;
- phase-sensitive detection of weak signals, even in presence of large white-noise.

Some advantages also characterize the continuous mode, like the correlation measurements with the muon-related events and the higher time resolution with respect to the pulsed muon mode (Nagamine, 2003).

2.3 Muons in Matter

Let's consider either μ^+ or μ^- and suppose to introduce it into a condensed matter. At energies higher than few keV there is not much difference between the two charged muons and the ionization is the major process of energy loss, described by the Bethe formula (Nagamine, 2003):

$$-\frac{dE}{dx} = 4\pi N_a r_e^2 \, m_e c^2 \rho \, \frac{Z}{A} \frac{1}{\beta^2} \Big[\ln(\frac{2m_e \gamma^2 \nu^2}{I}) - \beta^2 \Big] \tag{2.7}$$

where N_a = Avogadro number, $r_e = 2.817 \times 10^{-13}\, m$ is the classic range of the electron, m_e = electron mass, Z, A and ρ are, respectively, the charge, the atomic weight and density of the absorbing material.
Thanks to this equation, it's possible to determine quantitative information about the range of the muon, indicated with R_0.
By taking a momentum range between $20 - 70 MeV/c$, the muon range is known to be proportional to $p^{3.5}$ (Nagamine, 2003). The variation $-dE/dx$ is inversely proportional to the muon speed in the ionization process, imposing a minimum ionization to about $200\, MeV$.
On the opposite, around the $10\, keV$ the muons are not able anymore to ionize the atoms since their speed is not enough.
During the slowing-down processes, the muon beam is subjected to both transversal and longitudinal spread expressed as functions of R_0, giving form to a three-dimensional muon stopping region (Nagamine, 2003):

$$D_{//} = 2.6 \times 10^{-22} R_0^{0.94},$$
$$D_{\perp} = 7 \times 10^{-2} R_0^{0.92}$$

Considering energies below few keV, the behavior of the two charged muons tends to change one from the other.
The μ^+ has two possibilities, depending on the type of the material used (Rignanese, 2019):

- in gases, insulators and most semiconductors, the neutral bound state Mu is formed. Mu means Muonium, a hydrogen like atom composed of μ^+ and electron. After its formation, Mu is decelerated via elastic collision with the surrounding atoms;

- in some metals, no stable Mu can be generated due to the strong collisions of the μ^+ and the conduction electrons. At the end of the slowing-down process, the μ^+ and Mu reach in some way an equilibrium and also a bound state can be formed between μ^+ or Mu and the atoms (or even molecules) of the target materials.

The μ^-, instead, at the end of the ionization process is strongly caught by the electric field of the nuclei. Due to this attraction, the μ^- replaces one of the innermost electrons of the K shell, to form a muonic atom. Until the end of the processes, the polarization of the negative muon remains similar to that of the positive muon, keeping almost its totality. When the formation of muonic atom begins, the μ^- polarization reduces significantly (Nagamine, 2003).

2.3.1 Muonic Atom

After the end of slowing down processes, the negative muon is captured by the atom of the target material, taking the place of one of the innermost electrons and forming the muonic atom at excited state with critical quantum number (Nagamine, 2003): $n_{cri} = \sqrt{m_\mu/m_e} \cong 14$.

When this happens, the radius $R_\mu(1s)$ and the binding energy $E_\mu(1s)$ of the ground state of the μ^- are given by the point-like approximation (Nagamine, 2003):

$$\begin{aligned} R_\mu(1s) &\cong \frac{270}{Z} \times 10^{-13}\, cm \\ E_\mu(1s) &\cong 13.6 \times 207 \times Z^2\, eV \end{aligned} \tag{2.8}$$

where Z is the atomic number of the atom.

Most experiments are performed by using pure elemental or isotopic targets, even if it's convenient in some cases to use targets with two or more elements. The approximations shown in Equation 2.8 are valid in many cases, but some corrections are needed in case of heavier atoms, like Fe, Cu and so on (Nagamine, 2003).
The first measurement of the so called muon capture has been shown by Fermi and Teller (Measday, 2001) where it has been proved that the probability of being capture is proportional to the atomic number, Z. So the atomic capture probability takes the form (Measday, 2001):

$$A\Big(\frac{Z_1}{Z_2}\Big) = 0.6\rho(1+\alpha\rho)\Big(\frac{Z_2}{Z_1}\Big)^{\frac{1}{8}}(1+5.53V^{5.45}10^{-5}) \tag{2.9}$$

where ρ is the density expressed in $g\,cm^{-3}$, V is the valency of the metal and α is a parameter that differs for various values of Z_1, as can be seen in Table 2.2.

Materials	Z_1	α
	≥ 18	0
Oxides with metal	< 18	0.164
Chlorides with metal	< 18	0.222

Table 2.2: α parameter's values for different values of Z_1 (Measday, 2001).

One case apart is the Hydrogen since a neutral system μp is generated when a proton captures the muon. This μp can easily penetrate nearby atoms, where the muon is released and transferred to higher Z nucleus.

2.3.2 Nuclear Capture Rate

The lifetime τ_N of the ground state also depends on the atomic number of the nucleus, where two antagonist rates (or processes) take place: the free muon decay (Λ_d) and the nuclear muon capture (Λ_c) (Nagamine, 2003):

$$\tau_N^{-1} = \Lambda_d + \Lambda_c \tag{2.10}$$

The nuclear capture rate is proportional to the μ^- spatial density at nucleus and to the proton number of the nucleus. This means that Λ_c follows the Z^4 law and it is equal to (Nagamine, 2003):

$$\Lambda_c = \Lambda_1 Z^4, \tag{2.11}$$

the extended form of which is given by the Primakoff formula (Suzuki, Measday, and Roalsvig, 1987):

$$\Lambda_c(A, Z) = Z_{eff}^4 X_1 \Big[1 - X_2 \Big[\frac{A - Z}{2A}\Big]\Big], \tag{2.12}$$

where X_1 is the muon capture rate in hydrogen, X_2 takes into account the Pauli exclusion principle for nuclear environment.
However, this dependence of Z^4 is no longer available for heavier nuclei and some corrections must be taken into account. In order to express the corrections, the Goulard and Primakoff equation must be used (Suzuki, Measday, and Roalsvig, 1987):

$$\Lambda_c(A, Z) = Z_{eff}^4 \, G_1 \left[1 + G_2 \frac{A}{2Z} - G_3 \frac{A - 2Z}{2Z} - G_4 \left(\frac{A - Z}{2A} + \frac{A - 2Z}{8AZ}\right)\right]. \tag{2.13}$$

Some values of the parameters used in equations 2.12 and 2.13 are expressed in Table 2.3.

Formula	Parameters	Values
Primakoff equation	X_1	$170\,s^{-1}$
	X_2	3.125
Goulard and Primakoff	G_1	261
equation	G_2	-0.040
	G_3	-0.26
	G_4	3.24

Table 2.3: Parameters of equations 2.12 and 2.13 belonging to the TRIUMF Data (Suzuki, Measday, and Roalsvig, 1987).

2.3.3 Muonic Capture

Once the muonic capture has occurred, the muon cascades down to the $1s$ ground level in a time scale of $10^{-13}s$ (Measday, 2001), but two radiative processes enter in conflict (Nagamine, 2003):

- the Auger processes emitting low-energy electrons from atom's innershell, dominating in the first part of the cascade:

$$(\mu^- Z)_n + Z' \rightarrow (\mu^- Z)_{n'} + Z'^{+} + e^-;$$

- the emitting X-ray photons, starting to dominate around n = 5:

$$(\mu^- Z)_n \rightarrow (\mu^- Z)_{n'} + \gamma.$$

X-ray emissions can be very useful tools for various kind of experiments, but the knowledge of their characteristics must be acquired. At first, the energy levels for a point-like nucleus, observable in Figure 2.5, are given by (Measday, 2001):

$$E_{n,j} = -\frac{m_\mu c^2}{1 + m_\mu/A}\frac{(Z\alpha)^2}{2n^2}\left[1 + \frac{(Z\alpha)^2}{n}\left(\frac{n}{j + (1/2)} - \frac{3}{4}\right)\right], \tag{2.14}$$

with α the fine-structure constant and j the total angular momentum quantum number, equal to $|l \pm 1/2|$, according to the direction of the electron spin.

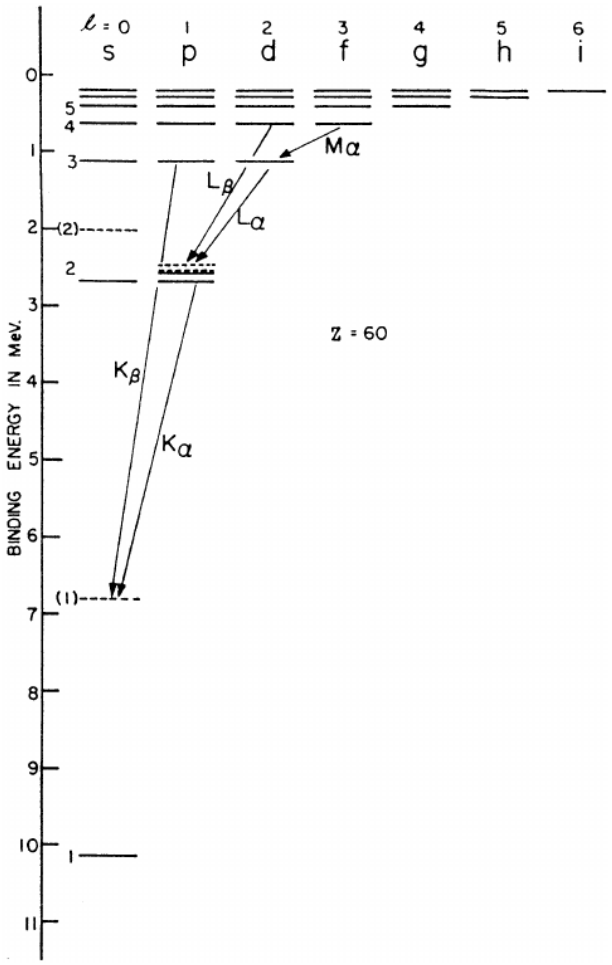

Figure 2.5: Levels of the muonic atoms, including the notation for X-rays (Measday, 2001).

The binding and the energy of the X-rays are reduced when the muon is in the $1s$ ground-state since the two radii are comparable, the one of the muon and that of the nucleus. In general, the most common transitions are those for which $\Delta n = 1$, like $4f - 3d$, $3d - 2p$ and others, but higher transitions can also occur at lower intensities. So, the observable lines that have as final state the $1s$ ground-state are called Lyman series, as in the common atomic notation, while those that have the $2s$ ground-state as final are called Balmer series. A common configuration of the Lyman series for the muon X-rays can be seen in Figure 2.6.
For higher n levels, the situation is a little bit different since the inner K electrons

act as a screen and this means that the binding is reduced, even if it can be classified as a small effect.

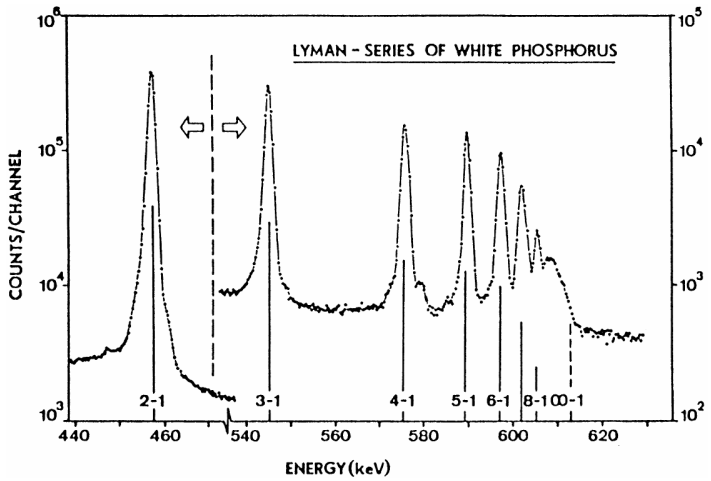

Figure 2.6: Configuration of the Lyman series of muonic X-rays (Measday, 2001).

Another factor related to the muonic X-rays of particular interest can be their intensity since, in most of the elements, the muon must make $np - 1s$ transitions, useful for example to know the efficiency of a germanium detector working in a very wide range of intensities, as explained in (Measday, 2001).

Some problems, related to the X-rays intensity, must be taken into account. The first is the presence of anomalously low X-rays due to the fact that the X-rays generated from deformed nuclei spread over complex fine structure (Measday, 2001). Even the isomer shift is a problem. The isomer shift, or the variation of few keV of the energy of transitions, is generated from the nuclear de-excitation in presence of the muon (Measday, 2001).
Another problem is related to the fine structure intensity since the levels not necessarily are statistically populated but can have intensity ratios quite different from those that one should expect (Measday, 2001).
In general, these are the difficulties encountered and also that must be avoided in the decision of the elements used for the efficiency calibrations.

2.4 Experiments

In this section, two versions of the same experiment (one in 2010 and the other in 2013) are considered, proving that a different proton radius with respect to the previous accepted value can be found using the muonic hydrogen.

The (Pohl et al., 2010), known as CREMA, is the first experiment in history that successfully shown the presence of the long-lived muonic hydrogen atoms in the $2s$ state, fundamental requirement for the determination of the $2s \rightarrow 2p$ transitions of the muonic hydrogen atoms.

2.4.1 CREMA

The first experiment demonstrating a value of the proton radius lower than the previous accorded was the known CREMA experiment, performed in 2010 at the PSI, in Switzerland. The expected value of proton radius was $0.8768(69)\, fm$ but they were able to found $0.84184(67)\, fm$, or even 5.0 standard deviations lower (Pohl et al., 2010).

Until 2010, the measurement of the proton radius was obtained by considering the Lamb shift of the Hydrogen atoms.
Here, the first difference. Instead of using the hydrogen atoms, the muonic hydrogen atom has been used, since its smaller Born radius enhances the effect related to the ordinary atomic hydrogen (Pohl et al., 2010).

Experiment and Apparatus

A new beam-line for low-energy negative muons, about $5\, keV$ kinetic energy, has been used. The muons are guided into a $5\, T$ solenoid, allowing the system to detect the single muons and generating a trigger for the pulsed laser system (Pohl et al., 2010). A scheme of the muon beam is shown in Figure 2.7.

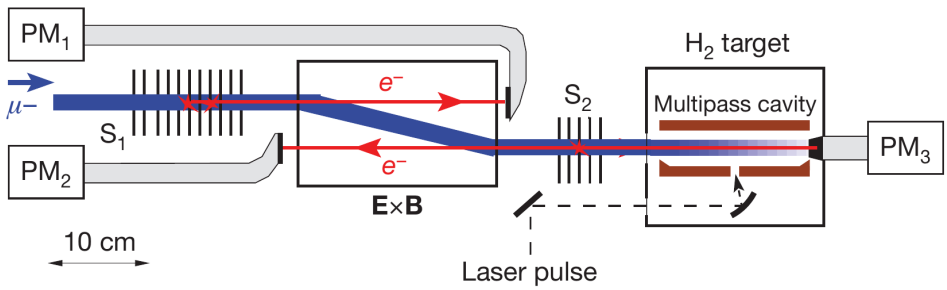

Figure 2.7: Representation of the muon beam used. The muons enters the final stage of the muon beam line, passing through two foils, S_1 and S_2. The released electrons are separated from the slower muons, thanks to the electric field perpendicular to the magnetic one (Pohl et al., 2010).

Once the muons have been separated by the faster electrons, a gas target filled with gaseous or liquid hydrogen at pressure of $1\, hPa$ stops the muons, giving birth to highly excited muonic hydrogen atoms (Pohl et al., 2010).
$0.9\, \mu s$ after the muon stop, a short laser pulse, observable in Figure 2.8, with a tunable wavelength around $6\, \mu m$ surrounds the target gas volume, inducing

$2s \rightarrow 2p$ transitions on resonance, with emission of a $1.9\,keV$ X-ray. This short laser pulse is generated by a thin disk laser that pumps a Ti:sapphire oscillator-amplifier laser. These pulses, initially at $\lambda = 708\,nm$, are converted to $\lambda = 6\,\mu m$ in the Raman cell (Pohl et al., 2010).

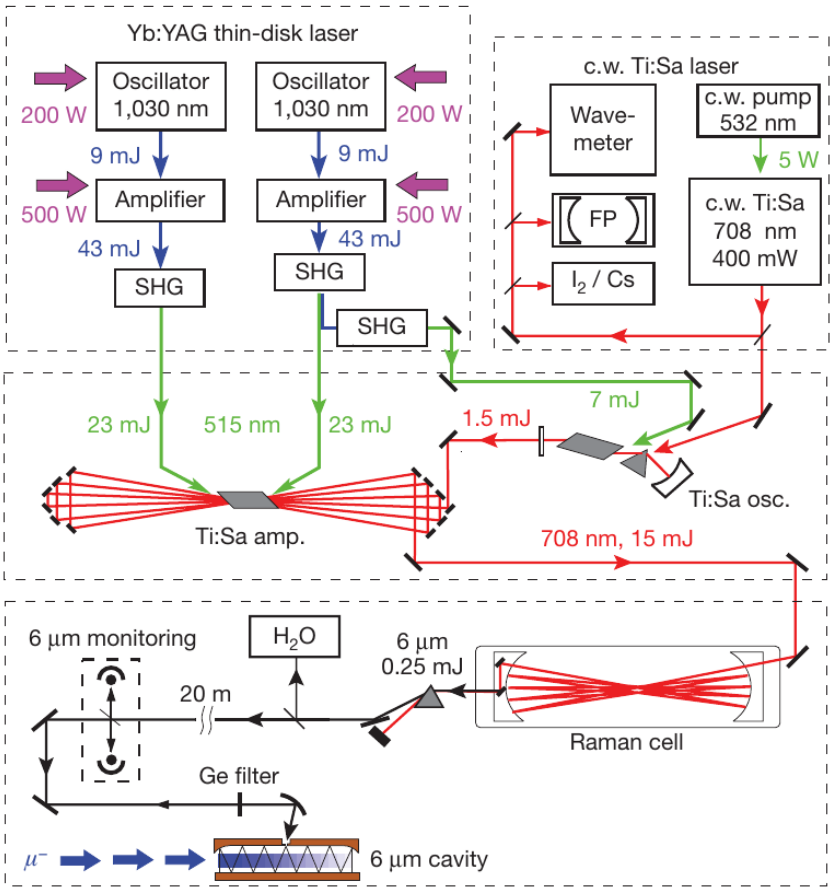

Figure 2.8: Representation of the Laser System. The continuous wave light of the Ti:Sa ring laser is used to seed the pulse Ti:Sa oscillator. At the same time, the thin-disk lasers are triggered by the detected muon. The emitted light then pumps both the Ti:Sa oscillator and amplifier, releasing $5\,ns$ short pulses at a certain wavelength, shifted by the Raman Cell to the desired value $\lambda = 6\,\mu m$ (Pohl et al., 2010).

Almost all the newly formed atoms de-excite quickly, reaching the $1s$ ground-state, while a tiny fraction of them reaches the $2s$ state. For the prefixed purpose of the experiment, the lifetime of the $2s$ state of the muonic hydrogen, τ_{2s}, must be known.
Without collisions, the $2s$ lifetime would be equal to the muon lifetime of $2.2\,\mu m$. In H_2, where the collisions are present, the $2s$ is strongly shortened leading to $\tau_{2s} \approx 1\,\mu s$ at the pressure of $1\,hPa$ (Pohl et al., 2010). This value of the pressure has been decided since it's a way to both maximize the τ_{2s} and to minimize the muon stop volume, minimizing at the same time the required laser pulse energy (Pohl et al., 2010).

Results

In order to extract and measure the proton radius, the number of events detected as a function of laser frequency must be constructed. To do this, the continuous wave associated to the Ti:sapphire laser is set to a free spectral range (FSR) of $1497.332(3)\,MHz$ (Pohl et al., 2010). To obtain the resonance spectrum, first the accumulated time spectrum of K_α events has been recorded for each laser frequency with a time window of $75\,ns$, visible in Figure 2.9.

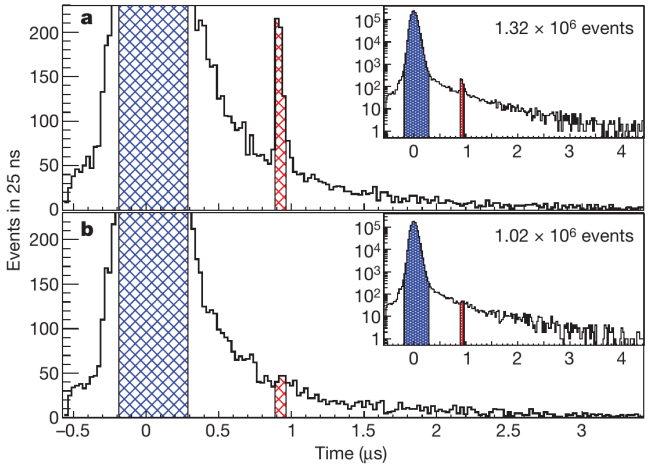

Figure 2.9: Spectrum of the recorded events, in condition of resonance and off resonance. The time window considered is from $0.887\,\mu s$ and $0.962\,\mu s$, where the muonic atoms are represented with the red line. X-rays are instead showing in blue (Pohl et al., 2010).

The 99% of the muons are contained in the large peak, useful to normalize the laser wavelength to the number of muonic hydrogen atoms (Pohl et al., 2010). By plotting the number of K_α events recorded in the time windows, it's possible to obtain the Resonance Curve, shown in Figure 2.10.

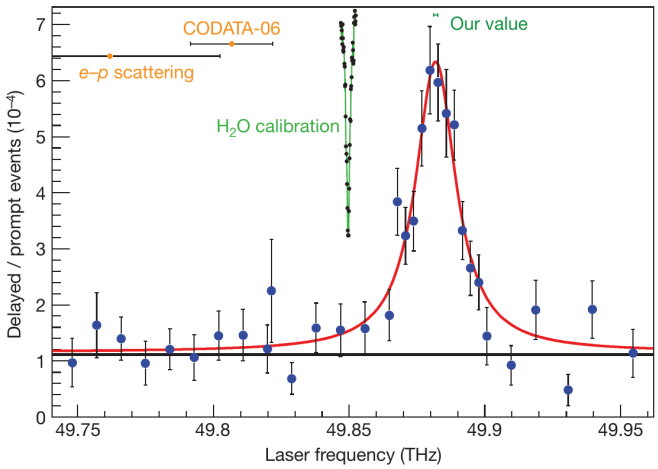

Figure 2.10: The blue circles represent the number of the events as a function of the laser frequency. The red line represents the Lorentzian on top of a flat background, returning the $\chi/d.f. = 28.1/28$, where d.f. stands for degrees of freedom. The error bars correspond to ± 1 standard deviation (Pohl et al., 2010).

The centroid position has been found at the value of $49,881.88(70)\,GHz$, but the centroid position of the $2s^{F=1}_{1/2} \rightarrow 2p^{F=2}_{3/2}$ transition must contains also the quadratic sum of the statistical and systematic uncertainties, leading to a centroid position set at $49,881.88(76)\,GHz$ (Pohl et al., 2010). The found frequency will correspond to an energy of $\Delta E = 206.2949(32)\,meV$, obtaining a proton radius $r_p = 0.84184(69)\,fm$.

2.4.2 Update of the Result

In 2013, the CREMA experiment has been re-performed, measuring the singlet and triplet transition frequencies, corresponding respectively to $2s^{F=0}_{1/2} \rightarrow 2p^{F=1}_{3/2}$ and $2s^{F=1}_{1/2} \rightarrow 2p^{F=2}_{3/2}$, as shown in Fig. 2.11.

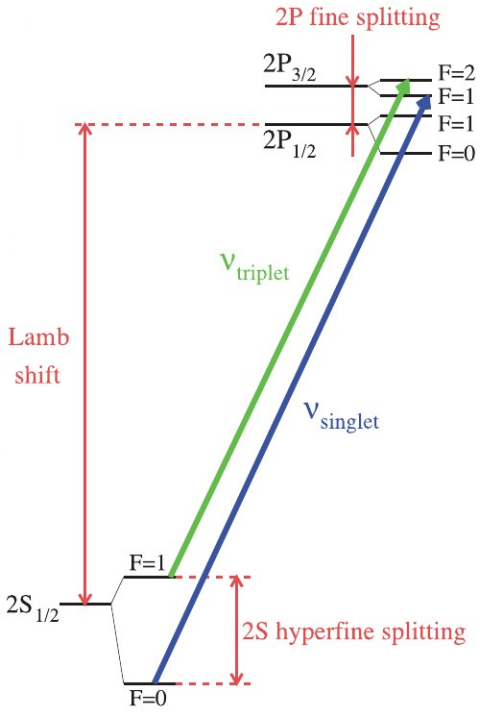

Figure 2.11: Energy levels of $2S$ and $2P$ states with the corresponding singlet and triplet transition frequencies (Antognini et al., 2013).

The transition frequencies so measured are (Antognini et al., 2013):

$$\nu_s = 54611.16(1.00)^{stat}(30)^{sys}\,GHz,$$
$$\nu_t = 49881.35(57)^{stat}(30)^{sys}\,GHz,$$

where *stat* and *sys* are the statistical and systematic uncertainties.

By summing and subtracting these two measurements, an independent assessment of the pure Lamb Shift and of the hyperfine splitting of the 2s state can be obtained.

From the obtained measurements, the Zemach Radius is measured, $r_z = 1.082(37)\,fm$, while the charge proton radius is extracted and results to be $r_E = 0.84087(39)fm$, reaching not only a lower value with respect to the result of 2010 but even a lower uncertainty (Antognini et al., 2013).

Chapter 3

FAMU Experiment

The Physics of Muonic Atoms is born in response to the proton radius puzzle, trying to use the muonic atoms to explore the dimensions of the proton like the proton Zemach radius.
In order to do so, the objective of the FAMU group is to measure the hyperfine splitting of the μp ground state from the moment that, as explained in the previous chapters, the effect of the proton finite size affects the hyperfine transition energy. The physics, treated before, is briefly explained:

At first, in a mixture of hydrogen and higher-Z gas, the incident low momentum muons are stopped and the muonic protons μp can be generated in an excited level, followed by their de-excitation at the ground state ($F = 0$).
At this point, a variable frequency laser is tuned to the resonance-energy of the hyperfine splitting $\Delta E^{hfs'} \approx 0.18273eV$ (Adamczak et al., 2018), used to re-excite the muons at the $F = 1$ level. These muons then de-excite due to the collisions with the surrounding molecules of hydrogen such that the transition energy is converted into additional kinetic energy of the muonic system. In this way, the muonic atoms are characterized by an excitation energy more or less equal to the 2/3 of the hyperfine transition energy, almost equal to 120 meV (Mocchiutti et al., 2018b).
So it's easy to see that the energy dependence of the muon transfer is a crucial parameter to determine the transition. The oxygen is one the few cases in which the muon transfer rate is not energy independent and for this reason it is added to the hydrogen, making possible to detect the occurred transitions. The time distribution of the K-lines X-ray emitted by the muonic heaver atom μZ is the observable, the rate of which depends on the kinetic energy of μp.

After this explanation, it's quite easy to understand why many articles published by the FAMU group focus primarily on the energy dependence of the muon transfer rate since it is an important parameter that must be precisely determined before conducting the FAMU experiment.

A Monte Carlo simulation has been conducted to study the best parameters and conditions, using the "description of the muon decay, μ^-p scattering from the H_2 molecules, formation of the $pp\mu^- p$ and of the $pd\mu^-$ molecules, muon transfer between proton and deuteron and, of course, of the muon transfer to oxygen. It also includes the energy dependence of the muon transfer rate" (Pizzolotto et al., 2020).

The parameters that the group aim to optimize are the following:

- Gas Temperature;
- Pressure
- Composition of the mixture, like the percentage of the oxygen atoms with respect to the hydrogen;
- The time length of laser shot;
- Time window to consider for the spectroscopic stage.

In this chapter, at first some general information will be given about some parts of the experimental apparatus, regarding:

- Beam and Laser;
- Cryogenic Target System;
- Detector System.

Then, the chapter will continue with the FAMU's experiments history, starting from the first of 2014 and concluding with the latest in the 2021.

3.1 Experimental Apparatus

In this paragraph, the main and newest components of the FAMU experiment are described.

Every different FAMU experiments are performed at the RIKEN RAL facility, with the first experiments conducted in the Port 4. After the recognition of the needed of stable temperature conditions, the experiments were moved to the Port 1, which is also better isolated from the external environment and has more space for the layout. The layout of the Riken Ral facility is shown in Figure 3.1a while in Figure 3.1b the Port 1.

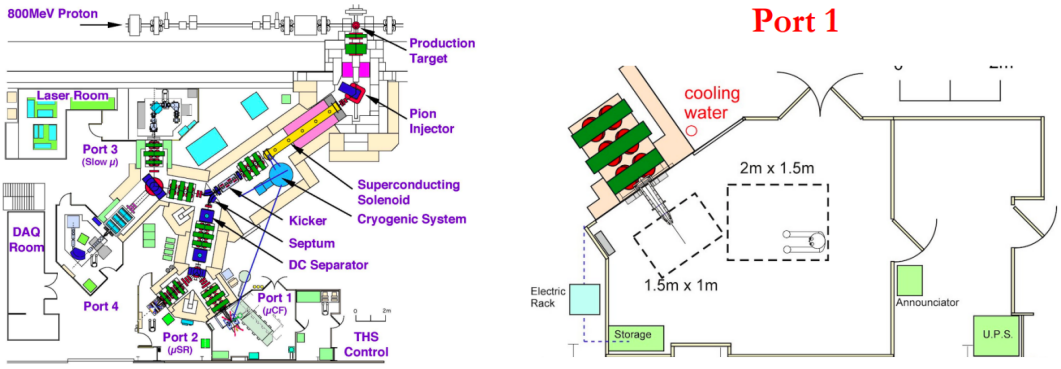

(a) **(b)**

Figure 3.1: RIKEN RAL facility. (a) General representation of the structure in which the experiment is performed. The path starts with the production of the beam and it ends in the Port 1 nowadays (FAMU, 2015a). (b) Scheme of the Port 1, used in the last years (FAMU, 2015a).

In Figure 3.2 is represented the CAD scheme of the FAMU apparatus: the laser system and the cryogenic target system surrounded by the $LaBr_3(Ce)$ detectors, everything positioned on the optical table (Pizzolotto et al., 2020).

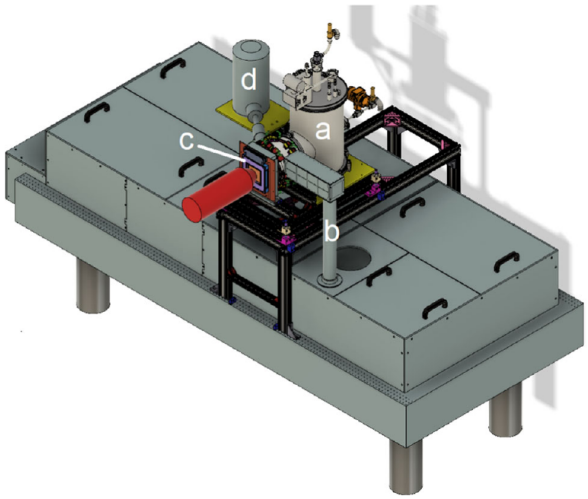

Figure 3.2: Representation of the FAMU system: a) Cryostat, b) Laser optical path, c) Hodoscope, d) Nitrogen container for germanium detector (Pizzolotto et al., 2020).

3.1.1 Beam and Laser

Beam

The pulsed muon beam is suited in such a way that it can deliver about 3 to $8 \cdot 10^4$ muons per second with a repetition rate of $50\,Hz$ and momentum in the range $30 - 80\,Mev/c$ (Adamczak et al., 2018). The beam spill has a double peak structure with a FWHM of about $70ns$ with a peak-to-peak-distance of $320\,ns$. The orientation of the beam, also called beam steering, is tuned using a $1\,mm$ pitch X/Y beam hodoscope. The aim to use a hodoscope is not just to tuned the beam, but also to evaluate the muonic Hydrogen incoming rate while increases the efficiency of the acquired data (Adamczak et al., 2018).

Other components are coupled to the beam hodoscope, each of which with their own function:

- To reduce the quantity of material placed in front of the entrance window, $1\,mm^2$ square scintillating Bicron fibers, coated with EMA, are used. The coating is useful to avoid the light cross-talked. The fibers are placed parallel on two orthogonal plates in the X and Y directions.
- Once the scintillation light is emitted, it is detected by using RGB SiPMs that are larger with respect to the dimensions of the fibers. Due to this size difference, the fibers must be read by turning them to make visible from all the sides.

The initial studied properties of the beam are summarized in Table 3.1 while in Figure 3.3 and 3.4 are shown respectively the pulse structure and the typical muon intensity (FAMU, 2015a).

Parameters	
surface μ^+	$20 \sim 30 Mev/c$
decay μ^+/μ^-	$20 \sim 120 Mev/c$
typical beam size	$10\,cm^2$
FWHM(surface)	5%
FWHM(decay)	10%
Structure	Double Pulse

Table 3.1: Beam characteristics (FAMU, 2015a).

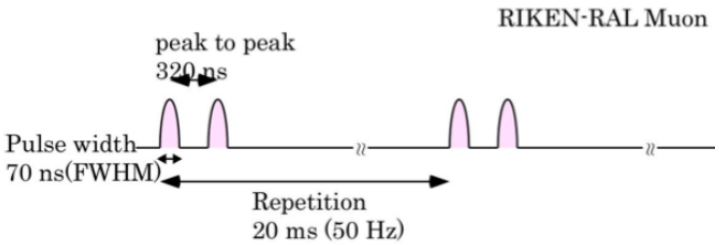

Figure 3.3: Double pulse structure with pulse width of $70ns$, distance between the peaks equal to $320ns$ and repetition of $20ms(= 50Hz)$ (FAMU, 2015a).

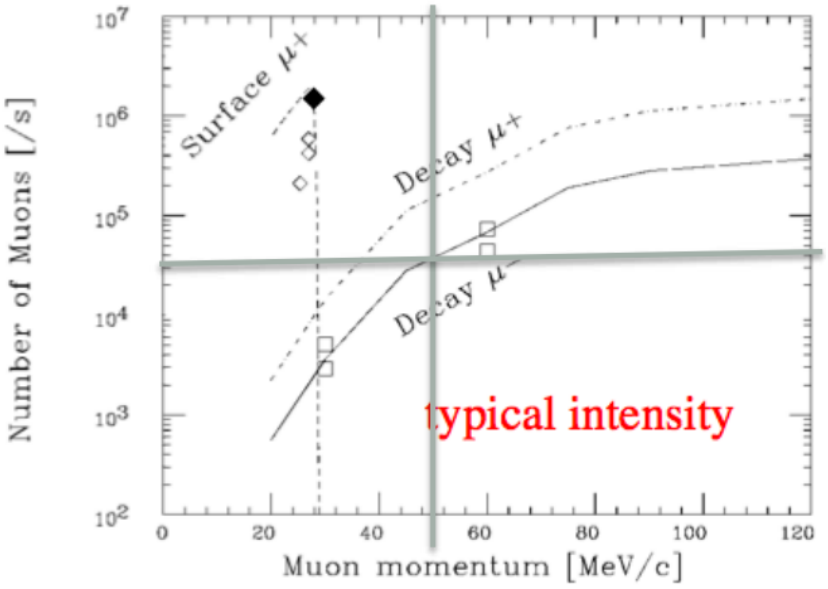

Figure 3.4: Typical muon intensity considering the muon momentum $[MeV/c]$ in function of the number of the muons $[/s]$. The estimated muon intensity shown refers to an area of $4cm \times 4cm$ (FAMU, 2015a).

Laser

To generate a compact, tunable, narrow-band laser, the starting point is to mix two narrow bandwidth solid state lasers: the single longitudinal mode Nd:YAG laser, set to a wavelength of $1.064\,\mu m$, and a tunable Cr:forsterite laser, set to $1.262\,\mu m$. The last laser is injected by a second Nd:YAG synchronized with the first laser. The mixing laser then is transformed in a coherent laser thanks to the DFG, or difference-frequency generation, in non-oxide crystals like lithium thioindate ($LiInS_2$) or lithium selenoindate ($LiInSe_2$) (Pizzolotto et al., 2020).

In Table 3.2 the characteristics of the laser are presented while in the Figure 3.5 the generation of the laser is drawn.

Parameters		
Wavelength Range	$6800 \pm 50\,nm$	$\approx 44\,THz$
Energy output	$> 1\,mJ$	Progressiv. up to $4\,mJ$
Linewidth	$< 0.07\,nm$	$200\,MHz$
Tunability steps	$0.03nm$	$200\,Mhz$
Pulse Duration	$10\,ns$	
Repetition rate	$25\,Hz$	

Table 3.2: Reference values for the pulsed FAMU laser (Pizzolotto et al., 2020).

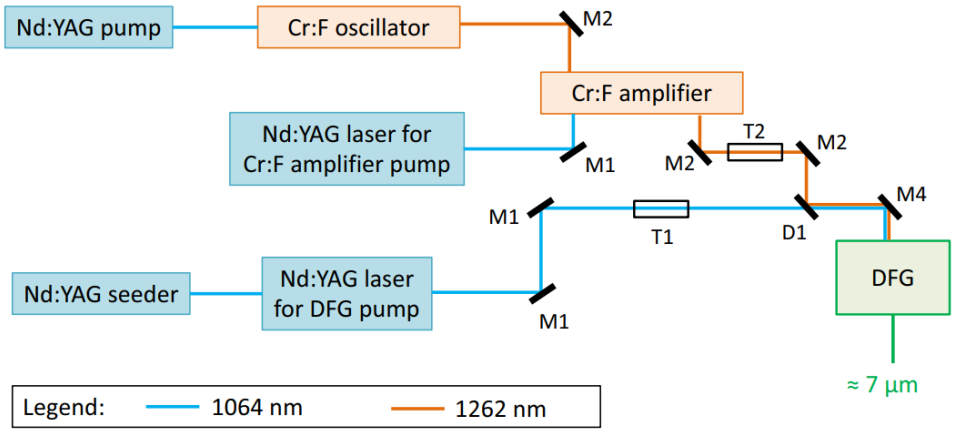

Figure 3.5: Formation path of the FAMU Laser. Two solid state lasers are subjected to several reflections using Mirror (M), Telescope (T) and Dichroic Mirror (D). At the end, the two lasers are transformed into a coherent laser thanks to the DFG (Pizzolotto et al., 2020).

3.1.2 Cryogenic Target System

One of the most important parameters for the FAMU experiment is the collisional energy dependence of the muon transfer rate. It has been already mentioned that it is not constant for gases like the Oxygen and for this reason the gas target is a mixture of Hydrogen and Oxygen. According to this non-constant behaviour, several conditions must be taken into account in order to maximize the results (Pizzolotto et al., 2020)(Adamczak et al., 2018):

- The beam entrance windows should be chosen thin enough to minimize the muon stop and the muon spread due to the Coulomb scattering;
- The transparency to the X-ray lines of the muonic atoms of interest must be improved by using low-Z materials;
- The electrons coming from the decay of muons can cause a very disturbing noise. This problem can be avoid using high-Z materials, capable to improve the nuclear capture rate of the muons outside the gas;
- The system must be able to hold pressure up to 40 atm of ultrapure Hydrogen gas;
- The temperature carries out a central role and the system must be able to work at stable temperatures from 50 up to 300 K;
- A highly reflective optical cavity is required.

According to these requirements the present design of the target system is represented in Figure 3.6 with: Muon beam entrance, Gas Entrance window, Laser entrance and the thermometers.

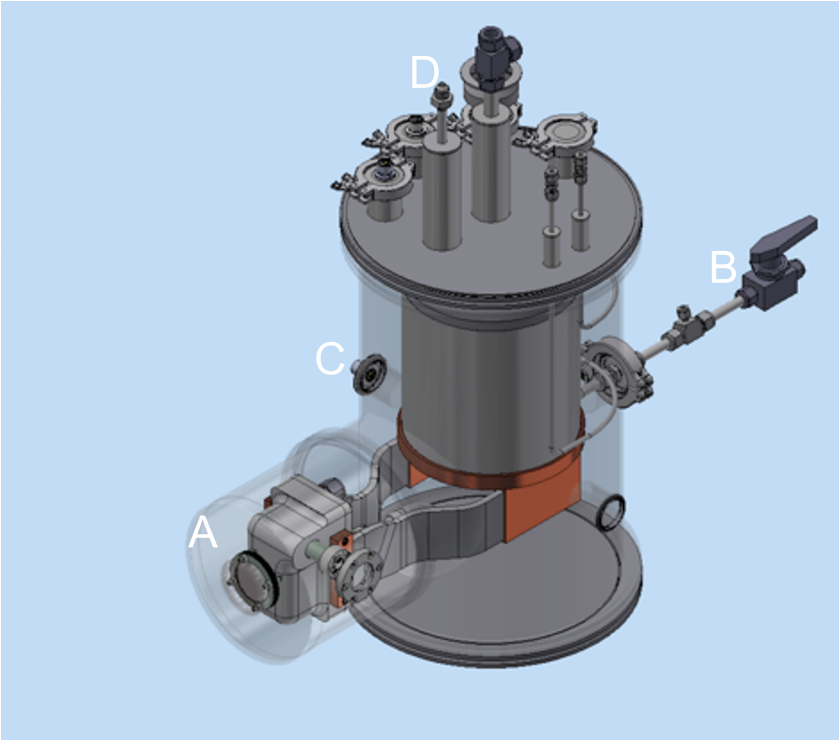

Figure 3.6: Target system: A) Beam entrance window, B) Gas Target Entrance, C) Laser Optical Window, D) Thermometers (Vacchi, 2020).

In Figure 3.7 a scheme of the internal composition of the cilinder is represented.

The surface of the pressurized vessel, contained in the cryogenic vessel, is composed by Gold and Nickel coating. The Gold element has been introduced in the coating in order to reduce the vibrations. In the center, a C-shaped mirror support, accompanied by a lead beam stopper, is used to maintain the top and bottom mirrors useful to control the effective interaction length from which the number of photon round trips depends (Pizzolotto et al., 2020).

The characteristics chosen for the top mirror are cylindrical ends curvature radius of $54\,cm$ and $17\,cm$ while for the bottom the measures are $15\,cm$ and $42\,cm$ (Pizzolotto et al., 2020).

The laser that reaches this mirror system passes through a laser optical window in order to enhance the interaction path between $\mu^- p$ and the photons of the laser, beyond the enhancement of the overall probability of spin-flip transition (Pizzolotto et al., 2020).

For what concern the Muon Beam, it passes through an aluminated mylar window.

From 2018, a cooling system has been constructed around a cold head coupled to a helium compressor in order to take the water necessary for the heat extraction from a closed system. This cooling system works as a single-state cryogenic refrigerator. In the end, the temperature of the system is monitored thanks to four thermometers, two on the cold head and the others at the limit of the inner cylinder (Adamczak et al., 2018).

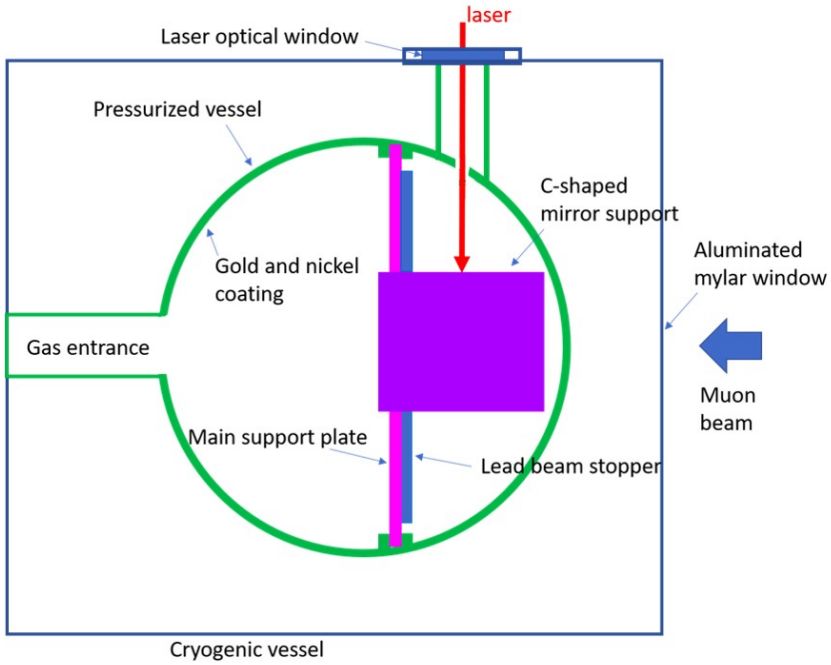

Figure 3.7: Internal structure of the target system (Vacchi, 2020).

3.1.3 Detector System

In order to study the muon transfer rate time dependence and so the proton size it's necessary to have a high speed and high-resolution X-ray detection system.

Several requirements are necessary to study the proton size, some of them observable in Table 3.3.

Requirements	Expected Values
High rate of events	$\sim 3 \times 10^6$ photons/s for each detector
Good spectrometric capabilities	Energy Resolution $< 4\%$ FWHM on $662\,keV$ line of ^{137}Cs
Good time resolution	$< 2\,ns$ FWHM in energy range $[40\,keV\,, 500\,keV]$
High efficiency for photons	absorption efficiency of 85% at $300\,keV$

Table 3.3: Requirements to study the proton size that the detector must satisfied (Baldazzi et al., 2017).

$LaBr_3$:Ce Detector

Thanks to its spectrometric performance (3% FWHM energy resolution at $662\,keV$) and to the good timing resolution ($< 600\,ps$) (Baldazzi et al., 2017) the $LaBr_3$ crystal has been chosen. Seventeen detector systems, shown in Figure 3.8, are positioned around the target system, as closed as possible to it.

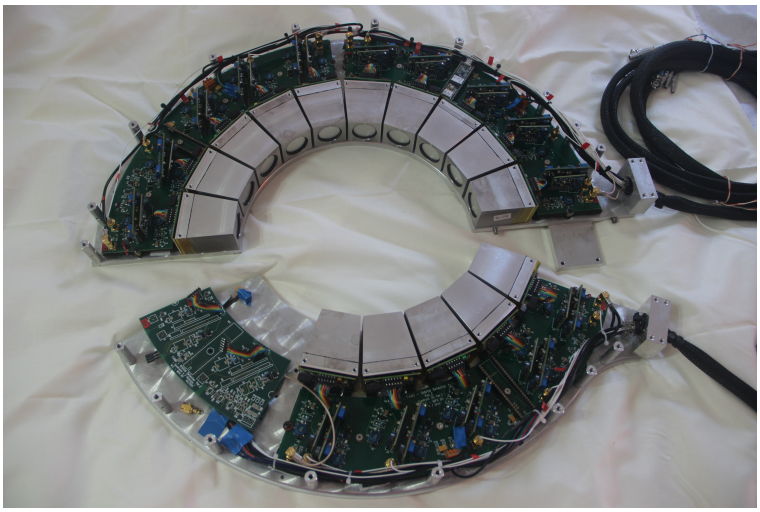

(a)

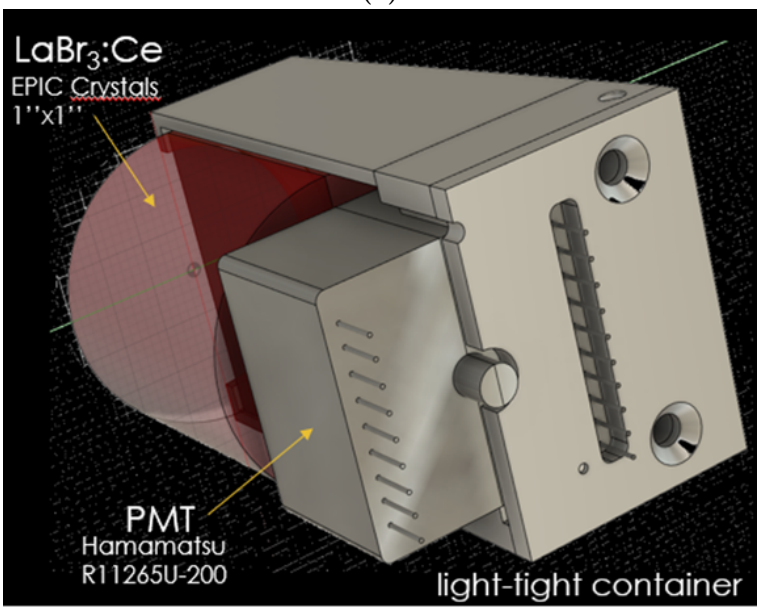

(b)

Figure 3.8: (a) Crown composed by the seventeen detectors and the related electronics. Two of them are missing, due to the an error in the fabrication of the board. (b) Here, just one of the detectors is represented.

The properties of the $LaBr_3$:Ce crystals are subdivided in optical and in mechanical, as can be seen below:

- Optical:
  - Wavelength of maximum emission = $380\,nm$;
  - Wavelength range between $325 - 450\,nm$;
  - Decay times = $25\,ns$;
  - Light Yield = $63\,photons/keV$;
  - Radiation length = $1.881\,cm = 9.95\,g \cdot cm^{-2}$;
  - Transmittance $> 90\%$.

- Mechanical:
  - Density = $5.2\, g \cdot cm^{-3}$;
  - Cubic crystal structure;
  - Lattice constant = $0.6196\, nm$;
  - Melting point = $1116\, ^{\circ}C$;
  - Thermal Expansion Coefficient = $8 \times 10^{-6}\, C^{-1}$.

All the detectors share the same dimensions: $32.4\, mm$ of diameter and $31.5\, mm$ of height. The nominal characteristics differ for each detector and they are shown in Table 3.4.

Detector	Peak Centroid (ch)	FWHM (ch)	Energy Resolution Cs-137 (%)
3	290.33	8.69	2.99
4	261.75	8.05	3.08
5	288.54	9.03	3.13
6	265.09	8.17	3.08
7	284.14	8.02	2.82
8	299.58	8.61	2.87
9	295.55	9.26	3.10
10	260.24	8.32	3.20
11	271.92	7.93	2.92
12	282.01	8.39	2.97
13	313.22	9.24	2.95
14	237.33	6.52	2.75
15	233.79	6.41	2.75
16	239.82	6.05	2.52
17	236.57	6.29	2.66

Presumed Gain			
Detector	relative	Ph/keV	% of NaI
3	1.07	67.3	176.0
4	0.96	60.6	159.0
5	1.06	66.9	175.0
6	0.97	61.4	161.0
7	1.04	65.8	172.0
8	1.10	69.4	182.0
9	1.09	68.5	179.0
10	0.96	60.3	158.0
11	1.00	63.0	165.0
12	1.04	65.3	171.0
13	1.34	84.4	221.1
14	1.02	64.0	167.5
15	1.00	63.0	165.0
16	1.03	64.6	169.3
17	1.01	63.7	167.0

Table 3.4: Nominal characteristics of each detector.

The good performance of high counting rate and energy-time resolutions are directly influenced from the high light output and from the fast time pulse decay. At the same time, the high light output and the high absorption efficiency for X-rays allow for good performances when the detectors are coupled to photomultiplier tubes (PMTs), specialized in high quantum efficiency (Adamczak et al., 2018). The values of these parameters can been seen in Table 3.5.

Parameters	Values
High light output	$63,000\,photons/MeV$ at $380\,nm$
Pulse time decay	$16\,ns$
Absorption efficiency	85% at $300\,keV$
for X-rays	
Spectroscopic performances	$< 3\%$ FWHM
	when coupled to PMT

Table 3.5: $LaBr_3$ Detector characteristics. According to these values, this kind of detectors is the best choice possible nowadays (Baldazzi et al., 2017).

The reference for the full scale chosen is the line of ^{137}Cs at $662\,keV$ since photons' energy lies in the range $40 - 500\,keV$. However, this kind of detector contains some impurities due to the ^{138}La isotope, emitting photons at $789\,keV$ and $1436\,keV$ (Adamczak et al., 2018).

HPGe Detector

Complementary to the $LaBr_3$(Ce), four of these crystals are implanted not in the crown, but a little bit further in order to detect characteristic X-rays. Since they are just a tiny fraction of the overall dimension of the crown, they are specifically used for high-precision inter-calibration. Indeed, the energy resolution of the HPGe is quite better than that of the $LaBr_3$(Ce) crystals (Adamczak et al., 2018). The characteristics of the four HPGe detectors are reported in Table 3.6 (Adamczak et al., 2018), subdivided according to the kind of detector used: two Ortec GEM-S, one Ortec GLP and one Ortec GMX.

Parameters	Ortec GEM-S	Ortec GLP	Ortec GMX
Geometry	Semi-planar	Planar	Coaxial
n/t-type	p-type	n-type	n-type
Dimension	30×20	16×10	54.8×49.8
diameter×length (mm)			
Window (mm)	0.9	0.127	0.127
and type	carbon	beryllium	beryllium

Table 3.6: Characteristics of four HPGe detectors used: Ortec GEM-S, Ortec GLP and Ortec GMX (Baldazzi et al., 2017).

Photomultiplier

The PMTs used are the Ultra Bialkali cathode photomultipliers with a quantum efficiency of $\approx 43\%$ (Adamczak et al., 2018). This high quantum efficiency is necessary to reduce the stochastic term to the energy resolution.

Having a short decay time as the $LaBr_3$ has, the rise front of the pulse at the anode of PMT is short, comprised between 4 and 6 ns (Adamczak et al., 2018).
It's also important to pay attention to the saturation and non-linear response of the PMT for large signals, due majorly to the high light and fast response. In order to prevent from saturation of the signal at the anode, the PMT divider must not work as passive and have to deal with high instantaneous current density in presence of the pulsed muon beam.

Fully Active High Voltage Divider

In order to work with high rate of events keeping the energy resolution high, the High Voltage Divider is needed. The fully active divider has been then introduced since it's been demonstrated that it improves the performance of the wide dynamic range of the PMT (Adamczak et al., 2018).

In order to stabilize the high voltage generator, a negative feedback is used to also drive a MOSFET that works to maintain constant the high voltage by adjusting the current.

A low current, about 30 μA, flows on the gate dividers supplied with a current limited to 2 mA. For high rate applications, it has been used inter-dynode capacitances that provide an excess of current (25 mA) for a small time (0.5 μs).
The non-symmetric distribution of this excess causes spikes on the MOSFETs and so a certain attention must be taken into account (Adamczak et al., 2018).

Before to enter in the Digital Pulse Processor, the signals are pre-formed and the baseline is stabilized.

PCB

The Digital Pulse Processor is used to study the timing and resolution properties of the detector.

The DPP has been designed in order to satisfy some requirements: high sampling rate, real time pulse analysis, flexibility and high communication throughput. To face these conditions, four different components have been introduced composing the Digital Signal Processor, as can be observed in Table 3.7 and in Figure 3.9 (L., 2017).

Requirements	Choices
High Sampling Rate	500 $Msps$ 12bit ADC
Real time pulse analysis	FPGA
Flexibility	Custom Firmware
High communication throughput	USB 3.0 Optical link and microSD

Table 3.7: Requirements and solutions to construct the DPP in order to work with the data coming from the Detector (L., 2017).

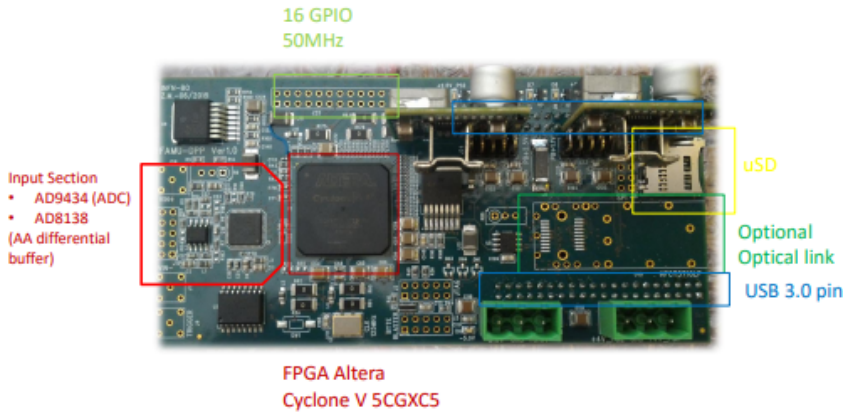

Figure 3.9: Present form of the PCB. The several components on the PCB are: Input Section with the ADC (red), FPGA (dark red), microSD (yellow), Optical Link (dark green), USB 3.0 pin (blue), 16 GPIO 50 MHz pin (L., 2017). The General Purpose Input/Output (GPIO) allows the device to interact with another perifery. It can act as input to read signals from other components or to just control them (L., 2017).

The DPP starts with the ADC feeding the FPGA. The aim of the FPGA is to optimize the energy resolution by triangularly shaping the signal. The triangular form is chosen since it is the best to reduce the pile-up effects and to increase the Signal-to-Noise Ratio, necessary element for the energy resolution optimization. Also the Trapezoidal shape can be considered in case of ballistic decifit, but it has lower performances. The two kinds of shaping are shown in Figure 3.10.

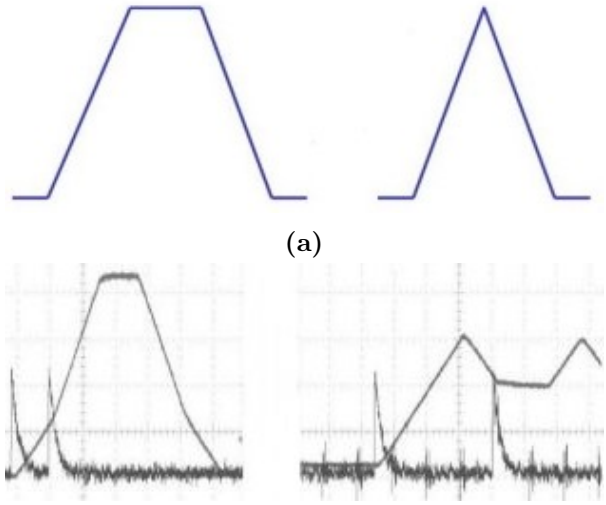

(a)

(b)

Figure 3.10: (a) Theoretical form of the Triangular (right) and Trapezoidal (left) filters. (b) Triangular (right) and Trapezoidal (left) forms taken by an oscilloscope (L., 2017).

These information are then passed to a PC thanks to a USB 3.0 interface (L., 2017), shown in Figure 3.11.

Figure 3.11: Usb 3.0 connection to transfer the data from the circuit to a PC (L., 2017).

The advantages to use a USB 3.0 are the following (L., 2017):

- The astraddle design;
- 5 Gbit/s capable;
- 32 bit interface;
- The embody debugger
- High flexibility.

Due to the use of algorithms present on the FPGA and to the USB, the ADC speed is reduced and in output the circuit has a speed of 100 MHz (up to 32 bit).

Thanks to this construction of the DPP system, when performing a peak detection and/or digitization, the dead time disappears and the finite impulse response causes the reduction of pile-up and pulse overlap effects (Adamczak et al., 2018).

Teensy

In Figure 3.12, the Teensy is shown. A Teensy is a micro-controller development system, coupled to a USB entrance that allows to connect it to the PC (PJRC, n.d.). The software used and uploaded in the Teensy for this purpose has been written in MATLAB. The Teensy have been implemented for two different tasks:

- One Teensy is used to check the Low and High Voltage and to read them in output;
- The others are used to control the commands to send to the circuit in order to vary the values of High Voltage. Each of these Teensy controls a dial of the semicircular crown which means five detectors at the same time.

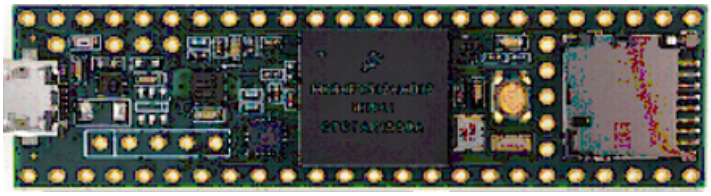

Figure 3.12: Teensy component.

3.1.4 GSPS

In order to acquire the fast signal coming from the $LaBr_3$ detectors, there is the need of a fast continuous sampling digitizer that should be also able to guarantee the required timing and energy resolutions (D'Antone et al., 2018). For this reason, a new digitizer has been constructed with the name of GSPS.

The GSPS is characterized by 1 GS/s sampling rate and a 12-bit nominal accuracy (D'Antone et al., 2018). In addition, the GSPS implements a filter to reduce the presence of the noise, which basically means that the GSPS contains a stage to optimize the Signal-to-Noise Ratio (SNR). The GSPS acquires from 4 ADCs, containing 2 channels that acquire the same signal. Each ADC works for a detector and so one GSPS system is able to work with at maximum 4 detectors.

To work under the several requirements of the circuit and detectors, the GSPS digitizer has been coupled with two Analog Devices (D'Antone et al., 2018), as shown in Figure 3.13.

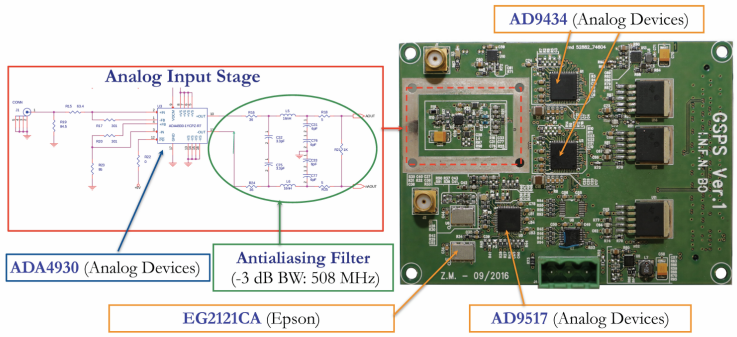

Figure 3.13: On the left the Analog input stage is schematized, comprising also the Antialising Filter (D'Antone et al., 2018). On the right, a picture of the GSPS digitizer is shown (D'Antone et al., 2018).

For the purpose of this thesis, the GSPS used, shown in Figure 3.14, it's not already complete since the Linux Firmware is not implemented yet and there is just one board for the channels, so it's possible to analyze just one detector at the time.

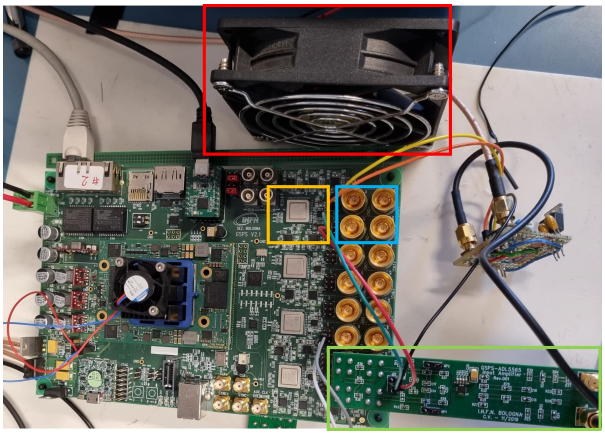

Figure 3.14: GSPS Circuit. The following elements have been highlighted: one ADC (yellow square), two channels corresponding to the ADC (blu square), the board interfacing with the detector (green square) and a fan (red square) preventing the channels to overheat.

3.2 Experiments

In this Section the different FAMU experiment results will be treated. The apparatus of each experiment will be treated only if it changes from the previous one while from 2020 the experimental apparatus is more or less the same to the newest of which has been already talked.

3.2.1 2014

"The FAMU experiment: muonic atoms to probe the proton structure"

In (Guffanti, collaboration, et al., 2016) article the problem related to the proton radius discovered in 2010 has been introduced for the first time.
Also, this is the first article in which the FAMU experiment is presented. It already talks about the needing of an experimental apparatus able to detect the high-rate X-rays. The scheme of the theoretical path to detect the X-rays is observable in Figure 3.15 (Guffanti, collaboration, et al., 2016).

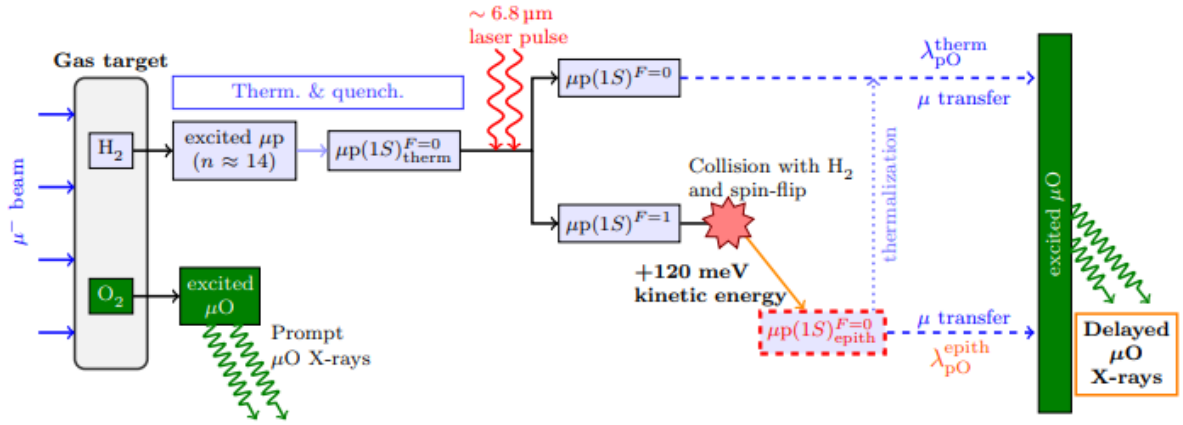

Figure 3.15: General scheme of the first FAMU Experiment. The muons slow down and stop in a hydrogen gas target, generating the so-called muonic hydrogen atoms. Several collisions between the muonic atoms and the hydrogen molecules de-excite the muonic atoms, leaving just the thermalized atoms in the $1S^{F=0}$ state. Using a laser tuned on the Hyperfine Structure resonance, several single-to-triplet transitions are caused, but the triplet-state atoms are de-excite again to the singlet one, trasforming the transition energy into additional kinetic energy. Thanks to the contamination with O (also Ar, or Ne), it's possible to study the muon transfer rate from muonic Hydrogen to high-Z materials. (Guffanti, collaboration, et al., 2016).

In a preliminary test, four targets have been taken in consideration: three gas mixtures containing pure H_2, $H_2 + 2\%Ar$, and $H_2 + 4\%C0_2$ and a graphite block. Recent studies have been demonstrated that the Oxygen was one of the elements for which the muon transfer rate was energy dependence, but also other elements were have been consider, like Argon and Neon. For this reason, they have been added to low-Z materials (Guffanti, collaboration, et al., 2016).

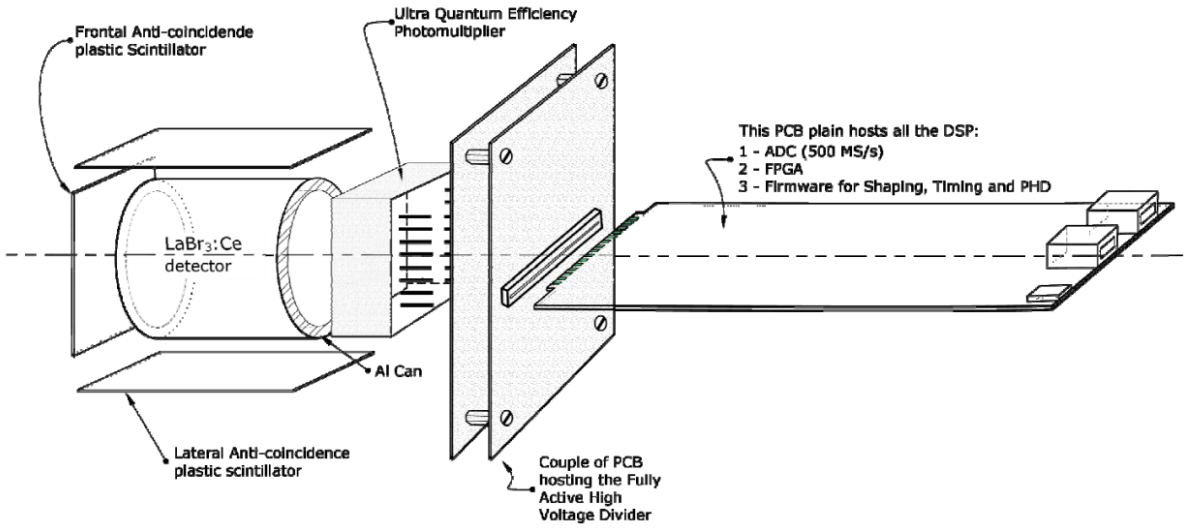

Figure 3.16: Detection system composed by two Anti-coincidence scintillators, the detector crystal $LaBr_3$:Ce, the two PCBs (Adamczak et al., 2018).

The detection system is shown in Figure 3.16 with a lower number of detectors compared to those used in last experiments: 5 based on the $LaBr_3$(Ce) crystals and just two HGPe detectors. In Figure 3.16 can be observed the form of one $LaBr_3$(Ce) detector and all the components attached to it, listed below.

- Frontal and Lateral Anti-coincidence plastic Scintillator, nowadays removed thank to the Gold usage around the detector;
- Three different detector crystals: 1" (diameter)×1" (thickness) $LaBr_3$:Ce, more compact $LaBr_3$:Ce coupled to a SiPM and HPGe;
- Aluminium Can of $3 \times 3\,cm$ containing the crystal;
- Ultra-Quantum Efficiency Photomultiplier;
- Couple of Printed Circuit Board (PCB) containing the Fully Active Voltage Divider;
- Another PCB containing the Digital Signal Processor components : ADC, FPGA, Firmware for Shaping, Tiping and PHD.

The detector output was also recorded for a very short time, just $5\,\mu s$ after the trigger while the waveforms shaping and processing was performed off-line with a dedicated algorithm (Guffanti, collaboration, et al., 2016).

The example graphs obtained studying single- and multi-pulse events from one $LaBr_3$ detector is shown in Figure 3.17 while Figure 3.18 shows the time evolution of the X-ray spectrum using a $H_2 - CO_2$ target.

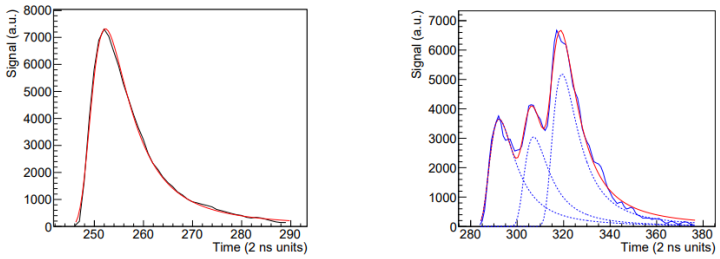

Figure 3.17: Graphs obtained from the use of just one $LaBr_3$ detector. On the left, the result comes from single-pulse events while on the right multi-pulse events have been considered (Guffanti, collaboration, et al., 2016).

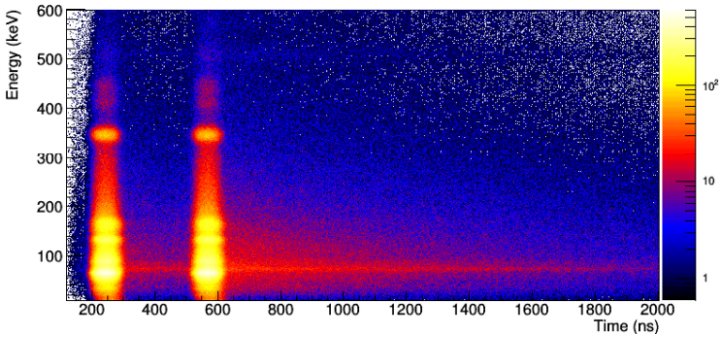

Figure 3.18: Time evolution of X-rays using a $H_2 - CO_2$ target where is evident the double pulse structure of the beam (Guffanti, collaboration, et al., 2016).

The spectrum and the time-distribution obtained instead using all the four $LaBr_3$ detectors and the HPGe detector change with respect to the single case, as can been observed in Figure 3.19a and 3.19b.

As can be observed from the Figure 3.19b, two are the major contributions: the "prompt" peak and the "tails" from the delayed events. From these it's possible to see that the prompt peaks carry majorly the information about the characteristics X-ray while the information about the muons is predominantly contained in the tails (Guffanti, collaboration, et al., 2016).

The information about the lifetimes of the different muonic atoms is shown in Table 3.8, compared also to the reference values.

Muonic Atoms	2014 Values (ns)	Reference Values (ns)
μC	2011 ± 16	2026 ± 1.5
μp	2141 ± 98	2194.53 ± 0.11
μAl	879 ± 28	864 ± 2
μO	1824 ± 46	1795 ± 2
μAr	564 ± 14	537 ± 32

Table 3.8: The lifetimes of the various muonic atoms determined in the 2014 experiment (Guffanti, collaboration, et al., 2016), compared to the reference values that can be found in the article (Suzuki, Measday, and Roalsvig, 1987).

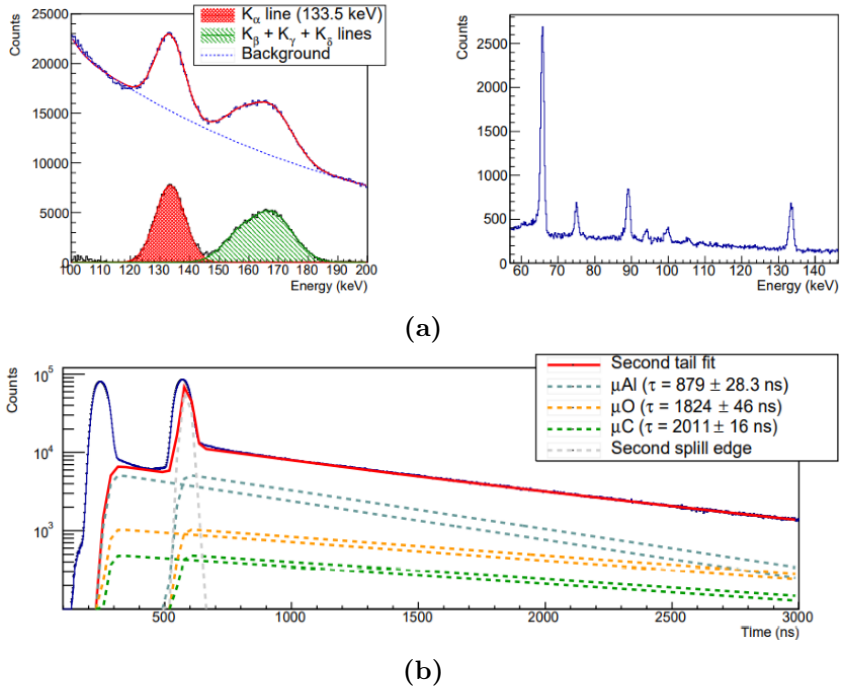

Figure 3.19: (a) In the two figures are represented, respectively, the X-rays spectrum coming from the four $LaBr_3$(Ce) detectors and the spectrum coming from the HPGe detector. In the left image, the red curve is associated to the K_α lines, the green curve to the summed effects from the K_β, K_γ and K_δ while the blue curve represents the background signal. (b) In the bottom image, the time distribution of the events is represented, events acquired from the $H_2 - CO_2$ target and using all the four $LaBr_3$ detectors. The two main contributions are the prompt peak and the tails of the delayed events (Guffanti, collaboration, et al., 2016).

The objective for this first experiment was the definition of a detection system with which was possible to study the behaviour and characteristics of muonic atoms and X-rays, with particular attention to the X-rays generated from the Oxygen. In the end, the good performance of the $LaBr_3$ crystals makes them one of the first choice in successive FAMU experiments.

3.2.2 2018

"The FAMU experiment at RIKEN-RAL to study the muon transfer rate from hydrogen to other gases"

Target System

The target system used in this article was quite similar to the last used in 2020, but with different shape. The Figure 3.20 represents its form, showing the different parts.

An Aluminium cryostat, thank to means of vacuum jacket, isolates the target (gas) from the environment. Moving from right to left, the muons enter in the first $0.8\,mm$ of Aluminium entrance window reaching the evacuated volume, where three disks of $0.1\,mm$ of Aluminium work as radiative shields (Adamczak et al., 2018).

Then a second Aluminium entrance window with length of 2.8 mm injects the muons in the pressurized volume. Due to the presence of the X-rays coming from the target, it has been necessary to introduce a thin coating of high-Z materials, composed by 100 μm of Ni and 20 μm of Au. Then, due to the sensibility of the optical path to the vibrations, the cooling system has been introduced. This cooling system is a compartment composed by liquid nitrogen.

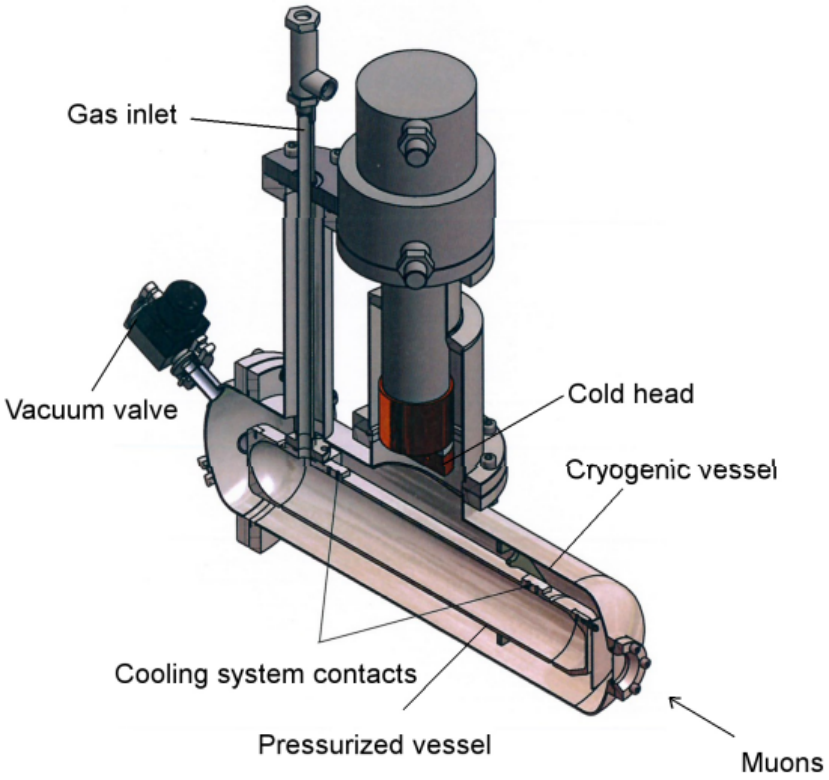

Figure 3.20: Target system comprising the pressurized and cryogenic vessels, the cooling system and the vacuum valve (Adamczak et al., 2018).

Beam Momentum Tuning and Detectors Positioning

First, the position of the X-rays detectors depends on the distribution of the muon stops. This dependence is related to the consideration that the X-rays coming from the inert material must be minimized while the rays coming from the gaseous target must be maximized. Also, the minimization and maximization of the rays influence the muon stop, according to the amount and type of the materials inserted along the beam line and according to the momentum and spatial spread of the beam (Adamczak et al., 2018).

Using a simulator called GEANT4 and by varying the beam momentum several information about the muon stop have been obtained, according the different considered materials, as can be shown in Figure 3.21.

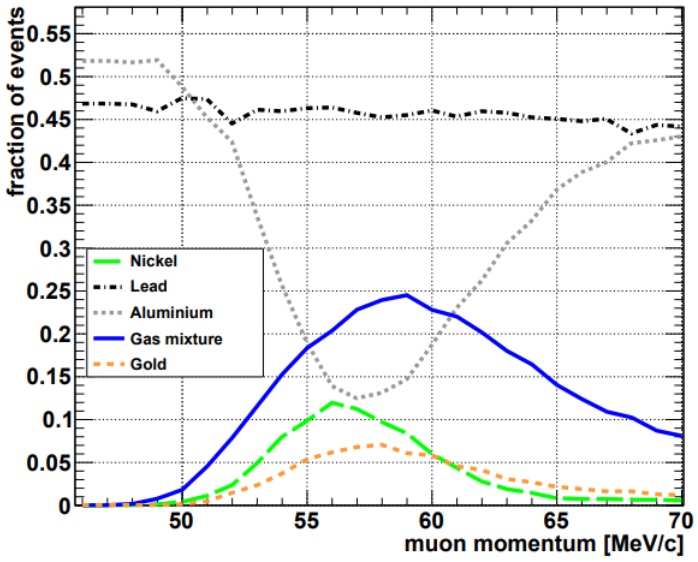

Figure 3.21: Simulation of the muon stopping in the FAMU apparatus using the GEANT4 simulator. The lines represents the fraction of events stopping as a function of the beam momentum in different part of the apparatus that are also made by different materials: gas mixture (blue continuous line), Aluminium walls (gray dashed line), coating composed by Nickel (green continuous line) and Gold (yellow dashed line) (Adamczak et al., 2018).

Looking at this picture, the lines of Gas Mixture (blue) and Aluminum (gray) almost correspond at the value of $57\,MeV/c$ of the beam momentum where the correspondence is between the maximum muon stop of the first and the minimum muon stop of the second.
For heavier materials, Gold and Nickel, the muon stop doesn't need to be considered since the X-rays emission coincide with the muons arrival time.

Once the muon beam momentum has been chosen, the spatial distribution of the muon stop can be studied, as can be observed in Figure 3.22.

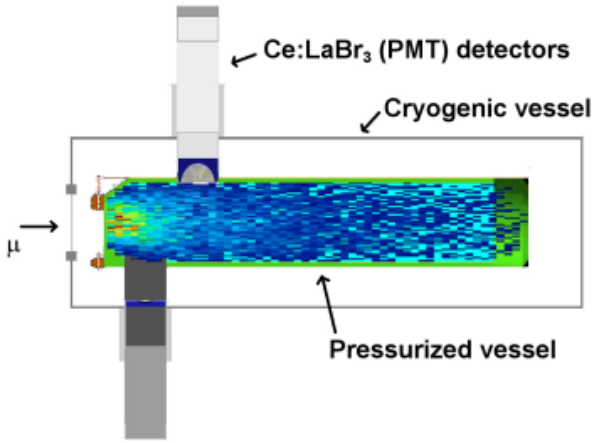

Figure 3.22: Spatial Distribution of the muons extrapolated from a GEANT4 simulation and superimposed on an image of the detection system. The majority of the muons stops in the first centimeters of the detector (Adamczak et al., 2018).

Observing it, the green part of the spectrum indicates that the majority of the muons doesn't go beyond few centimeters of the target and this is the reason because the detectors must be placed very closed to the target material. From 2017 the detectors were arranged in two half circular crown supports, containing all the necessary electronics (Adamczak et al., 2018).

The HPGe detectors, instead, are not positioned so closed to the target due to their sensitivity to the X-rays pile-up.

Data processing

In order to process the data, a software written in $C++$ has been written, using also ROOT toolkit. Two are the main operating modes: one very fast, requiring small CPU power, is used to monitor the data flow during the acquisition and to produce the quality plots; the other is used to obtain more accurate results from the analysis but it is much more slower than the first (Adamczak et al., 2018).

The data processing depends strongly on the waveform shape and also from the characteristics of each singular detector.
Here the Hodoscopes fulfill their function of studying the shape and intensity of the muon beam, with two different modes: "quick-look" and "full analysis" (Adamczak et al., 2018).
For all the detectors and the processing modes the program flow is almost the same.

At first, the waveforms are unpacked event by event. Then a numerical derivative of the waveform is computed, followed by a smoothing of the sharp edge due to the saturation problem (Adamczak et al., 2018). An example of both cases are shown in Figure 3.23.

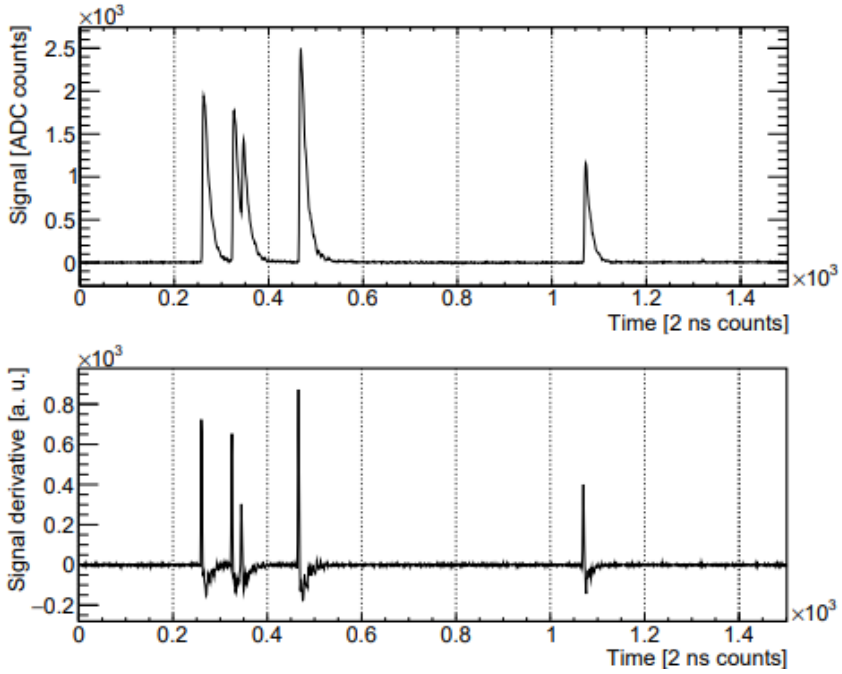

Figure 3.23: Representation of the first two steps of the data processing. Both the graphs are in function of the time where one count corresponds to $2ns$. In the top panel, the unpacked waveforms are shown, while the bottom one contains the computed signal derivative (Adamczak et al., 2018).

For each of the signals, the saturation events are saved in the final output file. At this point, the energy of each X-rays has been reconstructed together with its arrival time and an output data is saved, containing the amplitude of the different signals, the number of detectors and other information.
In the end, the output data is saved in a ROOT file (Adamczak et al., 2018).

According to the operating mode, the outputs from the $LaBr_3(Ce)$ detectors are reconstructed with two different algorithms. One uses the faster processing method ("quik-look") to stabilize the difference between baseline and waveforms maximum. Using instead the slower processing method ("full analysis"), each signal is fitted with a function of signal shape (Adamczak et al., 2018).

For the reduction of the pile-up effect, a tuning of the input parameters is necessary, accompanied with an excellent stability of detector waveforms.
In the delayed phase, the MonteCarlo Simulation proved that the perfect pile-up (indistinguishability of two overlapping signals) is completely negligible, since it starts with a separation less than $15ns$ between signals (Adamczak et al., 2018).
An example of this reconstruction can be seen in Figure 3.24.

On the other hand, the HPGe detectors are too slow to detect many X-rays during the same trigger. The two different modes in this case scan the waveform saving its maximum signal amplitude and time, considering just one X-rays per trigger.
In the end so a calibration offline of the detectors is necessary, such that the units are converted into keV (Adamczak et al., 2018).

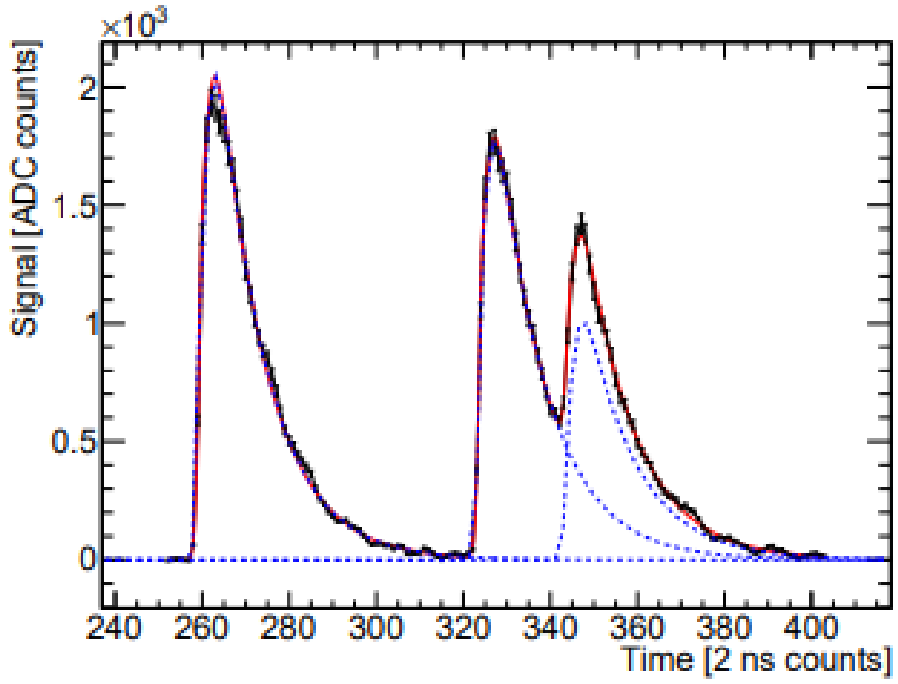

Figure 3.24: Fitting (red line) obtained from the overlapping signals (blue dashed lines) of three different waveforms (black points) (Adamczak et al., 2018).

Characterization

In order to characterized the Beam, the use of Hodoscopes was necessary. Indeed, thanks to its role of optimization and control of beam orientation, the number of beam muons has been obtained by using the total charge collected, observable in Figure 3.25. Once obtained, the group found the values to be consistent with the previous results (Adamczak et al., 2018).

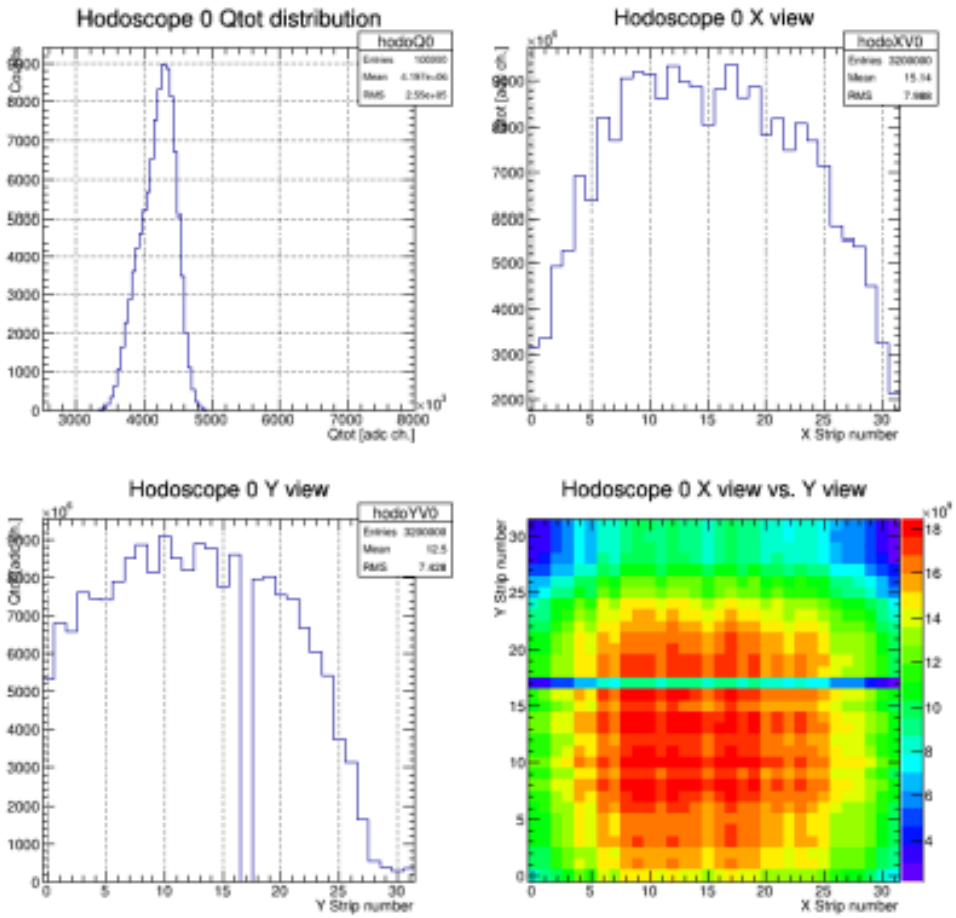

Figure 3.25: Number of muons obtained using the hodoscopes and the total charge collected information. In the top left image, the total charge distribution is represented. In the top right and left bottom images the information obtained from the X and Y views are respectively represented. In the last image instead, the total accumulated charge is represented. One line is in evident contrast with the others, due to the fact that one cable of the apparatus was disconnected (Adamczak et al., 2018).

Detection of Characteristic X-rays

Here, the results for each type of Detector are presented.
At first, consider the results for the $LaBr_3$ using a PMT readout, in Figure 3.26. The acquisition time has been considered to be around 10 μs while the entire windows has been separated in pre-trigger, prompt phase and delayed region. The last region is the most interesting since almost the majority of the muonic X-rays are produced

here (Adamczak et al., 2018). The three region can be observed in Figure 3.26a. In Figure 3.26b the delayed spectrum of gaseous hydrogen with a contamination of oxygen is shown, reporting also the difference in presence and in absence of background.

Focusing just on the $K\alpha$ line, the value measure for the X-rays detection is about 133 keV with an energy resolution of 8.5%, value that fits perfectly with the reference one and its uncertainty. This demonstrate the good performance of the $LaBr_3$ detectors, especially the good spectral and timing performances (Adamczak et al., 2018).

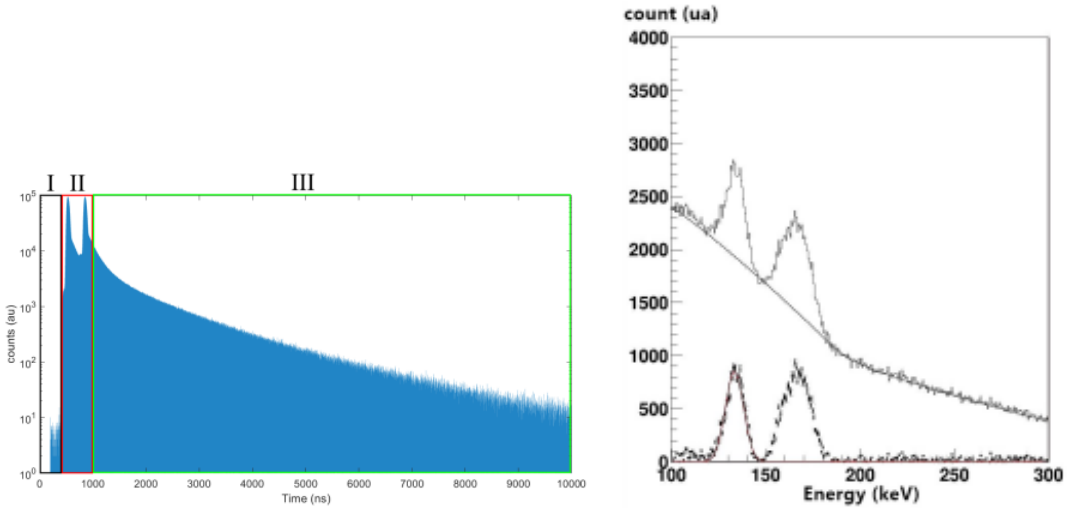

(a) **(b)**

Figure 3.26: (a) Time spectra using the $LaBr_3$(Ce) crystals using the PMT readout. The three different regions considered are: pre-trigger (black), prompt phase (red) and delayed region (green). (b) Delayed spectrum of the a mixture gas composed by H2 and a small fraction of O_2. In the upper spectrum, the background is present while in the bottom it is not. The energy resolution for a $K\alpha$ line of 133 keV is about 8.5% (Adamczak et al., 2018).

Several problems occur in the study of the detection using the $LaBr_3$ detectors with SiPM array readout.
First of all, the target wasn't composed just by Hydrogen and Oxygen bust also a strongly contamination of Nitrogen is present. In addition, the *in situ* experiment was characterized by environmental interference, like the electronic noise or the temperature excursions. These problems caused the values to be worse from those obtained in laboratory (Adamczak et al., 2018).
The spectrum of pure Hydrogen with contaminations can be observed in Figure 3.27.

Although all the problems faced, the results demonstrate that the coupling between the crystal and the SiPM could be useful in regions of difficult access of the detector. Also, to not be forgotten is the fact that the corrections for the temperature gain drift have improved the energy resolutions up to 4% level (Adamczak et al., 2018).

For the last case, the HPGe detectors shown a particularly ability in the intercalibration of the entire apparatus, observable in Figure 3.28 where a spectrum

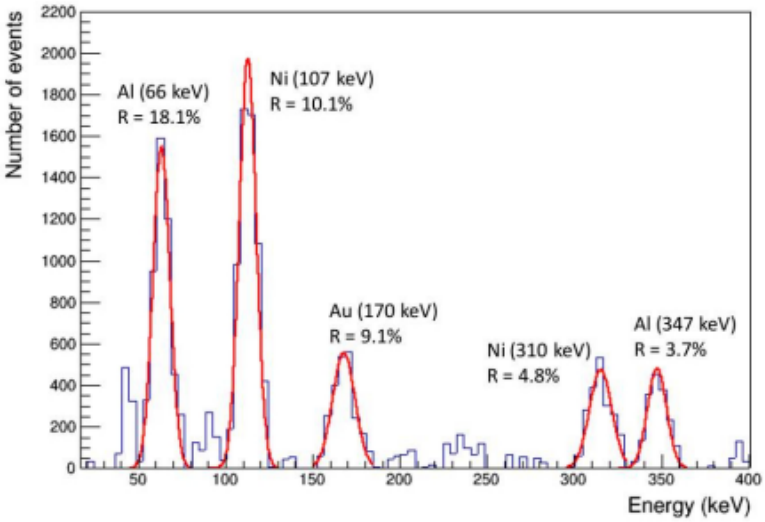

Figure 3.27: Spectra of $LaBr_3(Ce)$ crystals coupled to SiPM array readout. The peaks are related to heavy materials: Au, Ni and Al (Adamczak et al., 2018).

of the mixture Hydrogen and Oxygen is depicted.

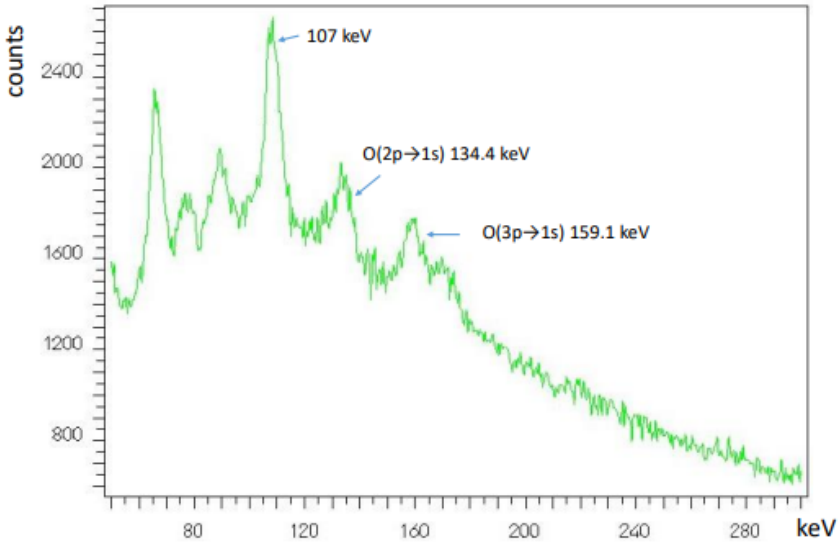

Figure 3.28: Energy Spectrum using the HPGe detectors coupled to a fast amplifier, an ORTEC 579. The range considered is between 50 and 300 keV. The characteristics X-rays are visible and just as example three peak energies of the Oxygen are shown (Adamczak et al., 2018).

At the same time, observing the time structure of the beam pulses using a GLP HPGe detector (Figure 3.29a) and the time evolution of the K_α line energy distribution (Figure 3.29b), it's possible to say that this detector presents a good energy resolution of about 2% in the region of interest with a good time resolution and possibility to resolve some pile-up events (Adamczak et al., 2018).

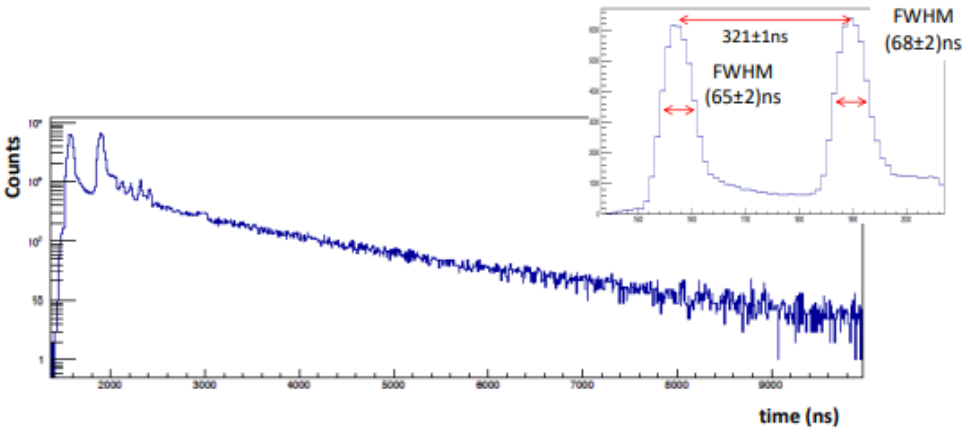

(a)

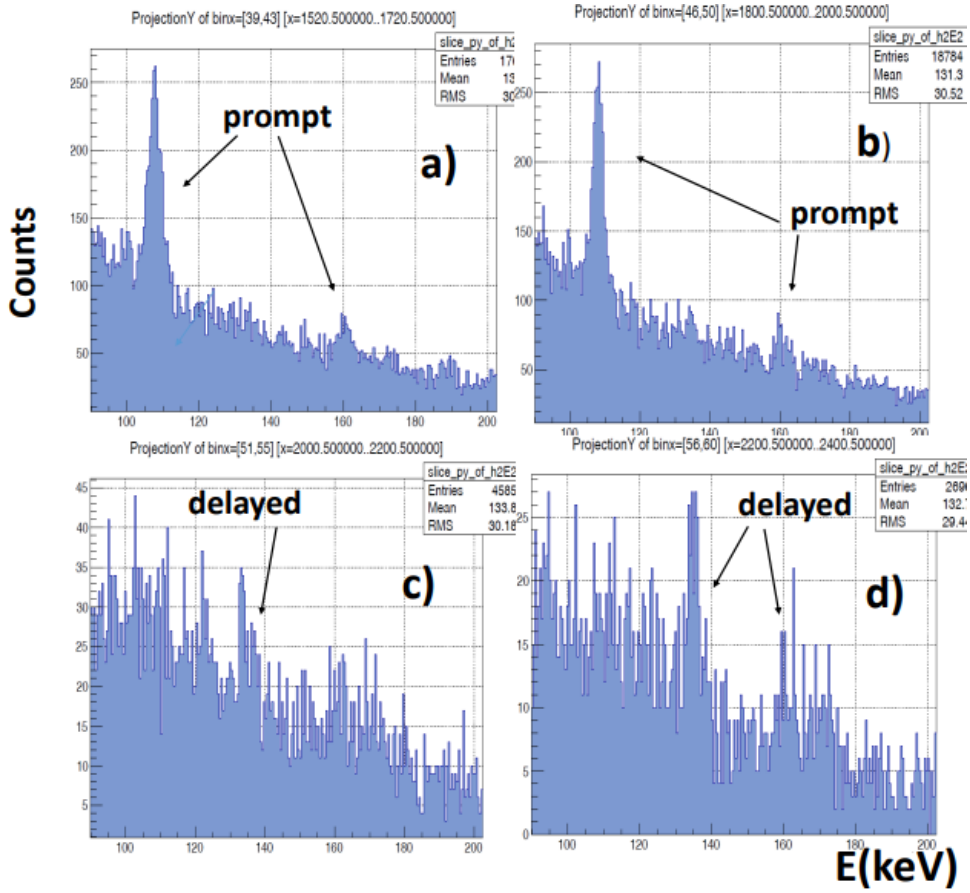

(b)

Figure 3.29: (a) Reconstructed time evolution from the HPGe detector with shown peak-to-peak distance of $321 \pm 1\,ns$ and FWHM of two peaks corresponding to $65 \pm 2\,ns$ and $68 \pm 2\,ns$. (b) Time evolution of the K_α lines transition from $2p$ to $1s$ using always the HPGe detector. In the upper reconstructions are shown some prompt peaks while in the bottom are shown the delayed (Adamczak et al., 2018).

"FAMU: study of the energy dependent transfer rate $\Lambda_{\mu p \to \mu O}$"

In addition to the muon transfer rate, also the energy transfer rate is one of the most important parameters to determine in order to characterize the detector system and

to be able to establish the proton radius with a higher accuracy.

The (Mocchiutti et al., 2018a) article focused its attention to this dependence, detecting so the transitions that occurred in the muonic atoms. The data considered to study this transfer were taken of 2016.

As already explained before, the energy dependence must be exploited according to some heavy atoms, like Oxygen, for which this dependence exists.

The experimental apparatus is shown in Figure 3.30, where eight detectors of $LaBr_3(Ce)$ are arranged in a star-shape structure around the target, in front of which is positioned the hodoscope. Two detectors of HPGE are inserted further away, due to their sensitivity to the pile-up effects.

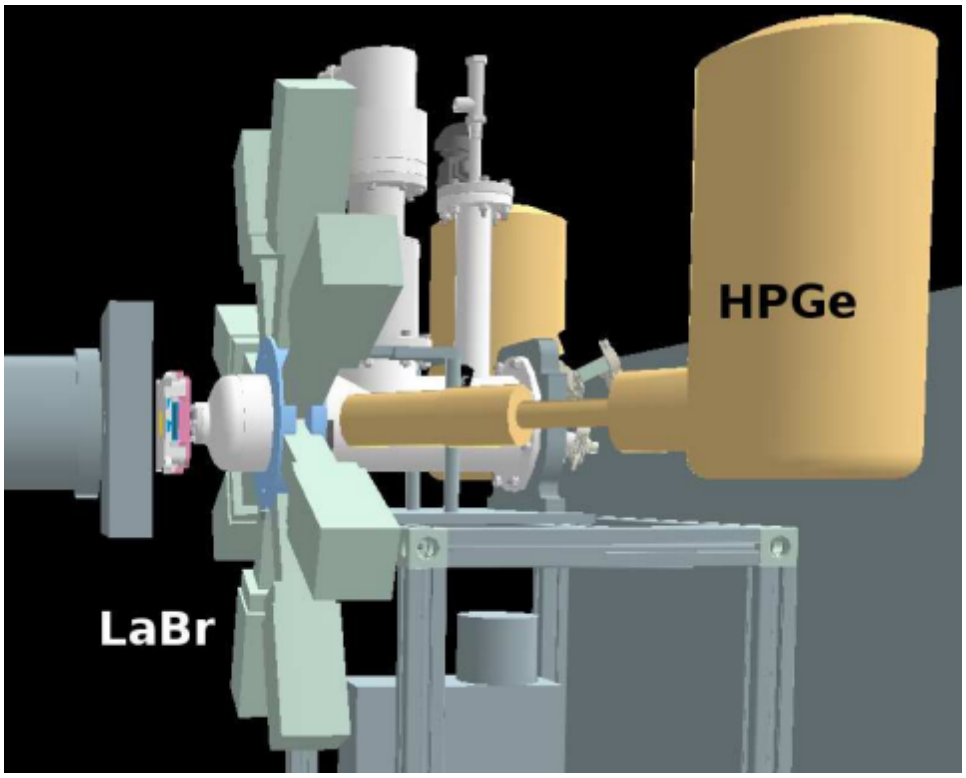

Figure 3.30: Eight detectors arranged in star-shaped structure, positioned closed to the target system. The HPGe detector instead is attached further away (Mocchiutti et al., 2018a).

To study the kinetic energy transfer rate, the experiment must be performed in thermalized conditions such that the energy of interest follows the Maxwell-Boltzmann distribution (Mocchiutti et al., 2018a).
The quantity of Oxygen gas considered was about 3% in order to have a longer mean transfer time with respect to the time required for the data acquisition of about $150\,ns$. In this range of time, the system is fully thermalized after the arrival of the last muon (Mocchiutti et al., 2018a).

The equation describing the variation of the number of muonic hydrogen atoms $N_{\mu p}$ in the time interval is (Mocchiutti et al., 2018a):

$$dN_{\mu p}(t) = S(t)dt - N_{\mu p}(t)\lambda_{dis}dt \tag{3.1}$$

and the total disappearance rate λ_{dis}:

$$\lambda_{dis} = \lambda_0 + \phi(c_p\Lambda_{pp\mu} + c_p\Lambda_{pd} + c_0\Lambda_{p0}) \tag{3.2}$$

where:

- S(t) = number of muonic hydrogen generated in the time interval;
- λ_{dis} = total disappearance rate;
- λ_0 = disappearance rate of the muons bounded to hydrogen;
- $\Lambda_{pp\mu}$ = formation rate of $pp\mu$ ion in collision with hydrogen;
- Λ_{pd} = muon transfer rate from the μp to the deuterium;
- Λ_{p0} = muon transfer rate from the μp to the oxygen.

The different values of the parameters necessary to set up the detection system are described in Table 3.9.

Parameters	Values
$T\,(K)$	300
$P\,(bar)$	41.00 ± 0.25
O_2 concentration (%)	(0.30 ± 0.09)
N_0 $(atom/cm^3)$	$4.25 \times 10^2 2$
# densities LHD atomic units	$(4.869 \pm 0.003) \times 10^{-2}$
Atomic concentration Oxygen	$(1.9 \pm 0.3) \times 10^{-4}$
Deuteron concentration	$564 \pm (1.358 \pm 0.001) \times 10^{-4}$
$\Lambda_{pp\mu}\, s^{-1}$	2.01×10^6
$\Lambda_{pd}(T)\, s^{-1}$	1.64×10^{10}
$\lambda_0\, s^{-1}$	$(4665.01 \pm 0.14) \times 10^2$

Table 3.9: Values of the parameters used in Equations 3.1 and 3.2 (Mocchiutti et al., 2018a).

The data analysis is based on the extraction of the transfer rate in function of the kinetic energy of the muonic atom. The path to follow starts with the calibration of the $LaBr_3$(Ce) detectors, followed then by the integration of all the signals (Mocchiutti et al., 2018a).
After this first step, the good events have been recorded from the data of 2016 and the selection efficiencies were evaluated. The delayed events are then used to obtain the energy spectrum in range of temperatures from 50 up to 500 keV for $K_\alpha(133\,keV)$, $K_\beta(158\,keV)$ and $K_\gamma(167\,keV)$ where the transfer rate from hydrogen to Oxygen is evaluated. In order to obtain this value, the temperature must be recorded due to the dependence from it (Mocchiutti et al., 2018a).
For each spectrum, the estimation and subtraction of the background has been performed. Just in the end the mean kinetic energy of μp can be obtained.

Detector Calibration

As for the (Adamczak et al., 2018) experiment, a coupling between C++ and ROOT software has been used.

An ADC has been used in order to detect the X-rays signals. Here the Prompt and Delayed X-rays lines were used to correct the fluctuations related to the temperature. The spectrum obtained using the ADC then has been converted into energy thanks to the comparison with the detected peaks (Mocchiutti et al., 2018a). The spectrum of the calibrated eight detectors can be observed in Figure 3.31.

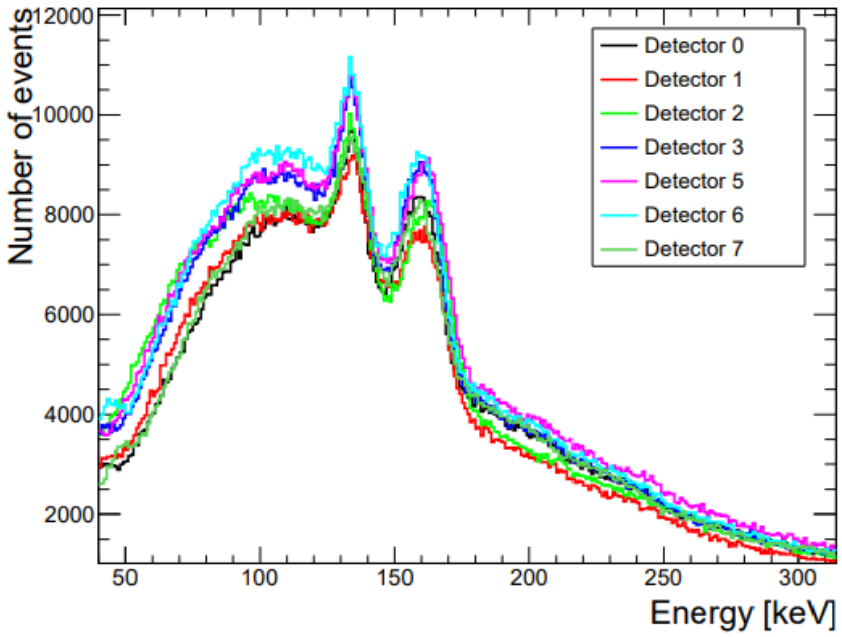

Figure 3.31: Energy spectrum of each $LaBr_3(Ce)$ for delayed events (Mocchiutti et al., 2018a).

Data Selection

The data analysis aims to study the time evolution of the X-rays signals coming from the oxygen in the trigger time windows, corresponding more or less to an acquisition of 10 ns. In this analysis, the prompt emission is the time occurring from 0 up to 1200 ns, at the end of which starts the delayed phase (Mocchiutti et al., 2018a).

The waveform is recorded every $2ns$ and read then by the software to extrapolate the information about the single pulse, recognized thank to a threshold superimposed on the derivative of the waveform. The simulation performed on this part of the experiment shows that the software was able to detect X-rays with energy higher than $20\,keV$ and separation higher than $15\,ns$ with a 99.9% efficiency or even higher (Mocchiutti et al., 2018a).

On Figure 3.32a it is possible to observe the time distribution of X-rays, where the peaks correspond to the muon arrival time with 72 ns of FWHM and 320 ns of separation. On Figure 3.32b, instead, the percentage of the signal pulses is shown. In the prompt emission, it's possible to observe the presence of the pile-up effects, presence that is very reduced in the delayed phase.

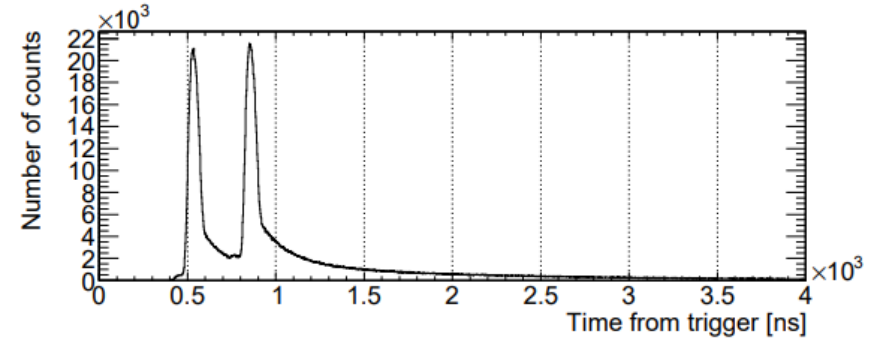

(a)

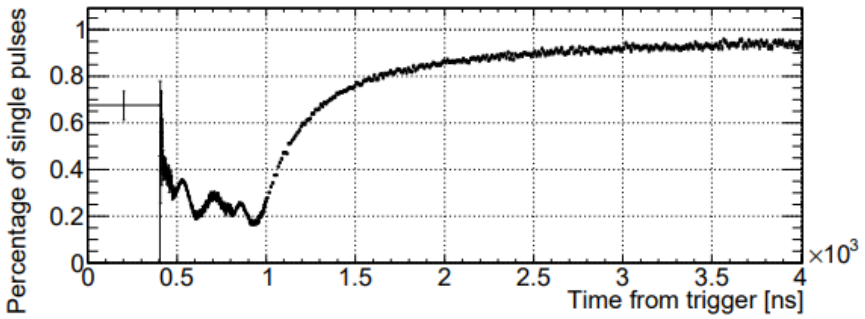

(b)

Figure 3.32: (a) Representation of time evolution of X-rays. The peaks correspond to the muon arrival time with 72 ns of FWHM and peak-to-peak distance of 320 ns (Mocchiutti et al., 2018a). (b) Percentage of the single pulses as function of the time. In the prompt phase it's evident the presence of the pile-up effects, remarkably reduced in the delayed phase (Mocchiutti et al., 2018a).

Background Subtraction and Fitting

The estimation of the background caused several problems. At first, in Figure 3.33a it's possible to observe the spectrum obtained in a certain time bin for a corresponding temperature.

Due to both physics and electronics, the detector signals show a tail reaching the low values, tail that in case of the oxygen mixtures reached values lower than 100 keV. For this reason, the estimation of the background wasn't possible just considering the data (Mocchiutti et al., 2018a).
In order to overcome this issue, the group tried to consider the spectrum of the target filled with pure hydrogen at same temperature and pressure, observing in the better results, but not the best ones. Indeed, following this strategy, the obtained statistics was so low to generate fluctuations on the signal. These fluctuations were removed by using a gaussian kernel to smooth the hydrogen data set (Mocchiutti et al., 2018a). In this way, just the systematic errors remained, composed by the fluctuations generated by the normalization of background and type of subtraction. The net result was so a systematical fluctuations around the true value of the measure transfer rate. The test here explained was useful to determine the systematic error between $5\% - 20\%$, error that is summed to the statistical error in each spectrum, as can be observed in Figure 3.33b, where the fitting lines for time dependence are shown.

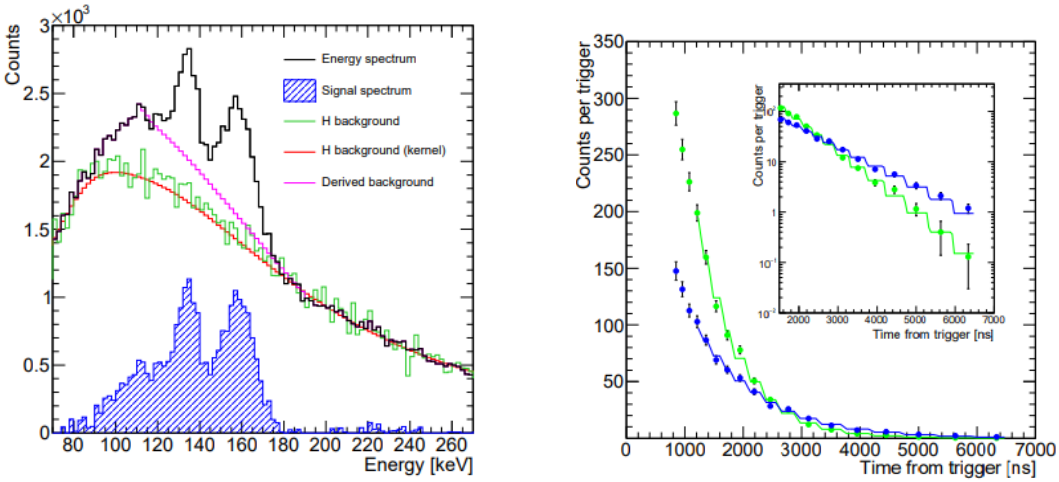

(a) **(b)**

Figure 3.33: (a) Example of energy spectrum signal. The time bin considered is between 1450 ns and 1650 ns. There are different lines: energy spectrum in black, signal spectrum in blue, H background in green, H background using the kernel in red and the derived background in pink (Mocchiutti et al., 2018a). (b) Oxygen signal in function of the time at 300 K (blue) and at 100 K (green). The statistical and systematic errors are summed up and shown in error bars (Mocchiutti et al., 2018a).

Results

The group in 2018 so obtained a preliminary test for the transfer rate in function of the temperature. This is, effectively, the first precise measurement of this dependence, shown in Figure 3.34. The work shows a good agreement with the results obtained previously at the PSI (Mocchiutti et al., 2018a).

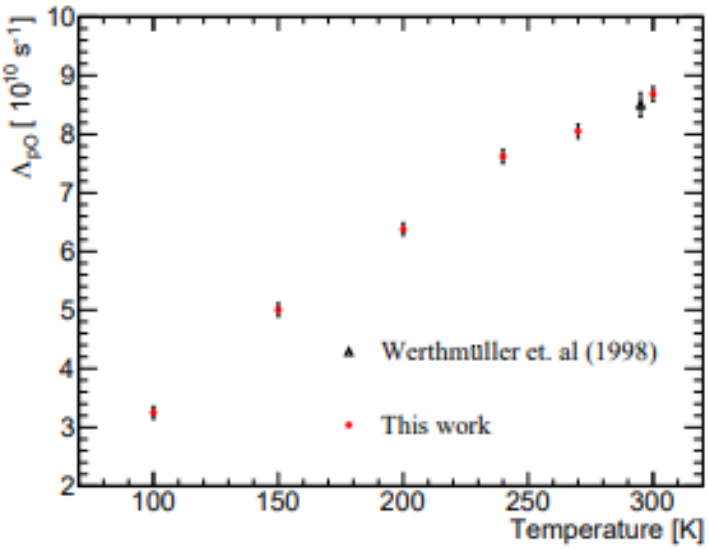

Figure 3.34: Result of the transfer rate in function of the temperature. This result is in accordance with the result obtained previously at PSI (Mocchiutti et al., 2018a).

3.2.3 2019

"First measurement of the temperature dependence of muon transfer rate from the μp atoms to oxygen"

The (Mocchiutti et al., 2020) experiment was performed using a target composed by a mixture of molecular Hydrogen and molecular Oxygen, this last with a concentration of 190 ppm. This value was chosen in order to have a longer mean life time of the μp atoms than 150 ns, allowing also a long-time observation (Mocchiutti et al., 2020).

The pressure considered was about 41 bar at room temperature and the experiment considers six temperatures controlled by two sensors: 104 K, 153 K, 201 K, 240 K, 272 K, 300 K. Each of these temperatures was maintained stable for three hours for the data extraction (Mocchiutti et al., 2020).

The number density of target was chosen to allow fast thermalization of the muonic atoms ($\leq$ 150 ns) and fast quenching ($\approx$ 10 ns).

In order to estimate the muon transfer, the time evolution of the muonic-oxygen lines must be studied with the consideration that the presence of the background of X-ray prompt emission must be suppressed, keeping just the steady-state delayed X-ray. This strong reduction has been performed by observing the muon transfer process after the end of the muon pulse (Mocchiutti et al., 2020).

The equations behind this study are Eqs. 3.1 and 3.2 while the values of the parameters can be observed in Table 3.9. The only unknown parameter, obtained using these equations, is $\Lambda_{pO}(T)$.

After the reconstruction of the X-ray signals using a fitting procedure, the combined efficiencies were about 95% that is constant above 2000 ns. This parameter tends to decrease up to 92% at 1200 ns (Mocchiutti et al., 2020).

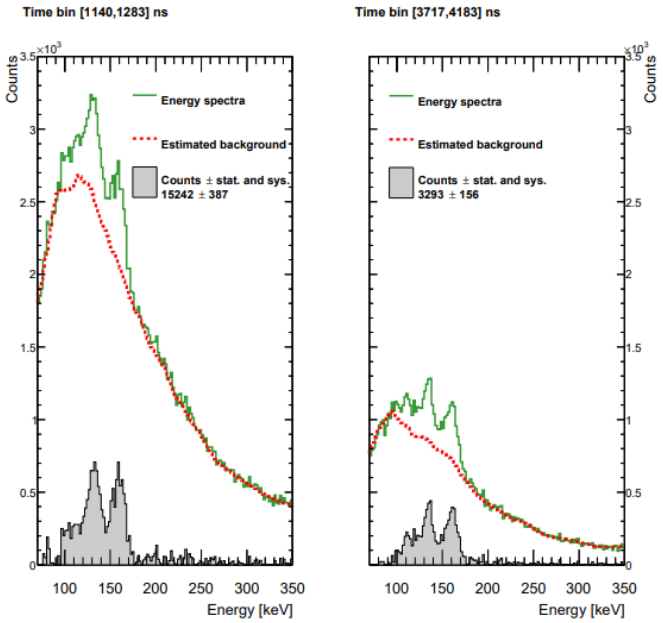

Figure 3.35: Spectrum of energy at 104 K with two time bins:$[1140, 1283]$ ns (left) and $[3717, 4183]$ ns (right). In both the figures: energy spectra (green line), estimated background (red line), signal without background (grey area) (Mocchiutti et al., 2020).

In Figure 3.35 are shown the energy spectra for a temperature of 104 K in two time bins: between 1140 ns and 1283 ns on the left and between 3717 ns and 4183 ns on the right. The red dots represent the line of the estimated background.

In Figure 3.36 instead the time dependence of oxygen is shown for two temperatures: 300 K and 104 K. The statistical and systematic errors, measured as described in the previous paragraph, are represented by the error bars.

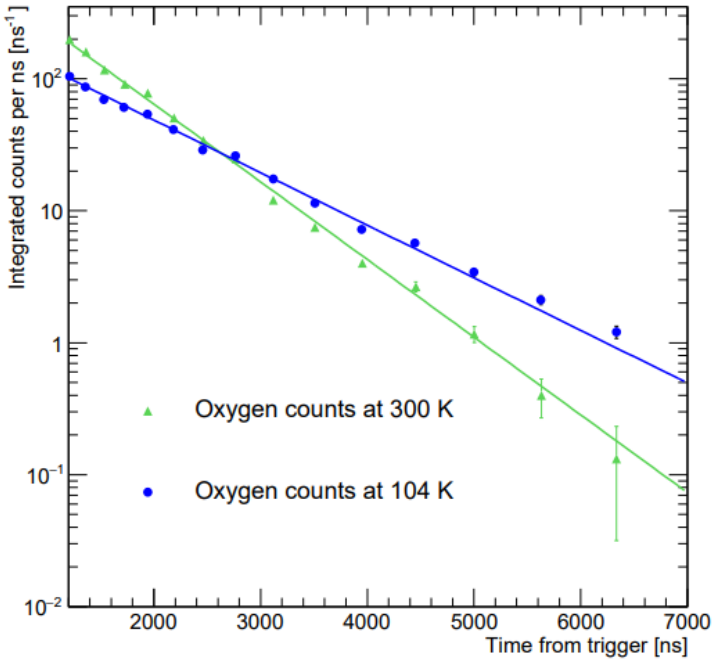

Figure 3.36: Time dependence of oxygen at two different temperatures of 300 K (green) and 104 K (blue). The different slope of the two curves is a symptom of the temperature dependence (Mocchiutti et al., 2020).

The fitting lines were obtained considering a time interval between 1200 ns, coinciding with the beginning of thermalized phase, and 6500 ns from trigger. Here, the dependence from the temperature is shown in the different slopes of the two lines. The values of muon transfer rate from the μp to the oxygen are shown in Table 1 with their corresponding temperatures (Mocchiutti et al., 2020).

Mean Temperature (K)	$\Lambda_{pO}(T)\,(10^{10}s^{-1})$
104	$3.25 \pm 0.10 \pm 0.07$
153	$5.00 \pm 0.11 \pm 0.10$
201	$6.38 \pm 0.10 \pm 0.13$
240	$7.62 \pm 0.12 \pm 0.16$
272	$8.05 \pm 0.12 \pm 0.17$
300	$8.68 \pm 0.12 \pm 0.18$

Table 3.10: Estimated transfer rate from muonic hydrogen to oxygen with corresponding temperatures (Mocchiutti et al., 2018a).

In the end, the result of the experiment is shown in Figure 3.37. The interval considered is between $0.01\,eV$ and $0.1\,eV$. This interval has been chosen because outside of this interval the contributions to $\Lambda_{pO}(T;P)$ from high-energy and lowest-energy intervals are very small (Mocchiutti et al., 2020).

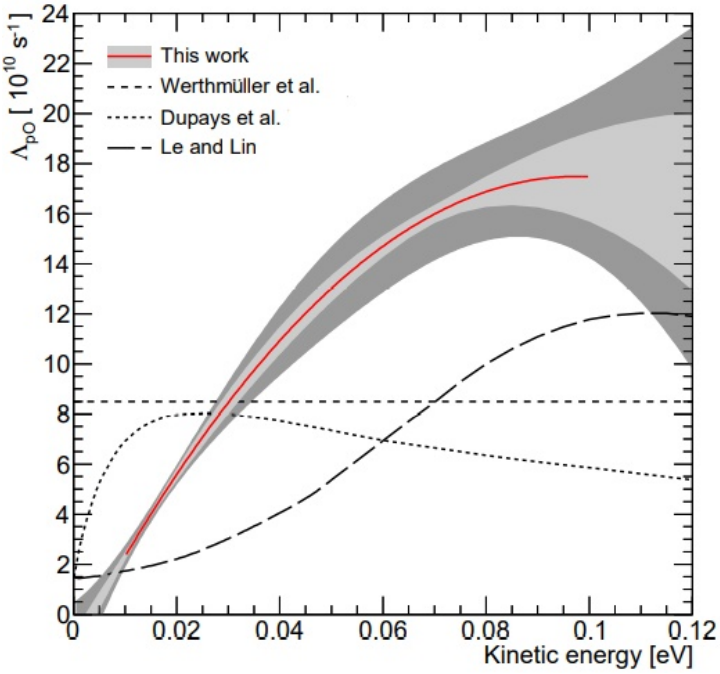

Figure 3.37: Λ_{pO} graph with respect to the other work results. The kinetic energy range is between $0.01\,eV$ and $0.1\,eV$. The shaded region corresponds to the uncertainties related to: experimental (light gray) and fitting-model (dark gray) (Mocchiutti et al., 2018a).

3.2.4 2020

"The FAMU experiment: muonic hydrogen high precision spectroscopy studies"

Since it is one of the most recent published article, the (Pizzolotto et al., 2020) has been widely used in this chapter to express the theories and the experimental apparatus behind the FAMU experiments. For this reason, the focus of this paragraph is on the Monte Carlo Simulations, together with parameters values and results that the group expected to reach in a real experiment.

To reach the final design of the detection system, the delayed background has been studied through several simulations taking in consideration the target conditions (pressure of $7\,bar$ at a temperature of $80\,K$) (Pizzolotto et al., 2020). The Figure 3.38 shows the different contributions to the background from the elements composing the target and the various material of the components of the detection system. Two peaks are quite visible, corresponding respectively to the K_α of oxygen at $\approx$ $130keV$ and to the unresolved K_β and K_γ at $\approx$ $160\,keV$. The group found that, in this configuration, the signal contained more than 50% of the total detector spectra (Pizzolotto et al., 2020).

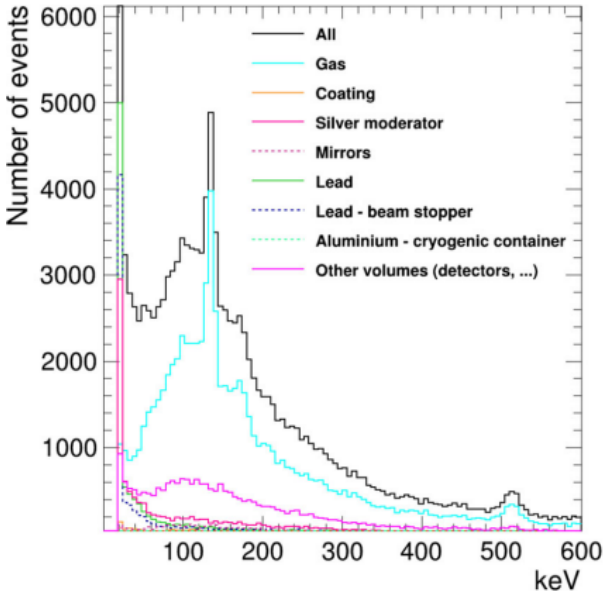

Figure 3.38: Simulation of energy spectrum coming from X-rays in the target system. Several contributions to the spectrum are represented (Pizzolotto et al., 2020).

The multipass optical cavity has been designed using a simulation tool called ray tracing, controlled by a MATLAB software (Pizzolotto et al., 2020).
In order to fulfill the cavity with light, a system of mirrors has been developed such that the light impinges on them about 1000 times, after been injected in the cavity by two parabolic mirrors. Working with this system, the lifetime of the photons in the cavity and the interaction path of μp are directly influenced, respectively 304 ns and 91 m (Pizzolotto et al., 2020).

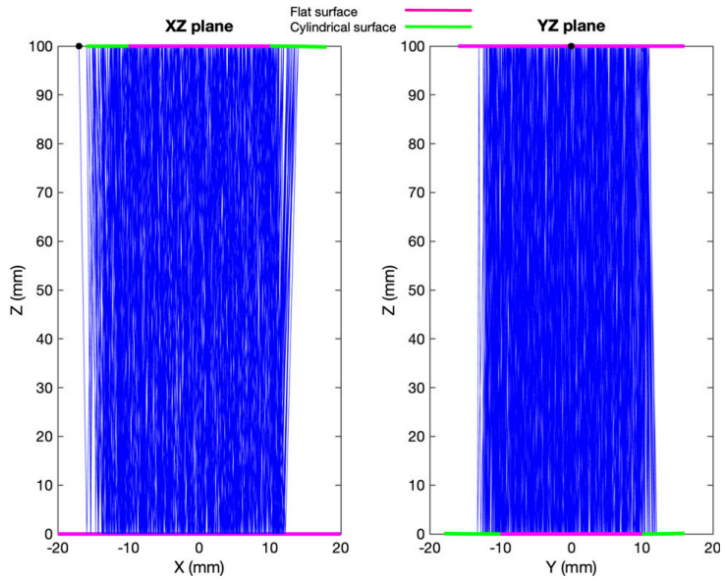

Figure 3.39: Ray tracing simulation. Black dots represents the injection parabolic mirrors. The colored lines represent the mirror: the green one refers to the cylindrical part of the mirror, the magenta one to the flat part instead (Pizzolotto et al., 2020).

By moving the parabolic system and so the injection angle, the beam focus changes, allowing an higher or lower ray path.
In Figure 3.39, a simulation of the ray tracing is shown, demonstrating the complete filling of the optical cavity.

In addition to the simulation, the beam parameters must be kept under control, in order to also avoid little fluctuations in shape and position of the beam. This control is performed by using a beam profile monitor. The system so developed allows the experiment group to: tune the beam, monitor the intensity of each beam pulse and deliver timing information (Pizzolotto et al., 2020).

Thanks to the Monte Carlo simulations, the number of muons formed in a $2 \times 2 \times 10\, cm^3$ can be determined. The group expected the 8% of the muons to form the muonic hydrogen, in comparison with what has been obtained in 2018 (Pizzolotto et al., 2020). Considering 12 detectors and 24 hours of work, an half with the laser and the other half without the laser, the number of the expected signal is about 12000 in both the situations.
In order to reach the goals of the experiment, 1% of statistical fluctuations has been estimated to be enough. Under these conditions, the Signal to Noise ratio was expected to be between 4 and 20 (Pizzolotto et al., 2020).

The estimation of a wavelength window around the expected resonance position is necessarily to understand the number of measurements to take. The resonance position, or the hyperfine splitting energy, is taken to be in an interval of width $0.00013\, eV$, equivalent $30\, GHz$.

By the way, when performing the experiments, the group took more measurements with respect to those necessary, between 100 and 200 (Pizzolotto et al., 2020).

3.2.5 2021

"Measurement of the muon transfer rate from muonic hydrogen to oxygen in the range $70 - 336\, K$"

The exploration of the temperature dependence of the muonic atoms transfer rate takes an update in 2021 with the (Pizzolotto et al., 2021) in which an enlargement of the temperature interval has been considered, specifically between $70 - 336\, K$.

The experimental apparatus to which the article refers is that of the 2018 (Adamczak et al., 2018).

As for previous experiment, the temperature dependence of the muon transfer from muonic hydrogen to oxygen is measured by changing the temperature of the target in a certain interval.

The data used in this analysis were performed in March and December 2018, under the same experimental conditions (Pizzolotto et al., 2021). Since the cryogenic compressor works at a pressure of $22.8\, bar$, which corresponds to a temperature of $350\, K$, the maximum temperature consider was about $340\, K$.
For what concern the data taken in March, four temperatures were considered: $272\, K$, $300\, K$, $323\, K$ and $336\, K$. Also, in order to reduce the vibrations transmitted to the laser system, the final experiment is performed using liquid hydrogen. In December, instead, the experiment is performed to obtain data at the temperature of the liquid nitrogen, $80\, K$, while lower temperatures are used to explore the region of the oxygen condensation (Pizzolotto et al., 2021).

Within the first two hours, the temperature decreased almost linearly from 300 K to 30 K and the data in the interval $[100, 300]\,K$ were confronted with the data extrapolated in the first measurement of the temperature dependence. The experimental conditions were different of course, but it was necessarily to study the oxygen concentration (Pizzolotto et al., 2021).

In Figure 3.40a the time-dependence of H_2/O_2 in the two dates is shown while in Figure 3.40b an example of digitized waveform is depicted. The starting time of the pulse, t_s, is measured by using a first derivative of the waveform larger than three times the local average fluctuations. In the end, the baseline with a RMS larger than 20 ADC counts are rejected in order to increase the resolution (Pizzolotto et al., 2021).

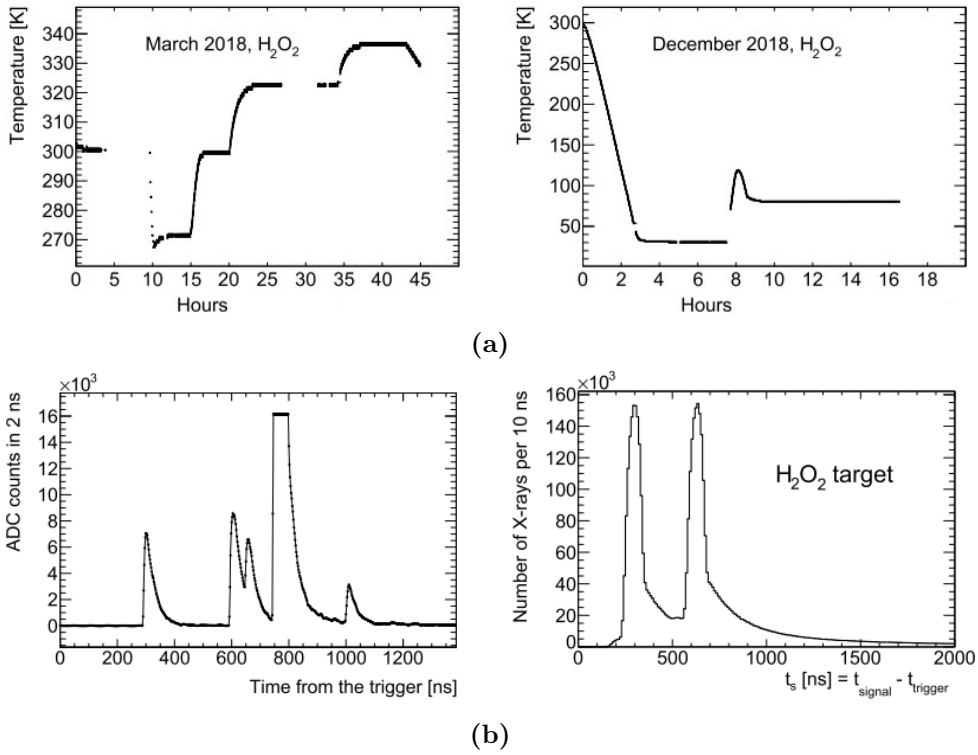

Figure 3.40: (a) Time dependence of H_2/O_2 target temperature in March (left) and in December (right) (Pizzolotto et al., 2021). (b) Left: Example of digitized waveform where different cases are shown: well separated pulses (first and fifth peaks), overlapping pulses (second and third pulses), saturation of FADC counter (fourth). Right: Example of starting time distribution of the signals when muons are captured by the target (Pizzolotto et al., 2021).

When the first derivative of the waveform goes back to zero the pulse amplitude is recorded. The pulses are rejected in one of these cases (Pizzolotto et al., 2021):

- The pulse doesn't go to zero (unresolved pulse) or are above this pulse;
- Time separation between peaks lower than 30 ns for which the pile-up effects verify;
- Pulses that saturate the FADC counter (214).

Using prompt X-rays from the elements of the target like Aluminum and Nickel and the delayed X-ray signals from oxygen ($133\,keV$) and from electron-positron annihilation ($511\,keV$) the pulse amplitude is calibrated in energy (Pizzolotto et al., 2021).
Figure 3.41 shows the calibration curve of the $LaBr_3$)(Ce) in which the points are obtained by fitting the pulse-height spectrum with a combination of gaussian peak and functional model. As can be observed, the relation between amplitude and energy corresponds to a second degree polynomial equation. The FWHM at a K_α line is about 10% (Pizzolotto et al., 2021).

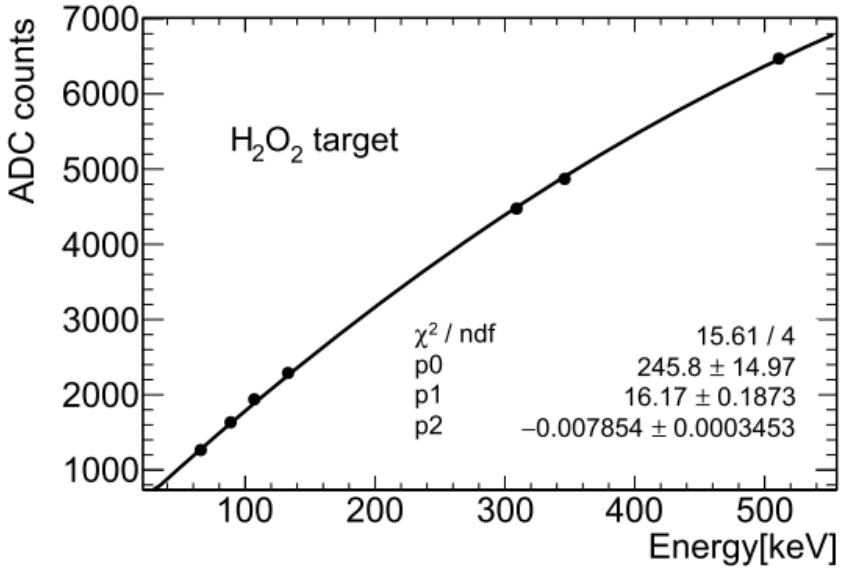

Figure 3.41: Calibration curve of $LaBr_3$(Ce) detector showing the relation between the amplitude and the energy (Pizzolotto et al., 2021).

In Figure 3.42 the energy spectrum using all the detectors of the delayed X-rays is shown. The gray area represents the background, normalized in energy range without X-ray lines between $250\,keV$ and $350\,keV$. The first peak corresponds to the K_α while the second corresponds to the unresolved K_β and K_γ lines (Pizzolotto et al., 2021).

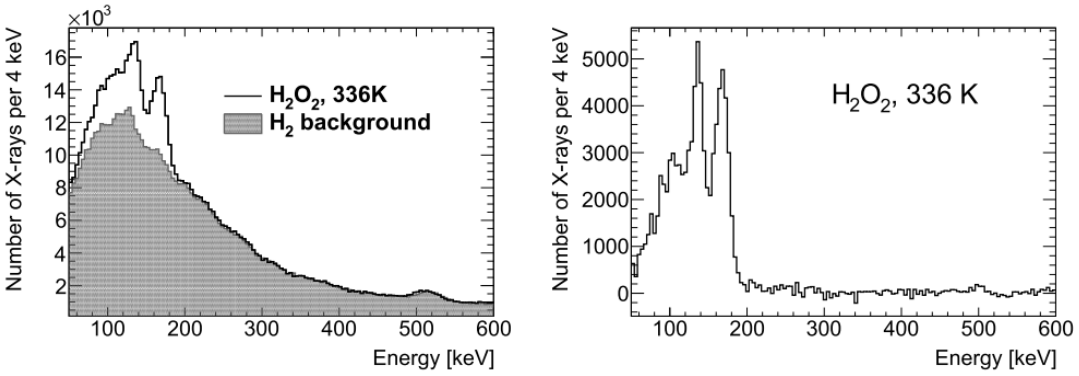

Figure 3.42: Energy spectrum with H_2 background subtraction (right). Energy spectrum of delayed X-rays produced in the target in the range $900\,ns - 1200\,ns$ (Pizzolotto et al., 2021).

Figure 3.43 shows the time dependence muon transfer rate to oxygen using all the detectors. In March, the data are divided in $50\,ns$ starting from $900\,ns$ while in December the data start from $1000\,ns$ with the bins obtained logarithmically (Pizzolotto et al., 2021).

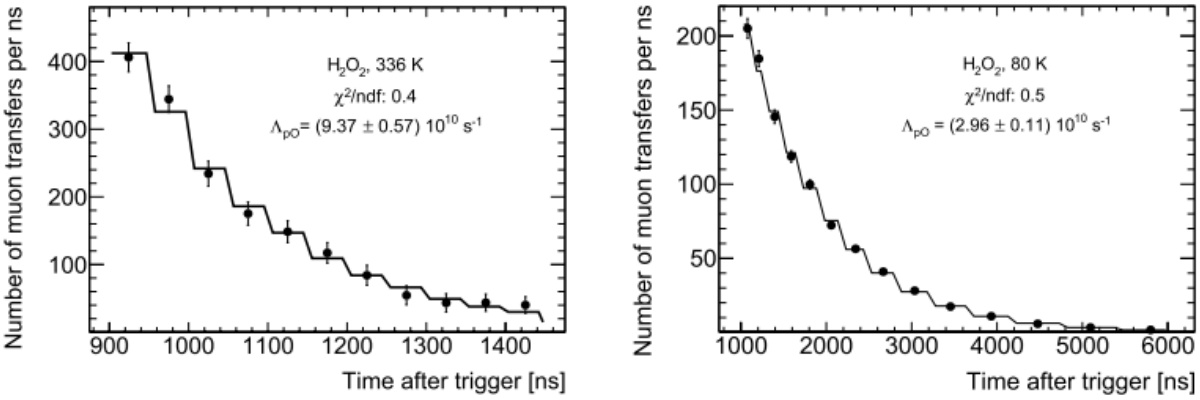

Figure 3.43: Muon transfer rate time dependence measured in March (left) and in December (right) using all the $LaBr_3(Ce)$ detectors (Pizzolotto et al., 2021).

Considering a temperature interval between $70\,K$ and $336\,K$, the values of the measured muon transfer rate from muonic hydrogen to oxygen are shown in Table 3.11.

T (K)	$\Lambda_{pO}(T)\,(10^{10}s^{-1})$
70	$2.67 \pm 0.40 \pm 0.32$
80 ± 0.5	$2.96 \pm 0.11 \pm 0.36$
323 ± 0.5	$8.88 \pm 0.62 \pm 0.66$
336 ± 0.5	$9.37 \pm 0.57 \pm 0.70$

Table 3.11: Estimated transfer rate from muonic hydrogen to oxygen with corresponding temperatures. The first error corresponds to the sum in quadrature of statistical and systematic uncertainties associated to background subtraction. The second corresponds to systematic error associated to the target gas composition (Pizzolotto et al., 2021).

These values are reported in Figure 3.44, compared to the values measured in 2016 and other previous results (for the experimental results obtained from Werthmüller et al., Dupays et al. and Le and Lin, refer to the bibliography of (Pizzolotto et al., 2021)).

The temperature dependence of Λ_{pO} confirms the relation between temperature and muon transfer rate and extends it in a larger range of temperature.

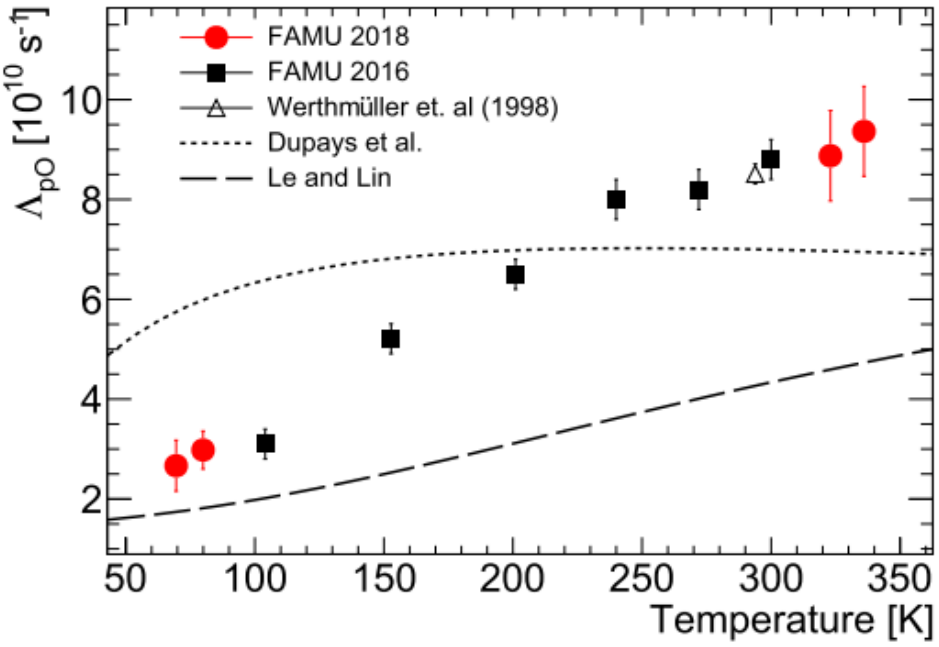

Figure 3.44: Measurement of the muon transfer rate Λ_{pO} as function of the temperature compared to previous results (Pizzolotto et al., 2021).

Chapter 4

Circuitry

The overall circuit of each module controlling the detection has been described in this chapter.

Figure 4.1 represents a scheme of one module, all the others share exactly the same configuration. Also, one module controls one and only one detector.

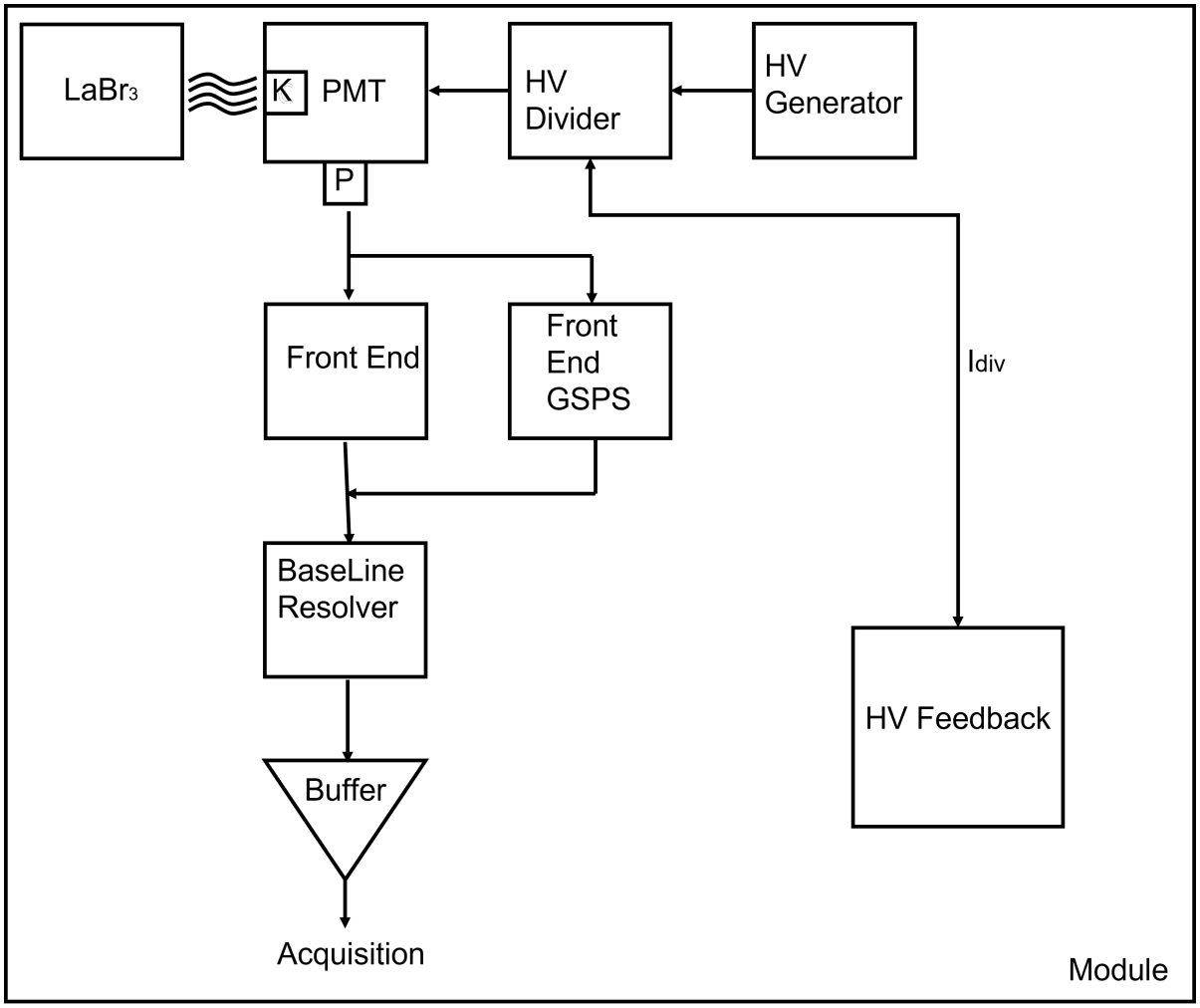

Figure 4.1: General Circuit of a module. The two main components are shown. The First Block comprises: $LaBr_3$, PMT, HV Generator, HV Divider, the two Front End, the BaseLine Resolver and the Buffer. The Second Block is composed by the HV Feedback.

Each module then can be considered as composed by two main parts:

- First Block of the Circuit:
  - High-Voltage Generator;
  - High-Voltage Divider;
  - PhotoMultiplier Tube;
  - First Front End;
  - Second Front End, optimized for the GSPS;
  - BaseLine Resolver;
  - Buffer.
- Second Block of the Circuit:
  - High-Voltage Feedback.

4.1 First Block of the Circuit

4.1.1 High-Voltage Generator

The HV Generator takes in input voltages equal to $\pm 5\,V$. This generator at high precision provides voltages that vary very little as the temperature changes. Its voltages are injected directly in the HV Divider which, in turn, provides it to the PMT.

4.1.2 High-Voltage Divider

In this first part of the circuit, the coupling is bright. It means that the arrival of a photon produces scintillation light, successively collected from the PhotoMultiplier Tube, represented in Figure 4.2.

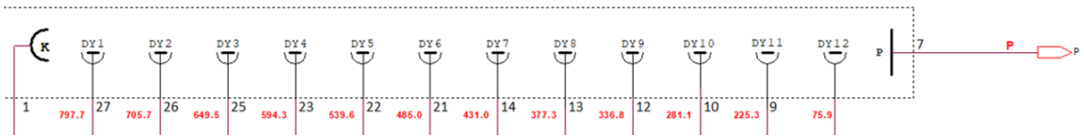

Figure 4.2: PhotoMultiplier Tube circuit. Thirteen dynodes are positioned with increasing voltage, starting from a negative voltage on the cathode and ending with a more positive one on the anode.

In the PMT, the dynodes are positioned at a negative voltage on the cathode, with a more positive one from dynode to dynode such that the electrons can be attracted to the next dynode and reach so the anode. This positive escalation of voltage from one dynode to the next one is given by the HV Divider. The High-Voltage (HV) Divider has been studied for a long time due to the innovative characteristics of the Lanthanum Bromide, as the high counting rate with a yield of light higher than 120% and responses of the order of 10 ns. The outcoming phenomenon is a large amount of light in a very short time which results in extreme energy pulses causing high currents on the dynodes. To respond at these high currents, the capacitance must be high so the capacitors can provide the required energy to all the pulses and not just to one of them. Different capacitance are positioned, as shown in Figure 4.3:

- The first line has capacitance of the order of $1\,nF$ but is faster than the other lines;
- The second line has capacitance of the order of dozens of $10\,nF$ with slightly lower speed;
- The last line has higher capacitance with respect of the others (order of hundreds of nF) but they are much slower.

The response so occurs starting from the faster line up to the slower one. In all the stages, the MOSFETs, shown in Figure 4.3, with a response of the order of $4\,ns$ have the function to keep the slower capacitors charged such that they charge the faster ones. In this way, the system is able to respond even in case of higher amount of pulses per second ($> 3\,Mpulses \cdot s$). It would possible to work also with

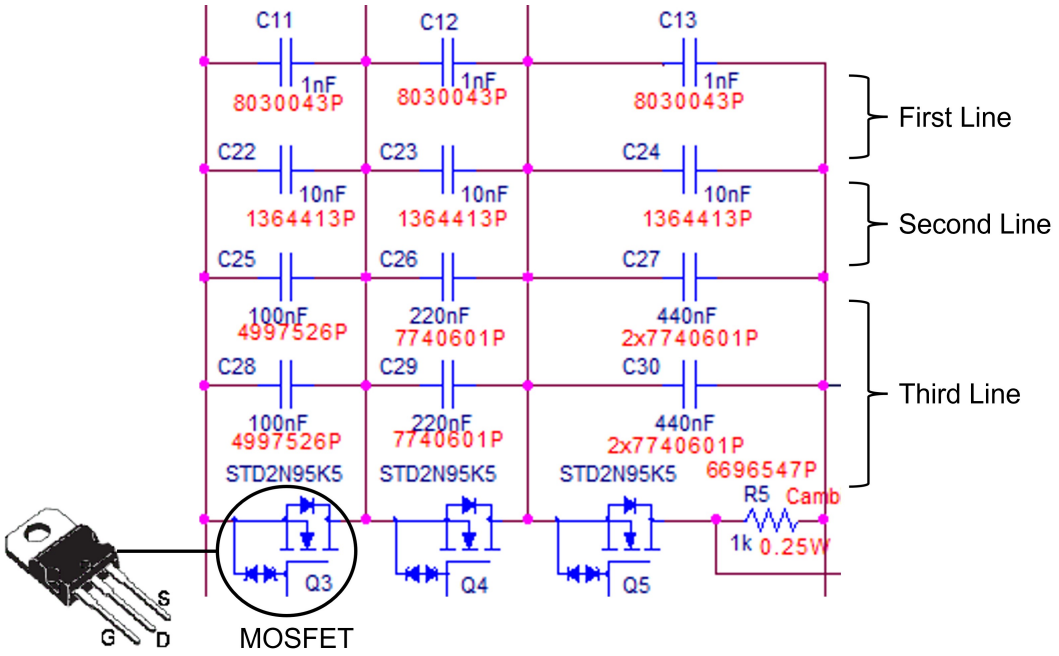

Figure 4.3: Capacitors block together with the MOSFET. The first line of is the fastest, the second is a slightly slower while the third line is the slowest. The MOSFETs ensures all the capacitors to be charged.

$5\,Mpulses \cdot s$ but at that point the response of Lanthanum Bromide will be no longer linear.

As shown in Figure 4.4, between the end of the HV Divider and the ground there is a resistance of $R = 2200\,Ohm$. Considering a certain voltage applied (V) and the total resistance (R_{tot}) of the circuit it's possible to measure the current (I) flowing in this part of the circuit, as in Eq. 4.1.

$$I = \frac{V}{R + R_{tot}} \tag{4.1}$$

Knowing the current, it's possible to extract the module of the voltage drop (ΔV) at the ends of R, as shown in Eq. 4.2.

$$\Delta V = I \cdot R \tag{4.2}$$

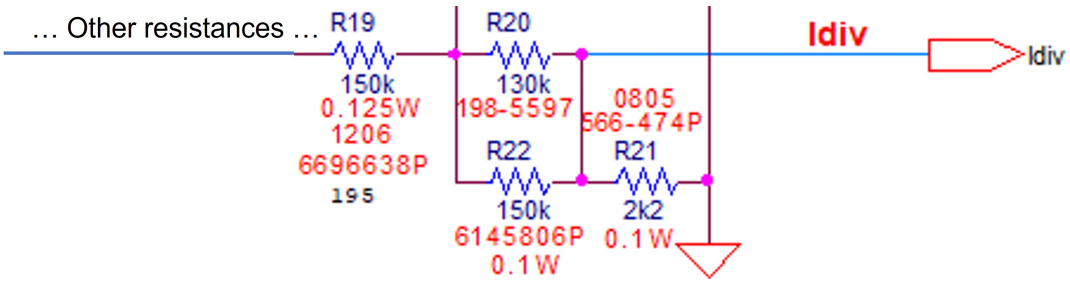

Figure 4.4: I_{div} voltage part of the circuit.

This voltage is indicated as a current since it is used specifically to determine how much current flows in the circuit. In less words, these voltage represents a monitor that tells the value of the HV on the HV Divider and the current.

To be mentioned, the HV is negative which means that also I_{div} is negative and it is not used so.

Just in paragraph 4.2.1 the I_{div} will be used while in the next paragraphs the input of the circuits will be the signal coming from the anode.

4.1.3 First Front End

The First Front End is just a simple Current-to-Voltage Converter, the stage of which can be seen in Figure 4.5.

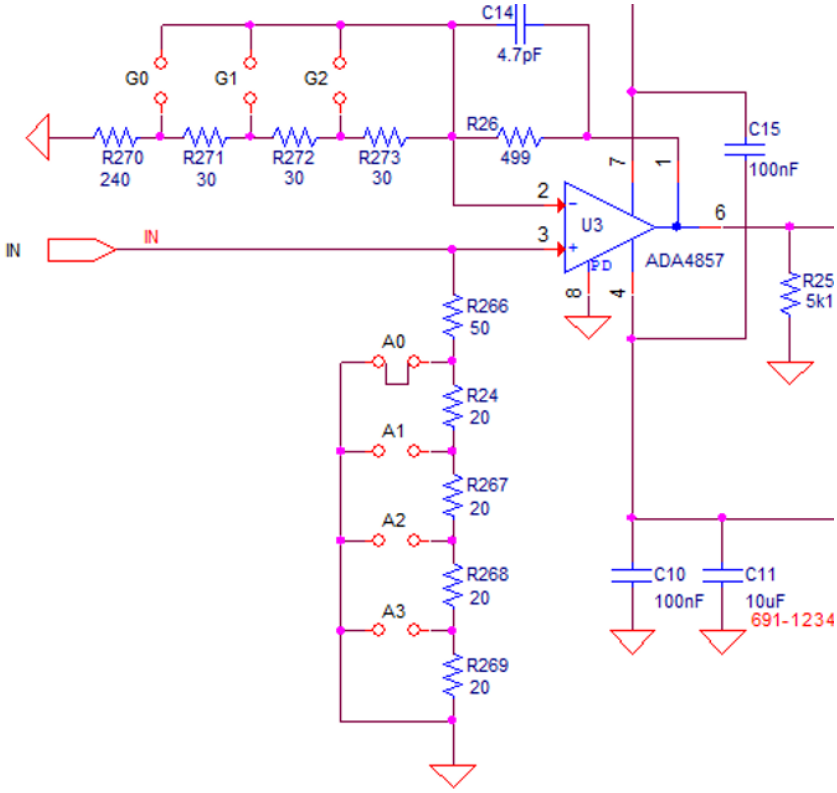

Figure 4.5: First Front End circuit. The signal passes through the operational amplifier and arrives on the resistance ($R25$) on which it's possible to measure the voltage drops.

Due to the high speed of the pulses the circuit is composed by a very high quality operational amplifier with a bandwidth of 750 MHz. The anode output passes through the amplifier and then it goes on to a resistance making possible to measure the voltage drop at its ends. Exiting from the Front End, the signal enters in the next stage: the BaseLine Restorer.

4.1.4 Second Front End

This kind of Front End is optimized for the GSPS system but it is also much complicated than the first.

The negative signal coming from the anode of PMT enters in the Charge Sensitive PreAmplifier (CSP) and it goes in a couple of integrated called Current Mirrors, installed to maintain the Feedback Capacitor discharge.

In the end, the output signal is a positive peak that must be inverted since the signal that enters in the BaseLine Restorer must be negative.

Charge Sensitive PreAmplfier

The CSP is composed by an amplifier stage at very high impedance and a Feedback Capacitor, as shown in Figure 4.6.

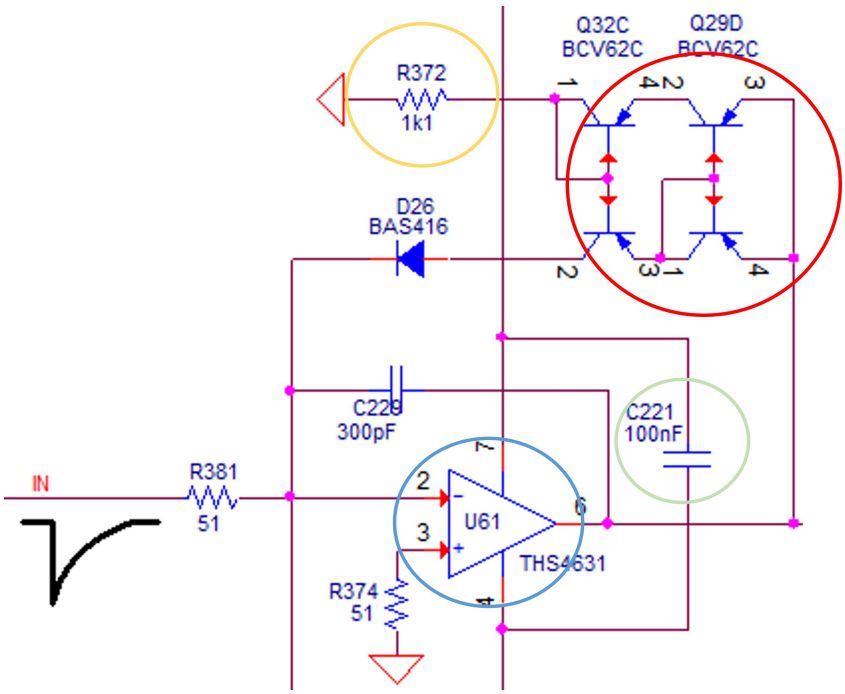

Figure 4.6: CSP circuit. The negative signal enters in the CSP (blue circle), passes through the Current Mirror system (red circle) and exits as a positive peak. Other two elements have been highlighted: the capacitor to keep discharged (green circle) and the resistance controlling the current flowing in the branches of the Current Mirror.

Since the gain can be obtained as:

$$G = \frac{1}{C_{feedback}} \tag{4.3}$$

smaller capacitance on the circuit will mean a higher gain. The feedback capacitor is typically used to read signal from the solid state. Since the signal from the PMT is already a very large value, the capacitance of this capacitor should be greater ($\approx 300\,pF$) than the usual case. Once a pulse arrives to the capacitor, it charges itself to reach the amplitude of the pulse and maintain this value. This mechanism is executed for all the incoming pulses and at some point the saturation level, given by the supply voltage, will be reached. This causes the saturation of the amplifier that will be blocked for a non insignificant period of time. The common solutions (that have been discarded) are the following:

- Usually, to maintain discharged the system, a resistance is placed in parallel to the capacitor. This resistance will discharge the capacitor whenever a pulse

reaches it. Since the resistance introduces a lot of thermal noise (also known as Johnson noise), it's value should be very high to reduce significantly the noise.

Now, the falling edge of the peak is represented by:

$$\tau_{falling} = R \cdot C_{feedback}$$

and so it means that the curve will have a very fast rising edge but a very slow falling edge, with a period of time of several orders higher than that of the rising edge. This is a problem considering that the experiment requires a high count rate. So, adding a resistance it's not a possible choice;

- A transistor is also another solution. It will work as a switch to short-circuit the input and to discharge the input without using the resistance. The use of this component will require a more complicated circuit, introducing a comparator, a flip flop and so on. In this way, maintain a high SNR will be very difficult and so neither this is a good choice.

The choice falls on the Current Mirror to discharge the capacitor, a system that takes the current on one transistor and replicates it on the second transistor. Two of them are placed in cascade in order to have a much higher impedance as required by the CSP. So the Current Mirror takes the polarized voltage from the CSP and, thank to the resistance near the Mirror Current, a known current flows in the circuit.

So when there is a peak as input, it is inverted by the CSP. As the voltage of the peak increases also the polarized voltage of Current Mirror increases and so a current peak is generated that will be sent to the input. Doing this, two opposite peaks interact with the result to cancel the integration and so to reset the baseline. Working in this way, a CSP with continuous reset of the voltage is formed.

Considering the output of CSP, it doesn't have a zero output due to some slow moving voltage offsets. In order to cancel these effects a slow acting integrator is used, as shown in Figure 4.7.

It extracts the exit of the CSP and uses as feedback a capacitor and a resistance, both of high value.

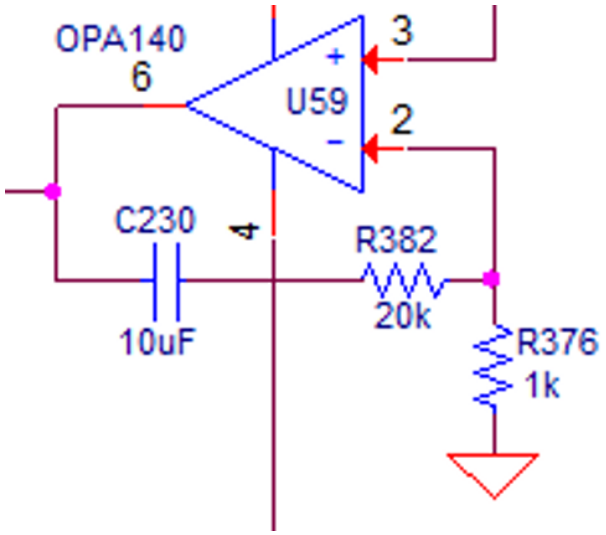

Figure 4.7: Circuit used to cancel the offset affecting the CSP output, using a capacitor and a resistance as feedback.

A difference between the Front End and this Second is that the last has a quick rising edge and a slow falling edge. For example, if the rising edge is of the order of 10 ns, the falling edge should take a period of time of the order of 100 ns, as shown in Figure 4.8.

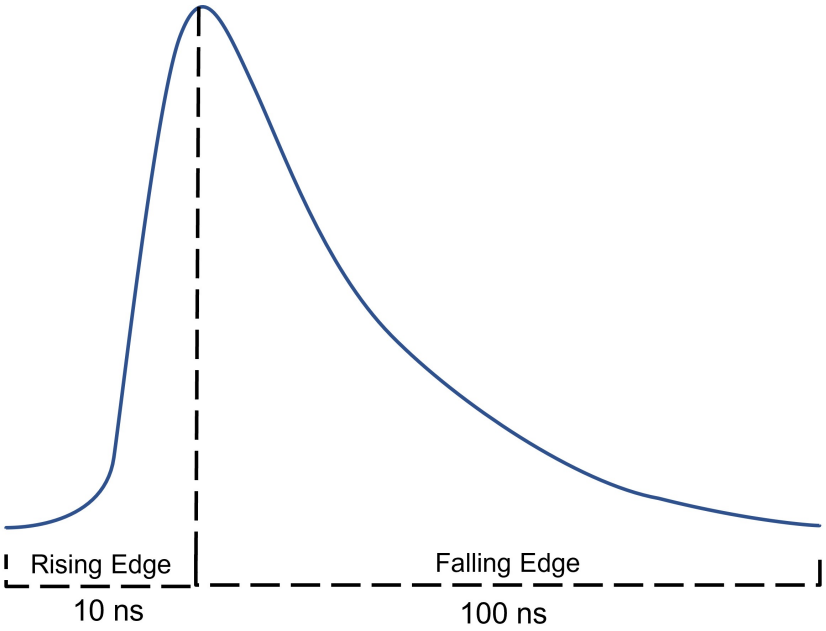

Figure 4.8: Example peak to show the difference between the Rising and Falling Edges in terms of times.

Before to enter in the Baseline Restorer circuit, the signal is inverted again using an operational, shown in Figure 4.9, since the BaseLine works only with negative signals.

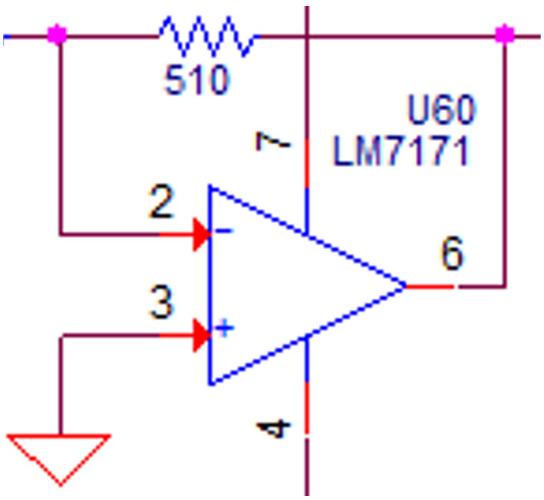

Figure 4.9: Operational to invert the signal coming from the CSP.

4.1.5 BaseLine Restorer

Due to the fast pulses and to the high rate count it could happen that consecutive pulses overlap, as shown in Figure 4.10. This overlapping causes the moving of

baseline, which would be otherwise fixed. The moving of the baseline is the primary cause of the problems in measuring thoroughly the peak amplitude.

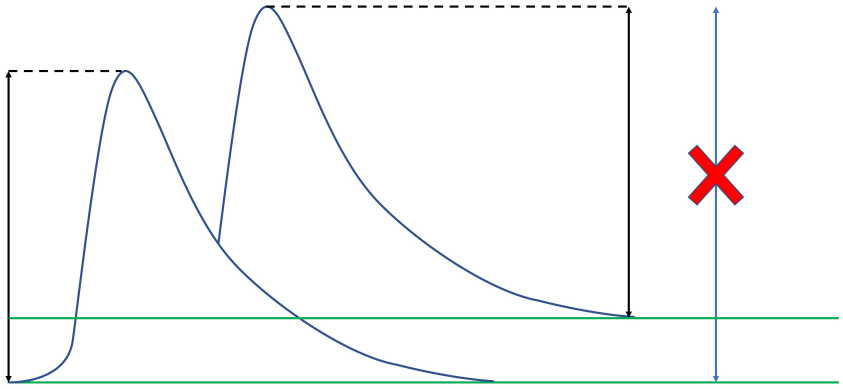

Figure 4.10: The overlapping of the pulses (blue curves) causes the movement of the baseline (green line) with subsequent problems in the measurement of the peak amplitude.

So the baseline needs to be maintained constant and the Restorer is used for this task. Its circuit is shown in Figure 4.11.

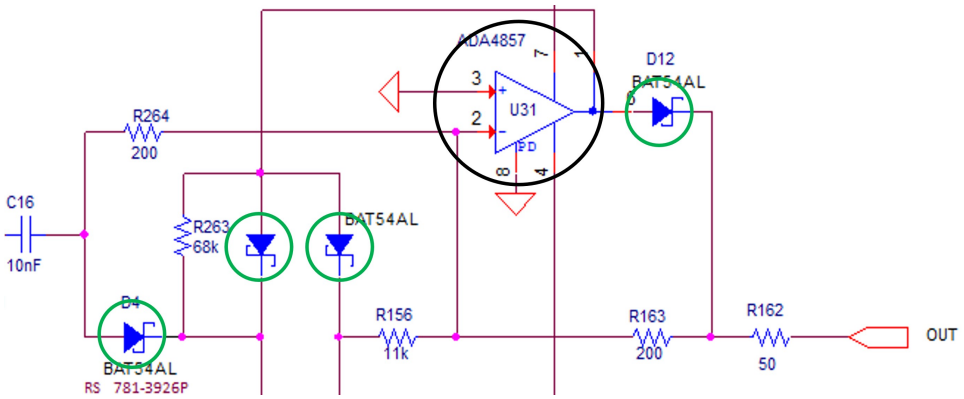

Figure 4.11: Circuit of the BaseLine Restorer. In black there is an operational working also as Buffer, as explained in 4.1.6. In green are shown the Schottky diodes.

Basically, the BaseLine Restorer contains several Schottky diodes that are very fast and have a gap of about $0.3\,V$ which results in a very low voltage drop. These diodes open and close as switches depending on where the pulse is in that moment. The effect is that of a very small cut of the tail at its end. This cut is so small that is not visible and the pulse seems to go to zero perfectly, as shown in Figure 4.12.

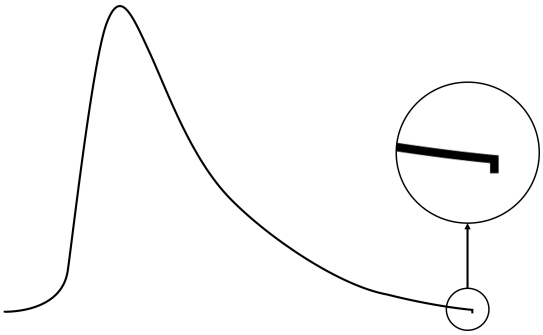

Figure 4.12: Small cut at the end of the tail of the pulse.

4.1.6 Buffer

As shown in the previous paragraph, the BaseLine Restorer contains an operational that works as a Buffer. Its scheme is shown in Figure 4.13.

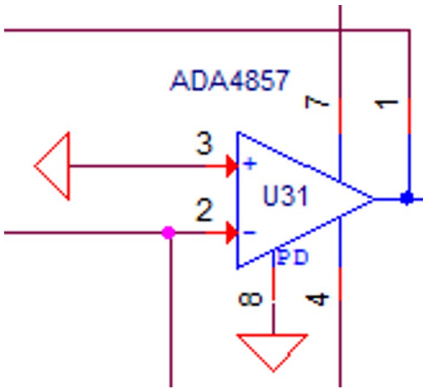

Figure 4.13: Buffer circuit

The Buffer is introduced just to increase the signal current since it passes through $3\,m$ of coaxial cables in which the signal risks to disperse with subsequent increase of noise.

4.2 Second Block of the Circuit

4.2.1 High-Voltage Feedback

From now on the input of the circuit will be the I_{div} voltage.

Filtering and Gain Control

In the first stage, the voltage I_{div} is inverted, filtered and the gain is controlled, the circuit shown in Figure 4.14. So, I_{div} enters in the circuit and passes through a buffer with an impedance so high that the HV Divider doesn't even notice the extraction of signal. After the Buffer, the signal enters in another operational amplifier which has the objective of inverting the signal, converting I_{div} in a positive voltage. In addition, the circuit of this amplifier contains a filter to eliminate the frequencies higher than $15\,KHz$. This filter is necessary from the moment that, extracting I_{div}, also the high voltage noise of the HV Divider will be present and it requires to be removed.

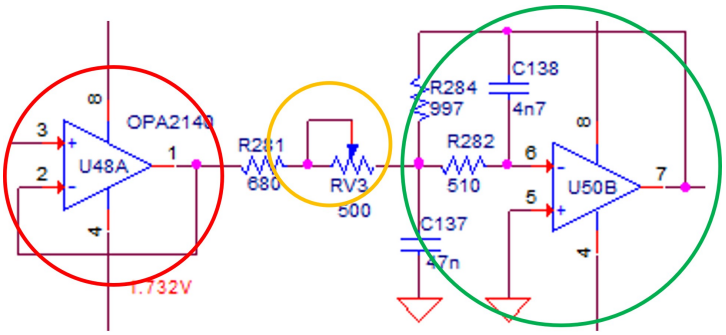

Figure 4.14: Schemes of: Buffer Circuit used in the HV Feedback (red circle), Control Potentiometer to vary the gain (yellow circle), Operational Amplifier containing also the filter to remove the frequencies higher than $15\,kHz$ (green circle).

Always looking at the Figure 4.14, between the buffer and the amplifier, there is a control potentiometer, able to change the gain of this stage. In the end so, a voltage AI is obtained. This voltage is of course proportional to I_{div} and also to the High Voltage. If the High Voltage changes in one verse or another, even the AI voltage changes in the same direction.

The proportionality factor between the High Voltage and the AI voltage depends on this control potentiometer.

Until now, the circuit can be considered as shown in Figure 4.15.

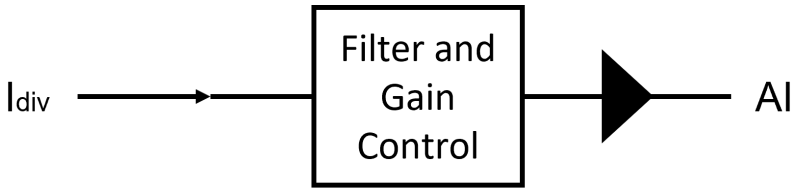

Figure 4.15: Representation of Filter and Gain Circuit.

High Voltage Control

The first component to consider for this part of the circuit is the Digital Potentiometer, shown in Figure 4.16. This potentiometer gives to the circuit a variable voltage between 0 and $+2.5\,V$.

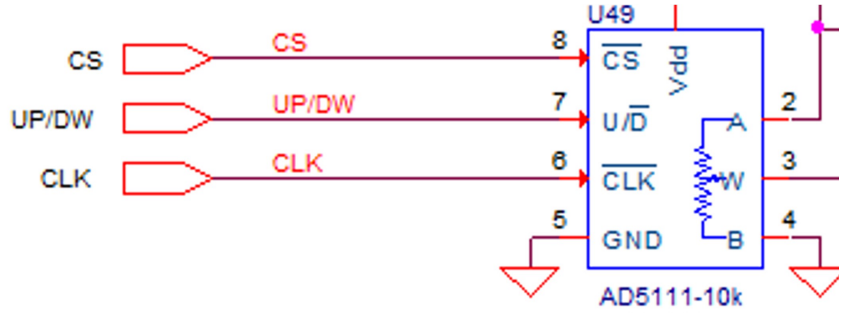

Figure 4.16: Digital Potentiometer Component.

The signal coming from the digital potentiometer is used to control an optocoupler, a diode led shown in Figure 4.17. This diode led is powered by a current, an amplifier and a potentiometer. If the resistance increases, a lower current will flow in the optocoupler which will produce a less intense light. This optocoupler is fundamental when it is coupled to a MOSFET.

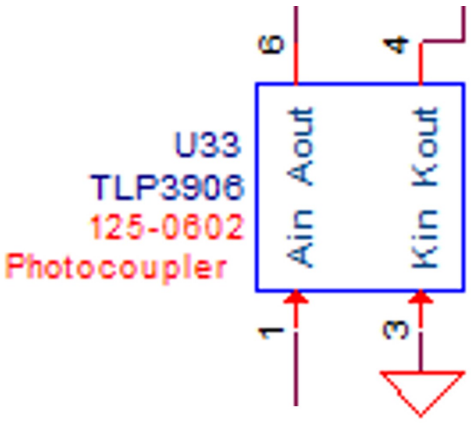

Figure 4.17: Optocoupler circuit.

Indeed, the MOSFET of the circuit works as a sink, controlling how much of High Voltage flows according to how much voltage is applied to the Gate. The voltage applied to the Optocoupler so is fundamental: in order to control this value, a second potentiometer is inserted in the circuit. This potentiometer adjusts the polarization on the optocoupler which will release a certain amount of light.

It's important also to notice that the analog potentiometer fixes the High Voltage while the digital potentiometer modifies this value remotely. Anyway, before to fix the value of the analog potentiometer, the value of the digital one also needs to be checked: if its value is already too low or too high, the analog potentiometer won't be able to reach a desired value.

The representation of this part of the circuit can be observed in Figure 4.18.

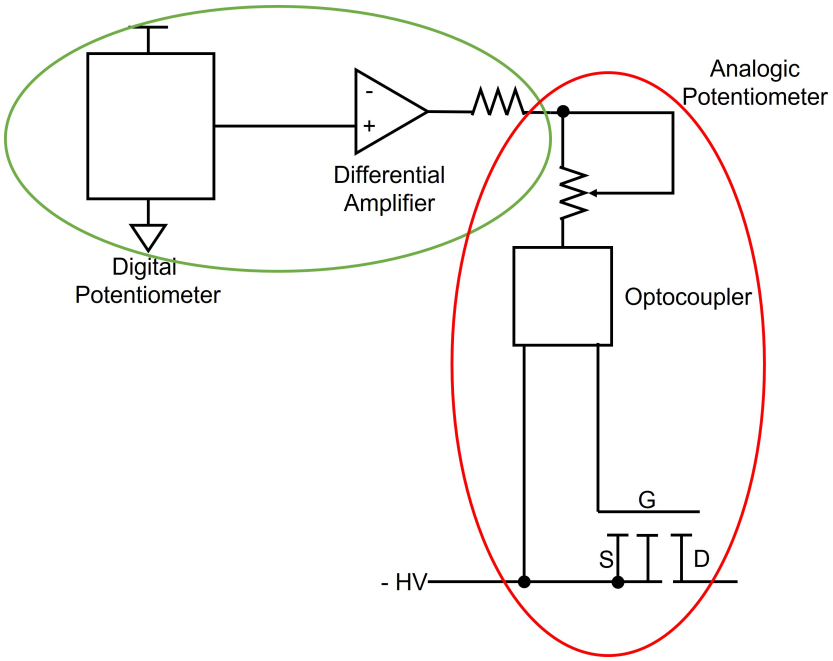

Figure 4.18: Scheme of the High Voltage Control part. In green there is the part related to the Low Voltage while in red is circled circuit related to the High Voltage.

Observing this last figure, there are two parts of the circuit characterized one by the Low Voltage and the other by the High Voltage. Indeed, the green part works with $5\,V$ and so there is the need to separate the two parts: the optocoupler has this task. It short-circuits the input of High Voltage from that of Low one.

4.3 Last Link

Now, the two parts of the HV Feedback need to be linked and to do that the I_{div} voltage from 4.1 enters in the negative pin of the differential amplifier of 4.2, as shown in Figure 4.19.

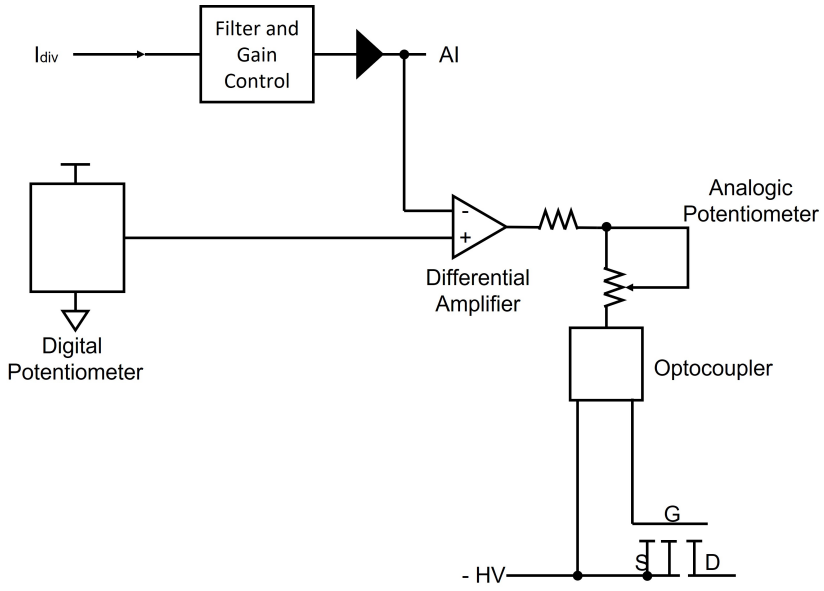

Figure 4.19: Scheme of the circuit obtained joined the two blocks already explained.

In this way, on the positive pin enters the voltage fixed with the digital potentiometer while on the negative one enters the AI voltage, proportional to the real High Voltage.

So the voltage outcoming from the differential amplifier, which in turn controls the High Voltage sink, is given by:

$$V_{outcoming} = V_{digital} - V_{AI} \tag{4.4}$$

This underlines two different behavior with the same objective:

- Suppose that, fixed the voltage using the digital potentiometer, if the real High Voltage flows and increases, from $V_{digital}$ is subtracted a higher value and the outcoming voltage that passes in the circuit will be lower;
- On the opposite case, if the real High Voltage flows and decreases, from $V_{digital}$ is subtracted a lower value and the outcoming voltage that passes in the circuit will be higher.

According to what already explained, this circuit is a negative feedback used to stabilize the High Voltage, maintaining the fluctuations under control.

This circuit has a certain response time, slower with respect to the other parts. This is necessary since in the circuit there are other feedback and with the same response time there can be some interference.

In the end, the efficacy of the feedback is controlled by the control potentiometer which establishes the proportionality between the voltages.

Chapter 5

Detectors' Characterization

In this chapter two main topics will be presented.

At first there is an explanation of the LabView screen that is used to control the semicircular crown in which are positioned the detectors. Together with the LabView screen, also the preliminary phase is shown: which is the order of executions, which parameters must be focus on and how to setup the GSPS command script.

In the end, the results of this project are presented, for each of the available detector.

5.1 Preliminary Phase: LabView and Oscilloscope

In order to characterize each detector there are some steps to follow. These steps are based on the use of a LabView program to control the circuitry of the detection system, which is shown in Figure 5.1. An Oscilloscope instead is used to visualize the signals coming from the circuit, like the pulses and the voltages from the feedback components.

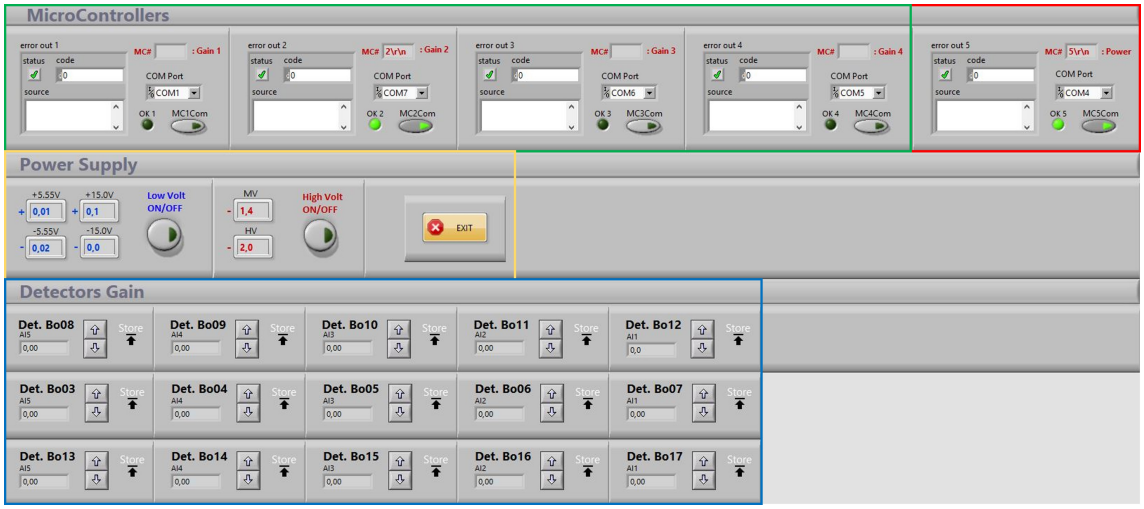

Figure 5.1: LabView screen to control the entire crown. The different parts are the following: Microcontroller 5 (red square) used to check the Low and High Voltages; Microcontrollers $1, 2, 3, 4$ (green square)controlling each quadrants; the Low and High Voltages button (yellow square); Detectors' Digital Potentiometers with UP and DOWN button (blue square).

The steps to follow for the characterization are the following:

1. The Microcontroller 5, shown in Figure 5.2, needs to be activated. Indeed, this is the command related to the Teensy that checks the Low and High Voltages and make them readable in output;

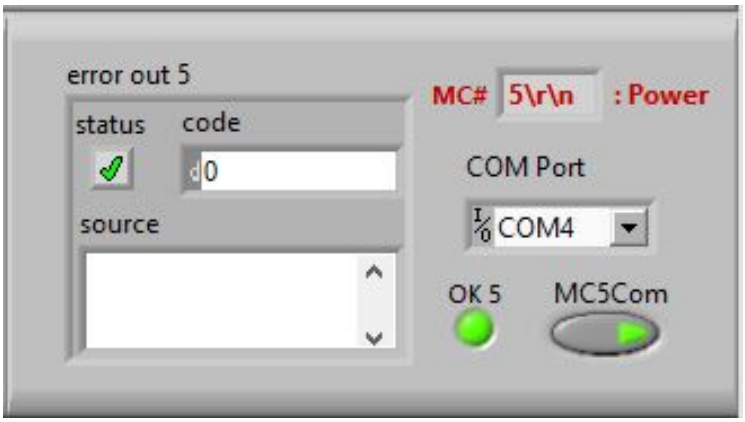

Figure 5.2: Block containing the power button of the Microcontroller 5. The white blank space is used to display the codes of errors if they are present.

2. The teensy related to the quadrant under investigation needs to be used. Depending on how many of the quadrants one wants to consider, one or more of them can be used at the same time. The corresponding commands are shown in Figure 5.3. This kind of teensy is the one that contains the necessary programming to increase or decrease the High Voltage and basically it controls the so called Digital Potentiometer;

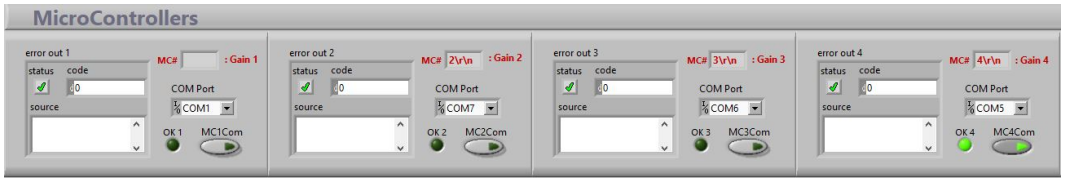

Figure 5.3: Commands to activate the teensy controlling the quadrants. The Microcontroller 1 is related to detectors 1 and 2, the Microcontroller 2 controls the detectors from 3 up to 7, the Microcontroller 3 those from 8 up to 12 and the last Microcontroller controls the last five detectors.

3. Turn on the Low and High Voltages, precisely in this order. Indeed, the Low voltage need to flow as first in the circuit to supply current to all the components of the circuit and just then the High Voltage button can be clicked. Their buttons are shown in Figure 5.4;

Figure 5.4: Block containing the power button of the Low and High Voltages. The Low voltage button must be pressed as first and just then the High Voltage can be activated.

4. The radioactive source of ^{137}Ce, emitting γ photons at $662\,keV$, has been positioned in front of the detector under study and the Oscilloscope will shown the curve related to the pulses, a red oscillating line related to the value of the digital potentiometer and a blue oscillating line showing the output signal coming from the HV Divider, as shown in Figure 5.5;

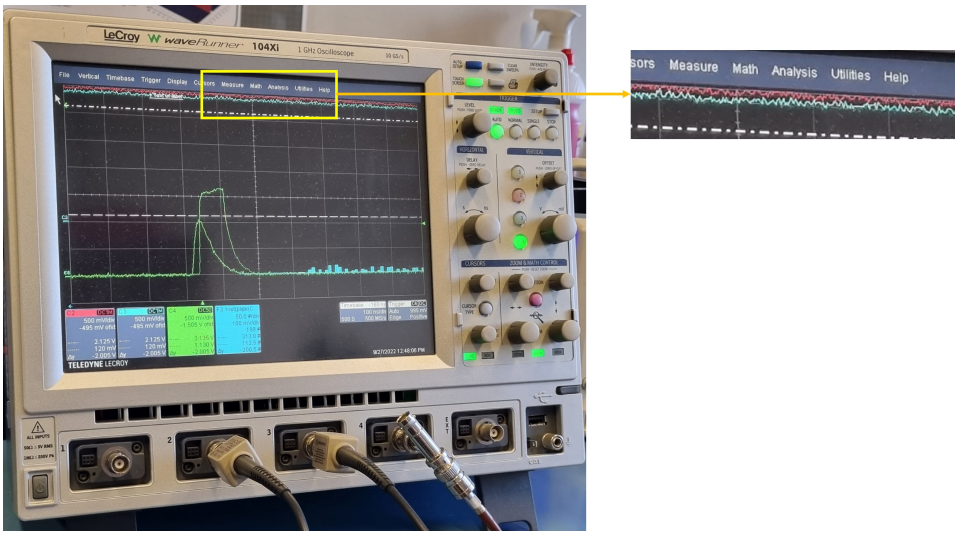

Figure 5.5: Signal shown using the Oscilloscope. The red and blue lines represent respectively the voltage of digital potentiometer and the value extracted from the HV divider.

5. It's time to use the Digital potentiometer, the controls of which are shown in Figure 5.6. At first, the digital potentiometer need to be set using the Up and Down commands. Since the program doesn't have yet a step counter in which it's possible to know how many times the Up and Down buttons have been pressed, the first operation is to reach its maximum value by pressing the Up button several times until there is no more movements of the curves on the oscilloscope. Subsequently the blue and red lines could be well separated, as shown in Figure 5.5, symptom that the feedback system is not working properly anymore. In order to overlap the two lines and to be sure that the voltage of this potentiometer has a certain range in which to vary, the Down button must be pressed a more or less 50 number of times to reach the half of its range of steps, equal to 120. This process indeed is necessary from the moment that a too low or too high value set on the digital potentiometer will preclude the possibility to reach the desired voltage;

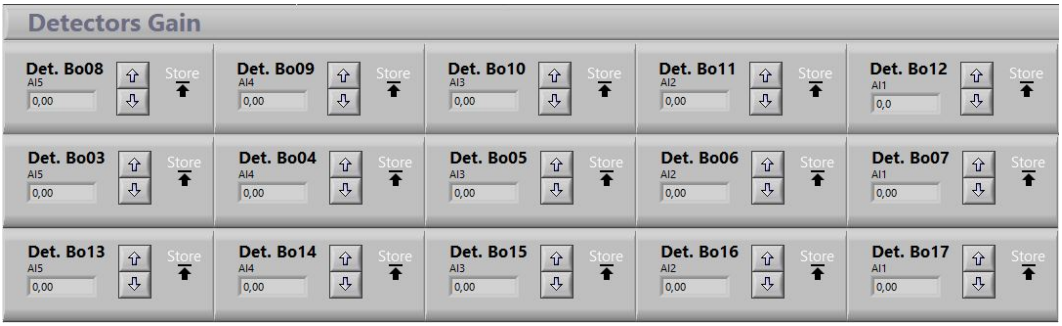

Figure 5.6: UP, DOWN and Store button to control the value of the digital potentiometer.

6. Once the stability has been reached, the Store command will save the value of the digital potentiometer that will be considered from that moment until another Store will be used;

7. Now the potentiometer controlling directly the High Voltage can be used. In-

deed, the final characterization of the detector is performed by acting on this potentiometer, bringing all peaks to be slightly lower than a certain voltage. This maximum value is represented by the dashed white line, shown in Figure 5.7. The need to have all the peaks with same amplitude comes from the requirement to have perfectly overlapping spectra, fundamental to consider the total detection;

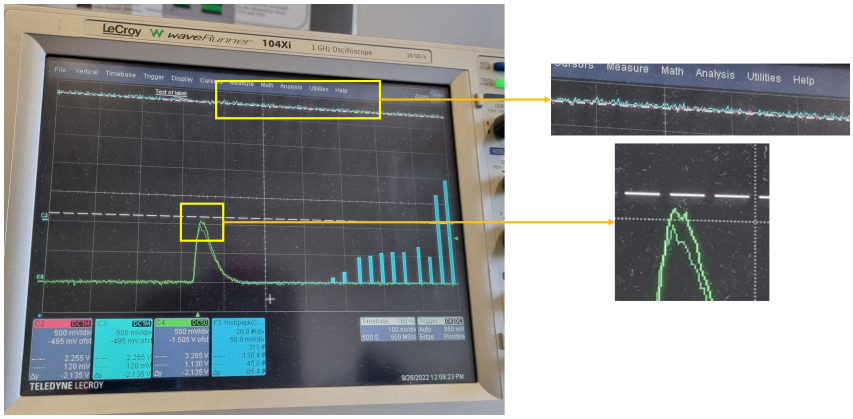

Figure 5.7: Signal shown using the Oscilloscope. The red and blue lines are rightly overlapped and the peak is below the decided maximum value, represented by the white dashed line.

All the detectors will require a different voltage to reach the dashed line (positioned around $1.2\,V$), chosen to have a very lower number of saturation in all the spectra obtained, as shown in Figure 5.8;

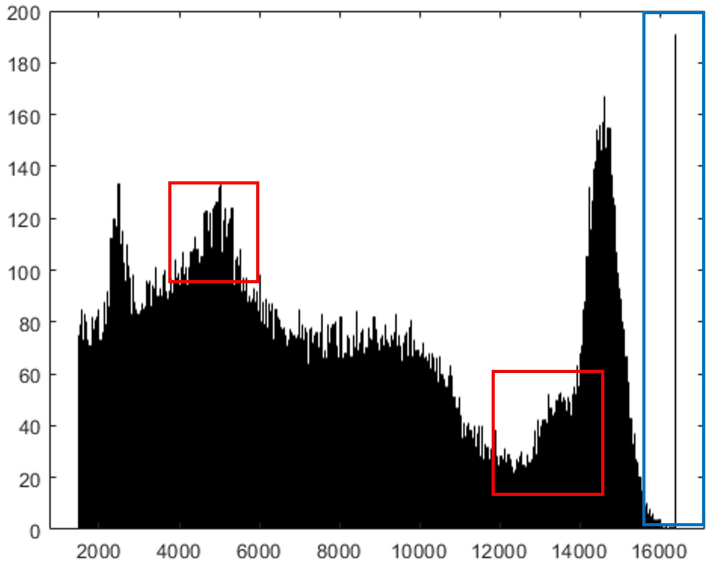

Figure 5.8: Spectrum obtained using the GSPS. In the blue square there is the line corresponding to the saturations, too much higher with respect the dimension of the peak. In red, instead, the errors of the spectrum due to non-stability of the signal are shown.

8. Once the detection system has been characterized, the analog potentiometers should be not touched again. Since the detection system is highly conditioned by the temperature, it could happen that the peaks will have different amplitudes in different experiments. To bring back these amplitudes to predefined values, the digital potentiometer will be used;

9. In the end, the GSPS is used to acquire the information about the detection. To start the acquisition, some input parameters have to be written in Windows PowerShell, like:

   - ADC to use, inserting a number from 0 to 3;
   - the trigger indicates the half value of y coordinates. It is used to decide the minimum value at which starting the signal acquisition. In this thesis, it's value is around 1500;
   - the number of samples, set to be 500;
   - the delay time, set to be *certainvalue*, which indicates after how many *ns* the trigger starts;
   - the number of events. In order to take measurement for half of an our, it must be 115000.

   All these values has been chosen to be sure to acquire just the signal and not possible noise signals.

10. The output of the GSPS is then analyzed using a MatLab program to obtain the spectrum, shown in Figure 5.9, making possible to extract the information like standard deviation and the position of the peak centroid.

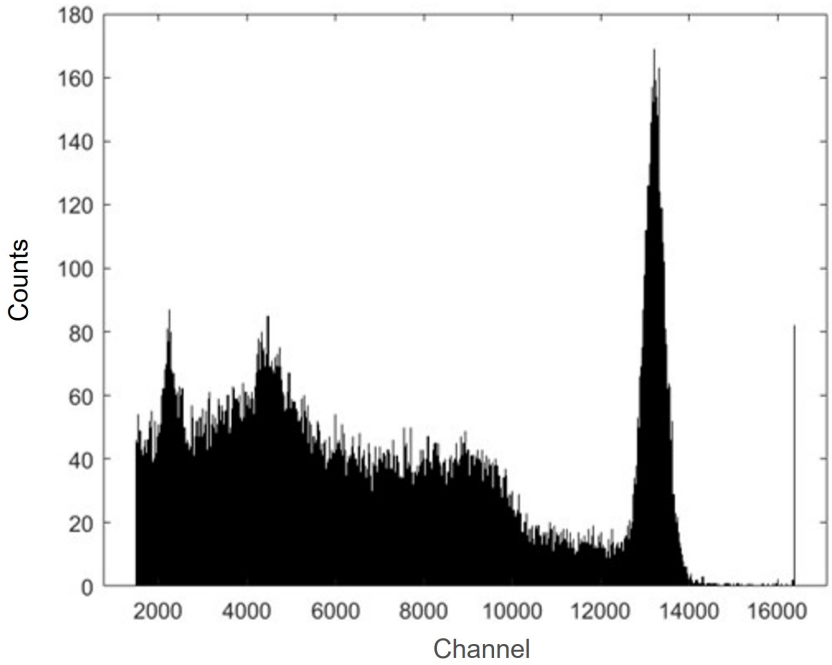

Figure 5.9: Histogram example of the GSPS output. It's possible to observe: several peaks around 2000 and 5500 which are related to component of the detection system; one major peak corresponding to the gamma radiation; one straight line corresponding to the saturation.

5.2 Results

In this section the spectra related to the detectors, shown in Figures 5.10 and 5.11, are presented together with some useful information like FWHM, Resolution, the voltage of each detector and the current exiting from the MOSFET.

Since this is a work in progress, not all the detectors have been studied and some of the results so are not shown. The acquisition time window considered is about 30 minutes.

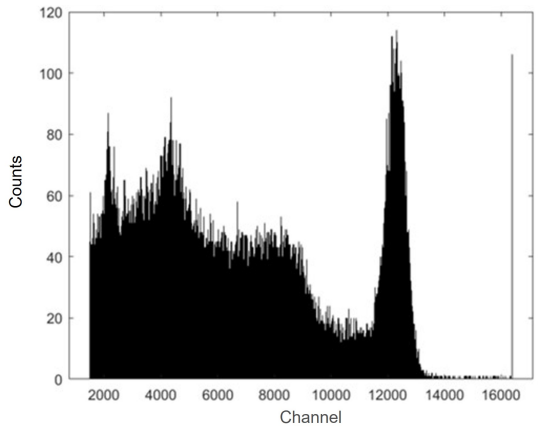

(a) Detector 3

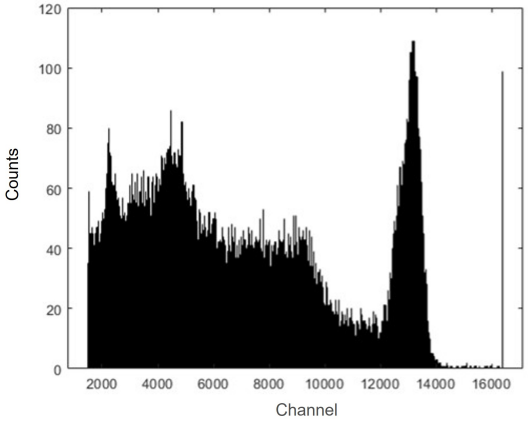

(b) Detector 4

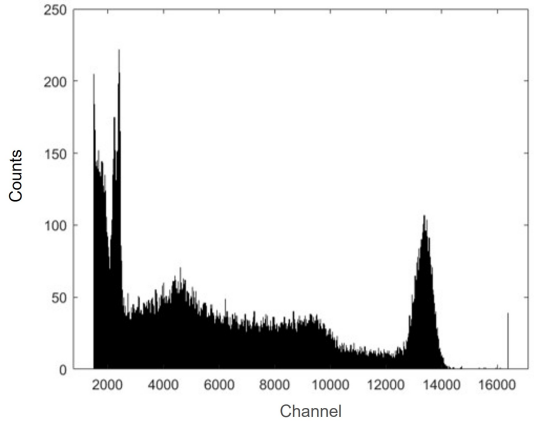

(c) Detector 5

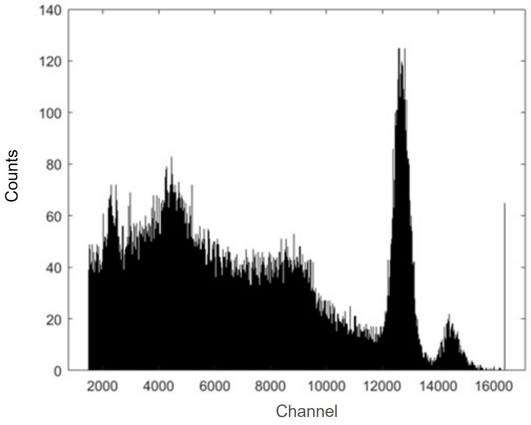

(d) Detector 6

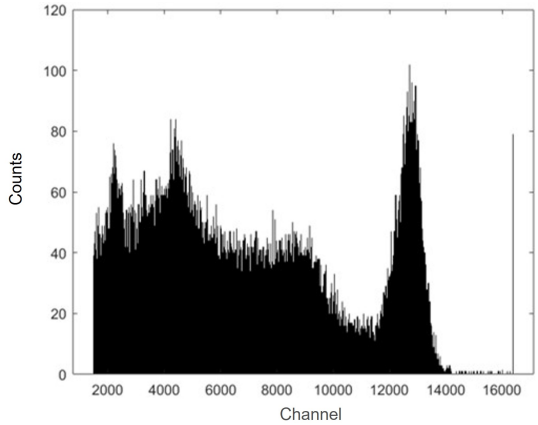

(e) Detector 7

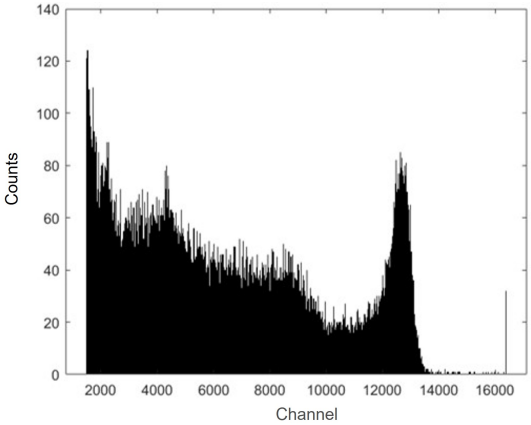

(f) Detector 8

Figure 5.10: Spectra of detectors 3, 4, 5, 6, 7, 8.

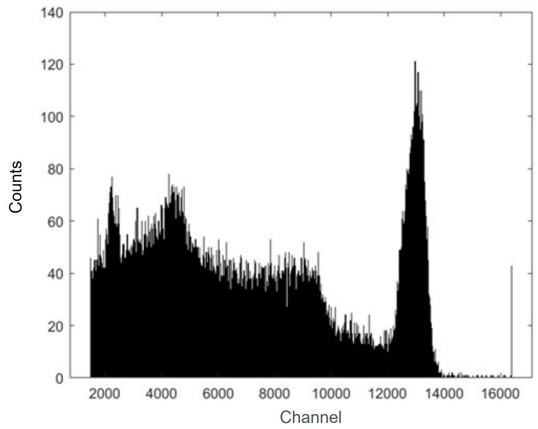

(a) Detector 9

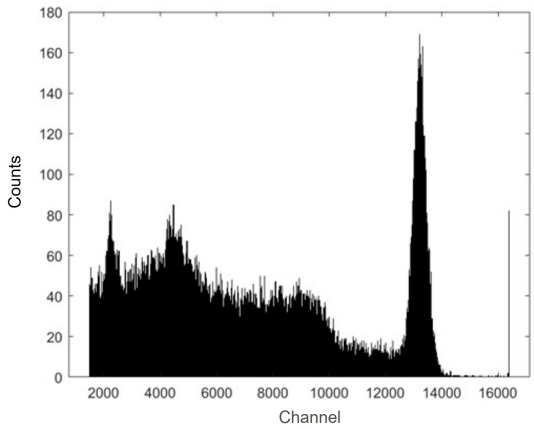

(b) Detector 10

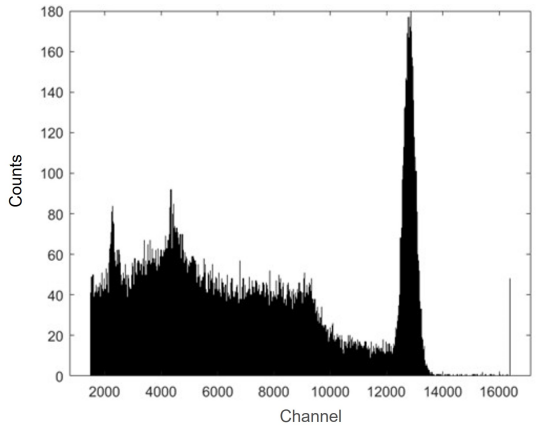

(c) Detector 11

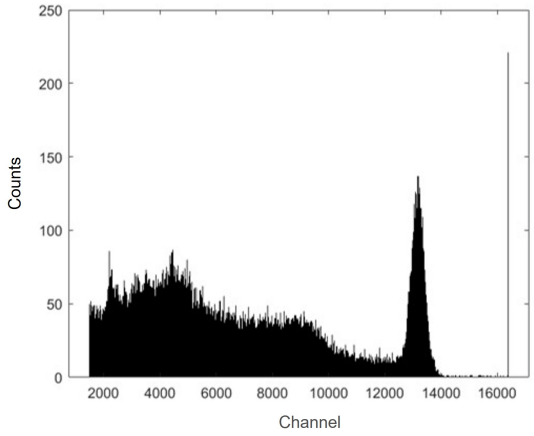

(d) Detector 12

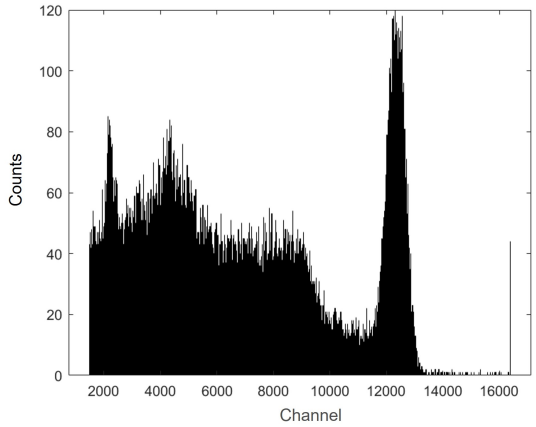

(e) Detector 13

Figure 5.11: Spectra of detectors 9, 10, 11, 12, 13.

In Table 5.1 and 5.2 some measured characteristics of the detectors are given: the Voltage of each detector, the Voltage exiting from the MOSFET (indicated as a current), the FWHM, the Resolution.

The Voltage exiting from the HV Generator is set to $-950\,V$ while the Middle Voltage to $-303\,V$.

Even if it is indicated as a current, the I_{mos} represents the voltage associated to the current flowing in the MOSFET. This value must be maintained quite low, more or less around $-1.00\,V$, in order to avoid spikes in the MOSFET that can cause distortions or that can damage the circuit.

The FWHM has been obtained starting from the equation used for the fitted curve which has a Gaussian Distribution:

$$f(x) = \frac{1}{\sqrt{2\pi\sigma^2}} e^{-\frac{1}{2}\left(\frac{x-\mu}{\sigma}\right)^2} \tag{5.1}$$

where μ is the mean and σ the standard deviation. For this study, μ gives the information about the position of the Peak Centroid.

At this point, the FHWM is obtained using:

$$FWHM = 2.33 \cdot \sigma \tag{5.2}$$

and the Resolution is given by:

$$R = \frac{FWHM}{\mu} \cdot 100 \tag{5.3}$$

The errors associated to the measurement are obtained considering the sensibility of the instruments, like voltmeter and oscilloscope, and using the propagation formula.

Det.	V_{det} (V)	I_{mos} (V)	μ or Peak Centroid (ch)		σ (ch)
			Nom.	Meas.	
3	-848.00 ± 0.04	-1.15 ± 0.01	290.33	12238.50 ± 2.58	378.52 ± 1.83
4	-816.00 ± 0.04	-1.35 ± 0.01	261.75	12985.50 ± 2.86	419.43 ± 2.02
5	-772.00 ± 0.04	-1.50 ± 0.01	288.54	13289.80 ± 2.88	379.28 ± 2.03
6	-852.00 ± 0.04	-1.16 ± 0.01	265.09	12644.60 ± 2.55	357.15 ± 1.80
7	-772.00 ± 0.04	-1.60 ± 0.01	284.14	12650.90 ± 3.06	452.67 ± 2.17
8	-868.00 ± 0.04	-1.04 ± 0.01	299.58	12475.00 ± 3.38	452.60 ± 2.39
9	-869.00 ± 0.04	-0.89 ± 0.01	295.55	12930.40 ± 2.34	346.24 ± 1.66
10	-920.00 ± 0.04	-0.80 ± 0.01	260.24	13208.10 ± 1.92	281.32 ± 1.36
11	-836.00 ± 0.04	-1.18 ± 0.01	271.92	12815.20 ± 1.49	218.35 ± 1.05
12	-804.00 ± 0.04	-1.38 ± 0.01	282.01	13144.40 ± 2.00	267.89 ± 1.41
13	-856.00 ± 0.04	-1.15 ± 0.01	313.22	12329.30 ± 2.11	309.89 ± 1.49

Table 5.1: Characteristics of each detector extrapolated from the oscilloscope (V_{det}), the voltmeter (I_{mos}) and MatLab program (μ and σ). The nominal values are the same of Table 3.4.

Det.	FWHM (ch)		Resolution (%)	
	Nom.	Meas.	Nom.	Meas.
3	8.69	881.94 ± 4.26	2.99	7.21 ± 0.04
4	8.05	977.26 ± 4.71	3.08	7.53 ± 0.04
5	9.03	883.72 ± 4.74	3.13	6.65 ± 0.04
6	8.17	832.15 ± 4.20	3.08	6.58 ± 0.03
7	8.02	1054.71 ± 5.05	2.82	8.34 ± 0.04
8	8.61	1054.56 ± 5.57	2.87	8.45 ± 0.05
9	9.26	806.74 ± 3.86	3.10	6.24 ± 0.03
10	8.32	655.48 ± 3.16	3.20	4.96 ± 0.02
11	7.93	508.75 ± 2.45	2.92	3.97 ± 0.02
12	8.39	624.18 ± 3.30	2.97	4.75 ± 0.03
13	9.24	722.03 ± 3.47	2.95	5.86 ± 0.03

Table 5.2: FWHM and Resolution of each detector. The nominal values are the same of Table 3.4.

5.3 Discussion of the Results

Looking at Figures 5.10 and 5.11, it's possible to observe very different behaviors. All the measurements have been taken in the office without a perfect control over the temperature. Since this detection system is strongly temperature dependent, it has been not possible to maintain the voltage constant and so the fluctuations have been affected the results.

Even with this temperature problem, the characterization of the detectors has been performed.

All the spectra present the following characteristics:

- two defined peaks produced by the detection of smaller radiation, like the Lanthanum composing the detectors;
- the Compton Edge, effect produced by the scattering;
- the well-defined peak generated corresponding to the γ emission;
- the saturation straight line.

A disturbing effect that affects almost the of spectra is related to the non-constant voltage which causes an unfixed shifting. This disorder causes an unwanted variation of the amplitude and so a different position of the peaks that, anyways, has been maintained between 12000 ch and 13500 ch.

The detectors 3 and 4 show a very high saturation line, almost surely related to the temperature problem. Indeed, the saturation level could be reached if the signal becomes too high due to a lower temperature.

The detector 5 shows a particular shape: in the first 2000 bins, two peaks extremely large occurs, due to a sudden shut-down of the detector and so null values have been inserted in the spectrum. Although this error, the γ peak is visible. Compared to this peak, the saturation line is small which results in a good acquisition.

All the peaks of the detector 6 are visible and well separated. A fourth unexpected peak can be noticed, probably due to the shifting.

The spectrum of the detector 7 present recognizable peaks that are evidently affected by the shifting. Also, the saturation level is quite high.

The detector 8 presents a very low saturation line and a distinguishable γ peak. The major problem here is the region before the Compton Edge: it is most higher than expected, probably due to a fast decreasing signal. This could be connected to an increasing temperature of detector.

The detector 9 shows a γ peak evidently affected by the fluctuations but this doesn't resolve in a high saturation line that remains quite small.

The next detectors are the ones with the best spectra. Even if the shifting is present, the spectra of detectors 10, 11, 12 show very narrow and high γ peaks. Indeed, not considering the saturation line, also the detector 12 shows a high peak with respect to the other regions.

The detector 13 has a very high γ peak but not so narrow, which will result in a lower resolution.

Consider now the values in Tables 5.1 and 5.2.

The detectors' voltages are all in the expected range, from 750 V up to 1000 V, with the majority concentrated in the range [800 V, 900 V]. Detector 10 presents

the highest module value which means it is the one with the lowest gain. Indeed, in order to reach the value the detector need more voltage with respect to the other, symptom of a lower gain. On the contrary, the lowest module value belongs to the detectors 5 and 7, sign that their gains are the highest.

In addition, it's possible to observe an inverse relationship between the voltage module required by the detector to reach the desired amplitude and the voltage module exiting from the MOSFET. Indeed, the lowest $|V_{det}| = 772.00\ V$ of the detectors 5 and 7 corresponds to the highest $|I_{mos}|$, respectively of $1.50V$ and $1.60V$.

Observing the values of μ, σ, FWHM and Resolution obtained from the spectra, it's clear their difference from the nominal values, with measured Resolutions worst than the nominal ones.

The difference between the nominal and extracted values in channel terms could be reconducted to a different scale used in formation of the spectrum. Since the uncontrolled temperature of the environments affects the spectrum, it should come as no surprise that there isn't a relation between the nominal and measured values.

An existing relation that can be observed is between the spectra and the Resolution values. Indeed, the spectra most affected by the fluctuations show worse resolutions, like the detectors 7 and 8 which respectively have a measured resolution of (8.34 ± 0.04) % and (8.45 ± 0.05) %.

The best looking spectra are those of the last detectors, from 10 to 12. Almost surely, the temperature during the acquisition of the signal from these detectors has been maintained more or less constant.
In presence of a stable temperature, the relation between the nominal and the measured resolutions is shown: these experimental resolutions indeed follow the relationship established from their respective nominal values.

So an expected effect that wasn't under study has been demonstrated: the strong dependence of the detection system to the temperature.

Conclusions

The FAMU Experiment is a project with the aim to determine with high precision the Proton Radius. The desire to know better the internal structure of the Proton is born in the last years when measurements on Lamb Shift using the muonic hydrogen have define a lower value of its radius, approximately 7σ lower. From the recognition of a new road to explore, the Proton Radius Puzzle has become one of the most interesting tasks.

To reach a value of the proton radius with the highest possible precision, a new detection system for the FAMU Experiment need to be studied and characterized. This is the objective of this thesis work.

The resulting model has been constructed according to previous experiments and simulations, leading to the construction of a 17-detectors semicircular crown. Here not all the detectors are presented for several reasons: some of them weren't mounted on the circuit while the acquisition using the others has not been possible since the detection system needed to be sent to the Riken-Ral for the final acquisition. Also, since the GSPS is not already fully completed, the detection has been performed on one detector at the time. Since the final acquisition will required to work with all detectors switched on, first the single quadrants have been observed and then all the detection system has been activated. In this first characterization the acquisition time was of 30 minutes, which is very smaller with respect to the future acquisitions. Even with such a small acquisition time, the entire system was left on for several ours, demonstrating so its capacity to work for a longer period.

The first operations to perform were the connection of the detection system to the pc to control it, to the oscilloscope to check the signal shape and the positioning of the radioactive source Cesium 137.

After the switching on of the detection system thanks to a LabView program, the calibration of the detectors can begin.

Once the HV flew in the circuit, a signal should appear on the oscilloscope. Due to a probable different environment temperature in which the acquisition will be taken, this characterization of the detectors was done to set the digital potentiometer on a modifiable value, more or less in the half of its range of steps which was set to 120. Then, acting on the two analog potentiometers, the voltage of each detector has been modified such that all the signals shared the same amplitude. In order to achieve this objective, a dashed line has been positioned on the oscilloscope at $1.2\,V$, value chosen to reduce the presence of the saturation signals which can affect the final results. In this way, when the detectors will be completely closed, the amplitude of the signals will be modified just using the digital potentiometer.

Once the desired shape of the signal has been reached, the acquisition using the GSPS has begun.

The results are affected by non-stable temperature of the work environment

which results in a shifting of the spectrum and so in less precision measurements. By observing the obtained spectra in Figure 5.10 and 5.11, all of them show a recursive scheme: two peaks coming from the acquisition of radiation of detectors' element, the Compton Edge, the γ peak and a possible saturation line.

All these spectra are characterized in order to have a value of the centroid as congruent with others as possible. Even if it is a wide range, the centroids are all contained in [12000 ch, 13500 ch].

The spectra most affected by these fluctuations are those corresponding to the detectors 5 and 7. The detector 5 also contains two unexpected peaks due to an its involuntary shutdown in which the acquisition doesn't have received the signal and so null values have composed the spectrum.

Also the detector 6 shows a different spectrum: probably due to a lower temperature, the amplitude of the signal increased too much in the last part of the acquisition, generating a small peak before of the saturation lines.

On the contrary, the best spectra are those of detectors 10, 11, 12. Their γ peaks are very narrow, high and well-defined. The detector 12 shows a smaller peak as a matter of fact, but this due to the presence of a high saturation line. Indeed, without considering that line, the peak will be otherwise higher with respect to those in the first part of the spectrum.

Consider now the values, shown in Table 5.1 and 5.2, obtained using a MatLab program. First of all, the scale of nominal values is unknown and so it is different with respect to the experimental measures.

A certain relationship is evident between V_{det} and I_{mos}: a higher $|V_{det}|$ will correspond to a lower $|I_{mos}|$.

Looking strictly to the values, the influence of the fluctuations is clear. Indeed, putting both the types of values in ascending order, the order of the detectors will be different in general, resulting in worse experimental Resolutions.

Anyways, this is not completely true: the best measured Resolutions are those of the detectors 10, 11 and 12 which are also the best from the nominal point of view. Indeed, these detectors were less affected by the fluctuations thanks to a more stable temperature of the room, marked also from the shape of their spectrum.

In conclusion, almost the totality of the detectors works as expected and the temperature dependence will be considered by performing the experiment at the Riken Ral Facility in the port 1 where the temperature will be maintained constant with a tolerance of $\pm 1\,^{\circ}C$.

In the last 2022, this detection system will be sent in London for the first run of tests and data processing. Then the system will return in Bologna for the inclusion of the GSPS and the final characterization of the detectors.

The major data taking will be performed in the first half of 2023 using all the 17 detectors for almost 20 days.

List of Figures

List of Tables

Bibliography

Adamczak, A et al. (2018). "The FAMU experiment at RIKEN-RAL to study the muon transfer rate from hydrogen to other gases". In: *Journal of Instrumentation* 13.12, P12033.

Antognini, Aldo (2005). "The lamb shift experiment in muonic hydrogen". PhD thesis. lmu.

Antognini, Aldo et al. (2013). "Proton structure from the measurement of 2S-2P transition frequencies of muonic hydrogen". In: *Science* 339.6118, pp. 417–420.

Baldazzi, G et al. (2017). "The LaBr3 (Ce) based detection system for the FAMU experiment". In: *Journal of Instrumentation* 12.03, p. C03067.

Banks, Thomas Ira (2007). *A measurement of the rate of muon capture in hydrogen gas and determination of the proton's induced pseudoscalar coupling g P*. University of California, Berkeley.

Belloni, Carlo (2014). "Determinazione sperimentale della costante di Rydberg". In.

Bernauer, Jan C (2010). "Measurement of the elastic electron-proton cross section and separation of the electric and magnetic form factor in the Q^2 range from 0.004 to 1 $(GeV/c)^2$".

Bernauer, Jan C and A1 Collaboration (2011). "High-precision determination of the electric and magnetic form factors of the proton". In: *AIP Conference Proceedings*. Vol. 1388. 1. American Institute of Physics, pp. 128–134.

Bernauer, JC et al. (2014). "Electric and magnetic form factors of the proton". In: *Physical Review C* 90.1, p. 015206.

Beyer, Axel et al. (2013). "Precision spectroscopy of atomic hydrogen". In: *Journal of Physics: Conference Series*. Vol. 467. 1. IOP Publishing, p. 012003.

Bezginov, N et al. (2019). "A measurement of the atomic hydrogen Lamb shift and the proton charge radius". In: *Science* 365.6457, pp. 1007–1012.

Biraben, François (2009). "Spectroscopy of atomic hydrogen". In: *The European Physical Journal Special Topics* 172.1, pp. 109–119.

Bonesini, M (2020). "The FAMU experiment at RIKEN RAL for a precise measure of the proton radius". In: *arXiv preprint arXiv:2010.01398*.

Carlson, Carl E. (2015). "The proton radius puzzle". In: *Progress in Particle and Nuclear Physics* 82, pp. 59–77. ISSN: 0146-6410. DOI: https://doi.org/10.1016/j.ppnp.2015.01.002. URL: https://www.sciencedirect.com/science/article/pii/S0146641015000034.

Chadwick, James (1932). "Possible existence of a neutron". In: *Nature* 129.3252, pp. 312–312.

D'Antone, I et al. (2018). "A 1 GS/s sampling digitizer designed with interleaved architecture (GSPS) for the LaBr3 detectors of the FAMU experiment." In: *Topical Workshop on Electronics for Particle Physics (TWEPP2018)*. Vol. 17, p. 21.

Dupays, Arnaud et al. (2003). "Proton Zemach radius from measurements of the hyperfine splitting of hydrogen and muonic hydrogen". In: *Physical Review A* 68.5, p. 052503.

Eides, Michael I, Howard Grotch, and Valery A Shelyuto (2001). "Theory of light hydrogenlike atoms". In: *Physics Reports* 342.2-3, pp. 63–261.

Feinberg, Gerald and Leon M Lederman (1963). "The physics of muons and muon neutrinos". In: *Annual Review of Nuclear Science* 13.1, pp. 431–504.

Gegier, H and Ernest Marsden (1909). "On a diffuse reflection of the α-particles". In: *Proceedings of the Royal Society of London. Series A, Containing Papers of a Mathematical and Physical Character* 82.557, pp. 495–500.

Gorringe, TP and DW Hertzog (2015). "Precision muon physics". In: *Progress in Particle and Nuclear Physics* 84, pp. 73–123.

Griffiths, David (2020). *Introduction to elementary particles*. John Wiley & Sons.

Groom, Donald E, Nikolai V Mokhov, and Sergei I Striganov (2001). "Muon stopping power and range tables 10 MeV–100 TeV". In: *Atomic Data and Nuclear Data Tables* 78.2, pp. 183–356.

Guffanti, D, FAMU collaboration, et al. (2016). "The FAMU experiment: muonic atoms to probe the proton structure". In: *Journal of Physics: Conference Series*. Vol. 689. 1. IOP Publishing, p. 012018.

Guffanti, Daniele (2015). "The FAMU experiment: measurement of muonic atoms spectra Master's thesis".

L., Rignanese (2017). "Design and implementation of a high speed digital pulse processor". In.

Le, Anh-Thu and Chii-Dong Lin (2005). "Muon transfer from muonic hydrogen to atomic oxygen and nitrogen". In: *Physical Review A* 71.2, p. 022507.

Measday, David F (2001). "The nuclear physics of muon capture". In: *Physics Reports* 354.4-5, pp. 243–409.

Mocchiutti, E et al. (2018a). "FAMU: study of the energy dependent transfer rate $\Lambda\mu p \rightarrow \mu 0$". In: *Journal of Physics: Conference Series*. Vol. 1138. 1. IOP Publishing, p. 012017.

Mocchiutti, E et al. (2020). "First measurement of the temperature dependence of muon transfer rate from μp atoms to oxygen". In: *Physics Letters A* 384.26, p. 126667.

Mocchiutti, Emiliano et al. (2018b). "First FAMU observation of muon transfer from μp atoms to higher-Z elements". In: *Journal of Instrumentation* 13.02, P02019.

Mohr, Peter J, David B Newell, and Barry N Taylor (2016). "CODATA recommended values of the fundamental physical constants: 2014". In: *Journal of Physical and Chemical Reference Data* 45.4, p. 043102.

Nagamine, Kanetada (2003). *Introductory muon science*. Cambridge University Press.

Parthey, Christian G et al. (2011). "Improved measurement of the hydrogen 1 s–2 s transition frequency". In: *Physical review letters* 107.20, p. 203001.

Pizzolotto, C et al. (2020). "The FAMU experiment: muonic hydrogen high precision spectroscopy studies". In: *The European Physical Journal A* 56.7, pp. 1–15.

Pizzolotto, C et al. (2021). "Measurement of the muon transfer rate from muonic hydrogen to oxygen in the range 70-336 K". In: *Physics Letters A* 403, p. 127401.

Pohl, Randolf et al. (2010). "The size of the proton". In: *nature* 466.7303, pp. 213–216.

Pohl, Randolf et al. (2013). "Muonic hydrogen and the proton radius puzzle". In: *Annual Review of Nuclear and Particle Science* 63, pp. 175–204.

Rignanese, Luigi Pio (2019). "The FAMU experiment: Towards the measurement of the hyperfine splitting of the muonic hydrogen".

Ross, G (1984). "Quarks and Leptons-An introduction course in modern particle physics". In: *NATURE* 311.5986.

Rutherford, Ernest (1911). "LXXIX. The scattering of α and β particles by matter and the structure of the atom". In: *The London, Edinburgh, and Dublin Philosophical Magazine and Journal of Science* 21.125, pp. 669–688.

Schlenga, Robin (Sept. 2015). "On the Physical Origin of the Lamb Shift". PhD thesis.

Suzuki, T, David F Measday, and JP Roalsvig (1987). "Total nuclear capture rates for negative muons". In: *Physical Review C* 35.6, p. 2212.

Thomas, Simon et al. (2019). "High-Resolution Hydrogen Spectroscopy and the Proton Radius Puzzle". In: *Annalen der Physik* 531.5, p. 1800363.

Thomson, Joseph John (1897). "XL. Cathode rays". In: *The London, Edinburgh, and Dublin Philosophical Magazine and Journal of Science* 44.269, pp. 293–316.

Tiesinga, Eite et al. (2021). "CODATA recommended values of the fundamental physical constants: 2018". In: *Journal of Physical and Chemical Reference Data* 50.3, p. 033105.

Vacchi, A (2020). "The FAMU Experiment: measuring the Zemach radius of the proton from laser spectroscopy of the 1S hyperfine splitting in muonic hydrogen". In.

Zhan, X. et al. (2011). "High-precision measurement of the proton elastic form factor ratio $\mu_p G_E/G_M$ at low Q^2". In: *Physics Letters B* 705.1, pp. 59–64. ISSN: 0370-2693. DOI: https://doi.org/10.1016/j.physletb.2011.10.002. URL: https://www.sciencedirect.com/science/article/pii/S0370269311012342.

Sitography

FAMU (2015a). *FAMU Beam*. URL: https://web.infn.it/FAMU/the-research/.
— (2015b). *FAMU Detector*. URL: https://web.infn.it/FAMU/the-research/.
— (2015c). *FAMU Laser*. URL: https://web.infn.it/FAMU/the-research/.
— (2015d). *FAMU Target*. URL: https://web.infn.it/FAMU/the-research/.
PJRC (n.d.). *Teensy*. URL: https://www.pjrc.com/teensy/#:~:text=The\%20Teensy\%20is\%20a\%20complete,done\%20via\%20the\%20USB\%20port..